Power Flow Analysis and Optimization for Combined Heat and Power Systems Considering Different Time Scales of Electricity and Heat

Thesis Submitted to

Tsinghua University

in partial fulfillment of the requirement

for the degree of

Master of Science

in

Electrical Engineering

by

Xin Qin

Thesis Supervisor： Professor Hongbin Sun

March, 2020

Online Version Details

This online version has been adapted for easy sharing and includes necessary formatting adjustments. The contents remain unchanged from the original version.

For the most recent research findings on synchronous economic dispatch (Chapter 3) and asynchronous dispatch (Chapter 4) of combined heat and power systems, please refer to the published papers [D1] and [D2], respectively. Additional resources related to this paper can be accessed on the website: https://xinqin-site.github.io/codes/.

Please find the citation information for this thesis below:

IEEE:

X. Qin, “Power flow analysis and optimization for combined heat and power systems considering different time scales of electricity and heat,” Master’s thesis, Tsinghua University, 2020.

BibTeX:

@ mastersthesis{qin2020msthesis,
title={Power Flow Analysis and Optimization for Combined Heat and Power Systems Considering Different Time Scales of Electricity and Heat},
author={Qin, Xin},
year={2020},
school={Tsinghua University}
}

References:

[D1] X. Qin, Y. Guo, X. Shen and H. Sun, "Increasing Flexibility of Combined Heat and Power Systems Through Optimal Dispatch With Variable Mass Flow," in IEEE Transactions on Sustainable Energy, vol. 13, no. 2, pp. 986-997, April 2022, doi: 10.1109/TSTE.2022.3141894.

[D2] X. Qin, H. Sun and Y. Guo, "Asynchronous Economic Dispatch for Combined Heat and Power Systems," in IEEE Open Access Journal of Power and Energy, vol. 7, pp. 467-477, 2020, doi: 10.1109/OAJPE.2020.3030242.

Abstract

Driven by the objective of constructing an open and interconnected Energy Internet, combined heat and power systems break the physical and cyber barriers between the electric power system and the heating system and thus improves the system's efficiency and reduces greenhouse gas emission. However, current studies on power flow analysis and optimization do not fully address the different time scale characteristics of the electric power system and the heating system: The research considering the different time scales simplifies system topology and control mechanisms; The research without compromise on system topology and control mechanisms fails to consider the different time scales of electricity and heat. Additionally, existing solution methods for power flow and optimization have convergence problems and sometimes are not interpretable. These problems threaten the efficiency and security of combined heat and power systems.

In this dissertation, the challenges from different time scales are addressed in the power flow, economic dispatch, and frequency control for the combined heat and power system, where the topology and control mechanisms are not simplified. The main contributions are:

1) In power flow analysis, the power flow model of combined heat and power systems is proposed considering the heat dynamic process, the meshed network, and variable mass flow. A decomposition solution method based on backward-forward iteration is proposed to solve the nonlinear power flow model iteratively and sequentially. The results of the proposed method have high accuracy compared with real-time measurement. Also, the proposed method has fast convergence speed and avoids the divergence problems of existing methods. Moreover, the proposed method overperforms commercial software in terms of the heat dynamic process. 2) In the synchronous economic dispatch with variable mass flow, the proposed optimization model reduces the complexity from integers in the existing optimization model without compromising on accuracy. The resulting non-convex model is solved by the proposed modified Generalized Benders Decomposition method with improved convergence and acceleration. Compared with existing methods, the proposed method has lower overall

costs and overcomes the divergence problem of solver IPOPT. 3) In the asynchronous economic dispatch, the different adjustment time scales of the electric power system and the heating system are addressed by the asynchronous dispatch models. The comparison with the traditional synchronous methods demonstrates that the asynchronous method can overcome the security problems and infeasible results. Also, the influence of the dispatch interval on the overall costs and computational efficiency is studied. 4) In the frequency control, a fully-distributed frequency control method is developed with the system-wide optimality. The proposed control method does not violate the constraints of generator's feasible regions compared with existing control methods and is robust to the inaccurate damping coefficient.

In summary, this dissertation studies the challenges from different time scales in power flow analysis and optimization of combined heat and power systems. By the innovation of models and solution methods, the simplifications on topology and control mechanisms are overcome, while the convergence and accuracy are improved compared with existing methods. The research in this dissertation can be applied for the accurate and efficient power flow calculation, economic dispatch, and frequency control of the combined heat and power systems in the Energy Internet.

Keywords: combined heat and power systems; different time scales; power flow; economic dispatch; frequency control

Table of Contents

List of Symbols

Abbreviations:

AC	Alternating Current
AGC	Automatic Generation Control
CHP	Combined heat and power
DC	Direct Current
DER	Distributed Energy Resource
ED	Economic Dispatch
GBD	Generalized Benders Decomposition
MINLP	Mixed-Integer Nonlinear Programming
MIQP	Mixed-Integer Quadratic Programming
SOCP	Second-Order Cone Programming

Chapter 1: Introduction

1.1 Background and Motivation

The traditional operation of the electric power system and the heating system adopts a highly closed manner with various barriers. The barriers from the different characteristics of electricity and heat make it difficult to model and operate the two energy systems jointly. Also, there are barriers from the separate operation of the two different energy systems because they are owned by different utility companies. These barriers not only influence energy systems' efficiency but also threaten security. For example, in December 2019, the failure of electric transmission lines caused by snowstorms led to the breakdown of the Icelandic heating system powered by electricity [1]. Moreover, in December 2018, the breakdown of a CHP unit led to the major failure in the heat network, where an area of about 13 million m^2 lost heat supply in Ningxia [2]. With the increasing number of renewables and electric-heat coupling devices especially the CHP units integrated into energy systems, it is impossible to adopt the traditional idea of increasing each system's reserves for security because of low efficiency.

In recent years, the concept of Energy Internet has been developed all over the world whose ultimate goal is to build an open, interconnected, and equal platform for energy systems [3]-[5]. To this end, breaking the barriers between different energy sectors, such as the electric power systems and the heating systems, becomes indispensable. Driven by this motivation, the combined heat and power system interconnects the electric power system and the heating system in both the physical layer and the cyber layer to jointly operate the two energy systems, which contributes to the improvement of the system's efficiency and security. The combined operation of the two energy systems can improve about 50% of fuel efficiency and reduce 13%-18% of carbon emission [6][7]. Furthermore, the complementary property of the two energy systems can be further used for more flexibility [8]: the electric power system requires real-time power balance whereas the temperature in a heating system has much higher inertia. Thus, if operated properly, heating systems can serve as storage for power systems, which may in turn provide alternative heat sources to heat systems. Therefore, it is of crucial importance to exploit such a complementary property with all possible adjustment means.

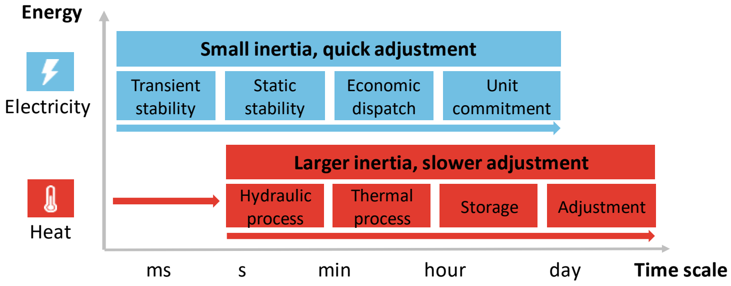

Figure 1-1. The time scales of different energy systems.

Table 1-1 The dynamic and adjustment time scales of the two energy systems.

Energy systems		Dynamic time scale	Adjustment time scale
Electric power system		<1 second	minutes
Heating system	Hydraulic process	seconds~minutes	minutes
	Thermal process	minutes~hours	minutes~hours

However, as shown in Figure 1-1 and Table 1-1, in the operation of combined heat and power systems, the electric power system and the heating system have different dynamic and adjustment time scales: The electric power system can reach the steady-state in seconds and is adjusted in minutes, while the heating system has a long dynamic process varying from minutes to hours and is adjusted in minutes or hours [9]. As a result, complex partial differential equations are needed to describe the heat dynamic process in power flow and optimization problems [10]. In addition, when the system topology and control mechanisms are not simplified, the combined electric and heat power flow model has nonlinear equations and the optimization model has bilinear constraints. These challenges make the power flow, economic dispatch, and frequency control of combined heat and power systems difficult to model and solve.

1.2 Literature Review

1.2.1 Combined Electric and Heat Power Flow Analysis

To overcome the challenges from different time scales and simplifications on system topology and control mechanisms, researchers have made unremitting efforts, which are summarized in Table 1-2. Based on whether the different time scales of electric power systems and heating systems are considered, the power flow research papers are divided into two types: the steady-state analysis [11]-[17] and the dynamic analysis [18]-[29].

Table 1-2. Summary of representative research on power flow analysis.

	Electric power system	Heating system			
Research	Power flow model	Heat dynamic process	Multiple DERs	Loops	Variable mass flow
X Liu-J Wu’16-APEN [15]	AC	×	√	√	√
Z Li-M Shahidehpour’ 16-TSE [27]	DC	√	×	×	√
W Gu-J Wang’17-APEN [25]	DC	√	√	√	×
I B Hassine’13-APTE [22]	-	√	×	√	√
L Wang’17-APEN [29]	AC	×	√	√	√
S Huang-Q. Wu’19-Energy [38]	DC	×	√	√	√
Proposed approach	AC	√	√	√	√

where DERs indicate the distributed energy resources. The AC and DC are the abbreviations of Alternating Current and Direct Current, respectively. The APEN and APTE denote the journals Applied Energy and Applied Thermal Engineering, respectively. The TSE indicates the journal IEEE Transactions on Sustainable Energy.

The steady-state analysis assumes after a change or disturbance both the electric power system and the heating system can reach steady states without dynamic processes. Under this assumption, [11] adopts the simplified power flow model which ignores electric and heat networks. Although the electric and heat networks are considered in [12]-[14] by the Energy Hub model, the networks are neglected or simplified as coefficients. As a result, the power flow calculation may be inaccurate because the electric power flow is influenced by the line impedance while the pipeline parameters can have a significant influence on the heat power flow. To take electric and heat networks into consideration in power flow analysis, papers [15] and [16] have proposed a combined electric and heat power flow model considering detailed network models. More preciously, paper [15] and [16] apply the AC power flow model in the electric power system and consider the meshed network, multiple DERs, and variable mass flow in the heating system. As an extension, paper [17] integrates the building temperature into the power flow analysis. However, the power flow models mentioned in [15]-[17] does not consider the different time scales of electricity and heat, which is not accurate to reflect the heat transmission process.

The dynamic models aim to consider the heat dynamic process in the combined electric and heat power flow analysis ignored by the steady-state model. Since the dynamic process is originally described by partial differential equations, researchers have developed model-based methods [19]-[25] and data-driven methods [28][29] for the complex power flow model.

In the model-based method, complexity from the nonlinear equations and partial differential equations challenges the convergence and accuracy of existing methods, so different levels of simplifications have been made to deal with it. Papers [18]-[21] analyze the power flow of a simple heating system which only has one pipeline. Based on a real-world heating system with loops, [22] proposes the heat power flow analysis methods for the meshed networks, but how to deal with direction-varying mass flow and multiple DERs still needs to be further explored. Besides, papers [18]-[22] only analyze the power flow of the heating system without the electric power system. To analyze the combined electric and heat power flow, authors of [23]-[25] have developed different methods considering the loops and multiple DERs. However, the heat mass flow is assumed to be as the constant. Papers [26] and [27] have developed quasi-dynamic models with a steady-state power system model and dynamic heating system model, but it does not consider multiple DERs and direction-varying mass flow in heating systems, either.

In the data-driven method, paper [28] proposes a black-box method based on the historical data for power flow calculation, which overcomes the nonlinearity caused by the loops in the heating network. Authors of [29] build an individual-based method to reflect the heat dynamic process in the power flow analysis. However, the above data-driven methods need massive and detailed data to train and cannot guarantee accuracy under different circumstances and is not interpretable.

In summary, if the different time scales of electricity and heat are considered without simplifications on topology and control mechanisms, the partial differential equations and nonlinear equations make existing methods difficult to solve. If too many assumptions are imposed on the power flow model, the calculation results cannot reflect the accurate power flow, and the model cannot be generalized. Thus, both the generalized power flow model and the reliable solution method are needed for combined electric and heat power flow analysis.

1.2.2 Economic Dispatch for Combined Heat and Power Systems

Since the heating system may not have the same adjustment time scale as the electric power system as presented in Table 1-1, two frameworks for the economic dispatch of combined heat and power systems are developed in this dissertation and shown in Figure 1-2: synchronous dispatch and asynchronous dispatch. Synchronous dispatch is used by most literature, where the electric power system and the heating system are adjusted with the same time scales. However, when the two energy systems have different adjustment time scales, if the combined economic dispatch adopts the short electric adjustment time scale, a part of heat dispatch command cannot be executed practically; if the dispatch follows the long heat adjustment time scale, some electric load demands cannot be satisfied and the efficiency cannot be guaranteed. This dilemma caused by the synchronous dispatch framework requires the system operators to trade off security and efficiency. Thus, asynchronous dispatch method is needed in combined heat and power systems to optimize the electric power system and the heating system according to their own adjustment time scales.

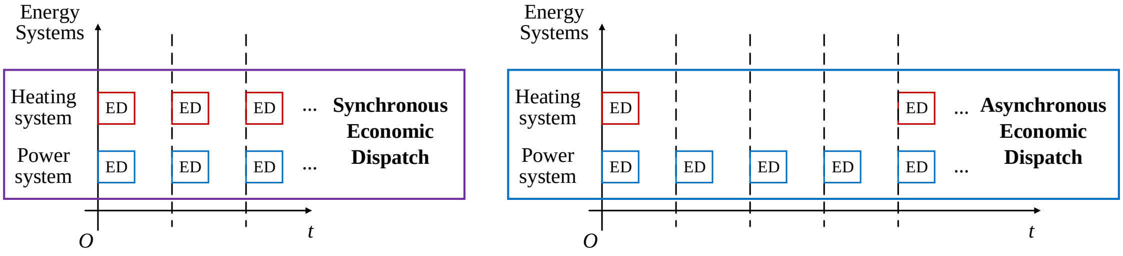

Figure 1-2. Illustration of synchronous and asynchronous economic dispatch (ED) methods.

In this dissertation, we first present the synchronous dispatch with variable mass flow because the hydraulic mass flow can be adjusted as fast as the electric variables. Then we extend the economic dispatch to the asynchronous dispatch which allows the electric power system and the heating system have different adjustment time scales.

1.2.2.1 Synchronous Dispatch with Variable Mass Flow

Temperature and mass flow are the two most important types of control variables in heating systems [30][31]. However, because adjusting mass flow and temperature simultaneously leads to the nonlinearity and non-convexity for the optimization model, many papers only consider varying temperature adjustment, which limits the flexibility of combined heat and power systems [32]. To further increase the adjustable range of heat power and improve the system flexibility, it is crucial to adjust both mass flow and temperature in the heating systems for combined heat and power operation. For clarity, the summary of papers in synchronous economic dispatch is shown in Table 1-3.

Table 1-3. Summary of representative research on synchronous economic dispatch.

Research	Optimization model				Solution Method	
	Electric power system model	Heat dynamic process	Multi-DERs	Variable mass flow	Convergence guaranteed	Summary of method
S Yao-W Gu’18-IEEE Access [41]	DC	√	√	×	√	MIQP
C Lin-W Wu’17-TSE-[23]	DC	√	√	×	√	Convex
S Huang-Q. Wu’19-Energy [38]	DC	×	√	√	√	SOCP
Z Li-M Shahidehpour’ 16-TSE[27]	DC	√	×	√	×	Direct iteration method
Y Chen-H Sun’19-Energy [39]	DC	√	×	√	√	Modified GBD
Proposed approach	DC	√	√	√	√	Modified GBD

where the blocks in grey indicate the optimization models in the papers are non-convex. MIQP is the abbreviation of Mixed-Integer Quadratic Programming, and SOCP is the abbreviation of Second-Order Cone Programming. GBD indicates the Generalized Benders Decomposition [33].

On the economic dispatch of combined heat and power systems, a large part of existing literature assumes the fixed mass flow adjustment in heating systems. The authors of [14] propose a convex dispatch model for Energy Hubs, but the detailed networks still need to be considered to reflect transmission limits. To address the issue of modeling electric and heat networks, papers [34] and [35] adopt different models to consider network constraints, but the heat network dynamic process is simplified. To further utilize the heat dynamic process as a source of flexibility, authors of [23][24][36] formulate convex combined heat and power dispatch programs to accommodate more renewables and reduce costs. Although [23][24][36] consider the flexibility from heat inertia, the mass flow is fixed. As a result, the flexibility of the combined heat and power system is still limited.

For more flexibility and accuracy, other researchers adopt variable mass flow adjustment in their optimal dispatch models. Since adjusting mass flow can cause strong non-convexity, two kinds of methods, i.e., data-driven methods and model-based methods have been developed. The data-driven methods have the same idea as [28] and [29], which treated the non-convex optimization problems as black-boxes and use historical data to predict future states. Although the data-driven methods are effective to deal with non-convex optimization models, they may suffer from problems of interpretability, reliability, and accuracy, especially under different operation strategies. Heuristic algorithms can be embedded in data-driven methods to improve reliability and accuracy. Paper [27] applies a heuristic iterative method for the non-convex economic dispatch model, but the DERs are ignored in this paper. Authors of [37] and [25] develop heuristic methods to solve the Mixed Integer Nonlinear Programming (MINLP) considering DERs which introduce nonlinear constraints. Unfortunately, due to the bilinear constraints and integers in the MINLP model, the solution methods based on the heuristic methods may suffer from problems in convergence and interpretability.

Recently, some model-based methods have been proposed to address the trackability and convergence problems. However, optimization models are simplified. For example, heat dynamic process is not considered in [15][38], as a result, the methods in the two papers are hard to ensure accuracy and convergence simultaneously due to other bilinear constraints. The authors of [39] have proposed the modified GBD to overcome GBD’s inability of solving non-convex problems, but there are varying degrees of simplification and approximation in the dispatch model and the solution method. Moreover, paper [39] does not consider multi-DERs, either. Although these simplifications on models help to make the optimization model solvable, they impede the accuracy and may threaten the system’s security.

In brief, the synchronous economic dispatch model with variable mass flow provides more flexibility for the combined heat and power system, but its non-convexity challenges the convergence and reliability of existing solution methods. Although simplifications and approximations help to make the optimization model easier to solve, the efficiency and accuracy can be affected in varying degrees. Thus, on the synchronous economic dispatch with variable mass flow, it is essential to reduce the model complexity from integers and propose the solution method with improved convergence and acceleration.

1.2.2.2 Asynchronous Economic Dispatch

As presented in Table 1-1, it is not safe to assume that in all circumstances the electric power system and the heating system have the same adjustment time scales. Thus, the asynchronous economic dispatch is needed to incorporate the different adjustment time scales of electricity and heat.

However, most existing literature assumes the same adjustment time scales of electricity and heat. For example, authors of [23] and [36] use the pipeline storage ability from the heat dynamic process to accommodate more renewables. Also, the building heat inertia is considered in [24] to provide additional flexibility. Moreover, some research papers like [15][38]-[40] adopt the variable mass flow adjustment in the heating system. Unfortunately, the above research papers all assume the heating system can respond to dispatch commands as fast as the electric power system, which is too ideal in practice.

To address the challenge of different adjustment time scales of the electric power system and the heating system, some researchers utilize hierarchical dispatch methods. An instance is that paper [41] proposes a hierarchical way to dispatch the combined heat and power system, which eliminates the dispatch error caused by different adjustment time scales layer by layer. However, because the power system and the heating system still have the same adjustment time scale in each layer, if the time scale is selected too long, the fast adjustment ability of the power system will be wasted; if it is too short, the heating system cannot respond to the command due to the slow dynamic process. Although [29], [41]-[43] propose different hierarchical models to relieve the problems caused by the different adjustment time scales, the traditional synchronous dispatch methods in each layer will still have a negative impact on system efficiency and security because of ignoring the different adjustment time scales for electricity and heat. Recently, an improvement has been made to step to the asynchronous dispatch by operating the combined heat and power system according to each energy system's adjustment time scale. The paper [44] discusses the framework of asynchronous economic dispatch, however, the optimization model and the necessity of using asynchronous dispatch are not included.

In summary, the different adjustment time scales of electricity and heat should be considered in the economic dispatch if the electric power system and the heating system have different adjustment time scales.

1.2.3 Frequency Control for Combined Heat and Power System

Traditionally, the secondary frequency control (also called Automatic Generation Control, AGC) employs a hierarchical model with a centralized control center [45][46]. But currently this strategy faces challenges due to expensive ramping reserves, heavy communication burden among a large number of DERs, and slow reaction because the time scales of each optimization layer are different. Besides, in the combined heat and power systems, electric-heat coupling devices' electric power output is dependent on the heat power output. Thus, traditional centralized control in the electric power system cannot be directly used in the combined heat and power system. To make it clear, the representative research papers on the secondary frequency control are summarized in Table 1-4 and detailed in the following paragraphs.

Table 1-4. Summary of representative research on optimal frequency control.

Research	Optimal control model				Solution Method	Global Optimality
	Electric-heat coupling	Electric line power limit	Measuring phase angle	Inaccurate coefficient	Distributed method	
H Liu’15-TPS [49]	×	√	-	×	×	×
Y Xu’18-TSG [52]	×	√	√	×	√	×
Y Xu’19-TII [53]	×	×	√	×	√	√
N Li’16-TEG [54]	×	×	-	√	√	√
E Mallada-S Low’17-TAC [55]	×	√	×	×	√ (semi)	√
X Chen’18-CCTA [56]	×	√	×	√	√	√
I Beil-I Hiskens’16-PIEEE [58]	√	-	-	-	×	×
T Sun’18-TSG [59]	√	×	-	-	×	×
Proposed approach	√	√	×	√	√	√

where TPS indicates the journal IEEE Transactions on Power Systems, and TSG indicates the journal IEEE Transactions on Smart Grid. TAC and TII denote the journals IEEE Transactions on Automatic Control and IEEE Transactions on Industrial Informatics, respectively. TEG is the journal IEEE Transactions on Control of Network Systems, and CCTA indicates the conference IEEE Conference on Control Technology and Applications. PIEEE denotes the Proceedings of the IEEE.

In the electric power system, researchers have proposed distributed frequency management by controlling some types of loads and devices. For example, flexible load demand is utilized in [47] and [48] to respond to frequency regulation signals. Moreover, electric vehicles [49] and battery storage systems [50] are also controlled to provide ancillary services and realize load-side frequency management. These works illustrated how to model and control specific types of loads and devices, however, the system-wide optimality might not be guaranteed at the same time. To address this issue, paper [51] proposes a distributed proportional-integral load controller. Papers [52] and [53] develop distributed optimal control schemes to regulate frequency and voltage. Nevertheless, some reliability constraints such as load power and line power flow limits are not considered. Based on the reverse engineering, papers [54]-[56] design distributed control manners to restore frequency with system-wide optimality, line thermal limit, and guaranteed convergence under inaccurate coefficient, where [56] realizes the fully distributed algorithm with only neighborhood communication and does not need an accurate measurement of parameters. However, the methods above may not work well in the combined heat and power systems because of ignoring the electric-heat coupling constraints of generators. As a result, if we directly apply the frequency control methods above in the combined heat and power system, the electric power adjustment may violate the operating constraints of electric-heat coupling devices like CHP units, which menaces the stability of frequency.

In the combined heat and power systems, paper [57] realize frequency regulation by adjusting water boiler, [58] uses heating, ventilation, and air-conditioning devices to support frequency regulation, and [59] adopts CHP units for microgrid frequency management. However, the system-wide optimality is not considered above, and the flexibility from heating networks or buildings are not fully exploited.

In summary, on the secondary frequency control of combined heat and power systems, existing centralized control methods bring the system with heavy communication and computation burdens, while some distributed control methods cannot guarantee the system-wide optimality and ignore security constraints. Thus, the distributed frequency control manner with system-wide optimality is needed with the consideration of electric-heat coupling devices, electric line power limits, and inaccurate coefficients.

1.3 Outline and Framework

The framework of this dissertation and the relationship between different chapters are shown in Figure 1-3. Different chapters in this dissertation play different roles in the Integrated Energy Management System [5]: The method for combined electric and heat power flow analysis is developed in Chapter 2. In Chapters 3 and 4, economic dispatch methods are proposed for different operation scenarios: Chapter 3 is for the synchronous dispatch of the combined heat and power system with variable mass flow, and Chapter 4 is the asynchronous dispatch method which incorporates the different adjustment scales of electricity and heat. Based on the results of economic dispatch, Chapter 5 propose the secondary frequency control method to restore the frequency and eliminate the power unbalance between generation and load sides.

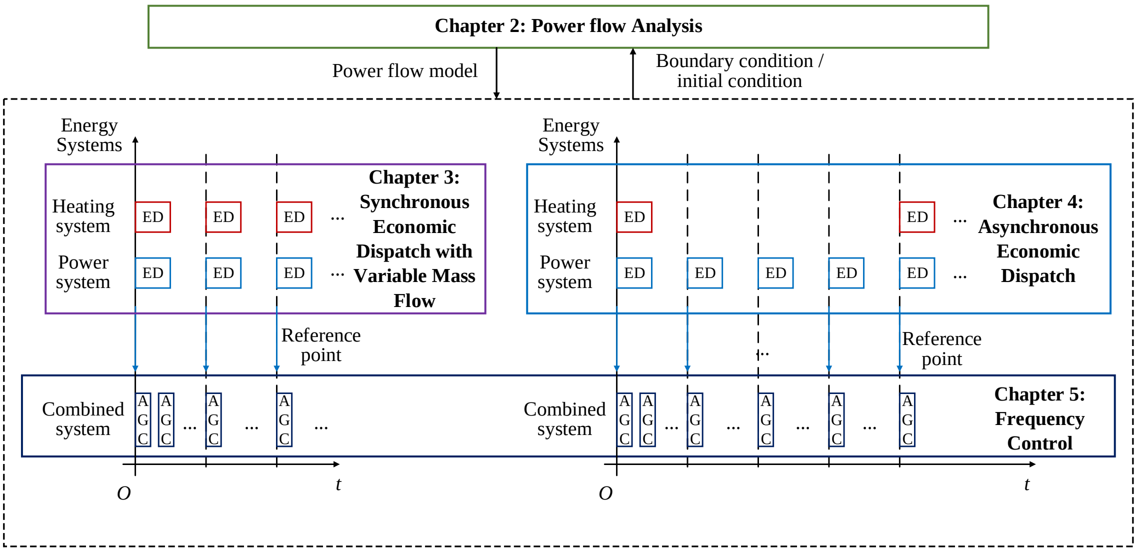

Figure 1-3. The framework of the dissertation.

From another point of view, Chapters 3-5 constitutes a hierarchical dispatch framework to optimize the combined heat and power system layer by layer, and Chapter 2 provides the power flow analysis methods and the optimization constraints for Chapter 3-5.

1.4 Contribution

This dissertation develops the power flow analysis and optimization methods for combined heat and power systems, whose key contribution is to consider different time scales of the electric power system and the heating system with weak simplifications on system topology and control mechanism. Compared with existing research, the contributions are summarized as follows and illustrated in Table 1-4.

Table 1-4. Overview of contributions of this dissertation.

		Model formulation	Solution method
Chapter 2	Power flow analysis	Develop a generalized model considering different dynamic time scales, non-simplified topology and control mechanisms	Propose a decomposition method with improvement in convergence and efficiency
Chapter 3	Synchronous economic dispatch	1) Consider the flexibility from heat dynamic process and variable mass flow, 2) Reduce the complexity from integers	Propose a solution method for the non-convex program with improved convergence and acceleration
Chapter 4	Asynchronous economic dispatch	Propose asynchronous time scale dispatch models with different electric and heat dispatch intervals	Study the influence of dispatch intervals on cost and computational efficiency
Chapter 5	Frequency control	1) Design a control mechanism with system-wide optimality, 2) Consider electric-heat coupling device models, line thermal limits, and inaccurate coefficients	Propose a fully-distributed control method with globally asymptotical stability

1) On power flow analysis, a generalized power flow model is developed in which the AC power flow model in power systems and the heat dynamic process, variable mass flow, meshed network, and multiple DERs in heating systems are considered. Then a decomposition solution method is proposed to solve the nonlinear power flow model sequentially and iteratively with the improvement in the convergence compared with existing methods. The data from the practical system, and the comparisons with the commercial software and research papers demonstrate the effectiveness of the proposed method.
2) On the synchronous economic dispatch with variable mass flow, a non-convex economic dispatch model is developed to remove integers in existing models without compromising on the accuracy. An efficient solution method is proposed for the developed model with acceleration and improved convergence.

3) On the asynchronous economic dispatch, asynchronous dispatch models are proposed which incorporates the different adjustment time scales of the electric power system and the heating system. Also, the influence of dispatch intervals on the total cost and computational efficiency is studied in the case simulation, and the necessity of using asynchronous dispatch is demonstrated from the comparison with the traditional dispatch method.
4) On the frequency control, a fully-distributed frequency control mechanism with system-wide optimality is developed considering the model of the electric-heat coupling device, line power flow limits, and the inaccuracy of damping coefficients.

Chapter 2: Combined Electric and Heat Power Flow Analysis

2.1 Overview

The combined electric and heat power flow analysis calculates the power flow distribution in the electric power system and the heating system, which provides basic information for the security analysis. In this chapter, a generalized power flow analysis method is proposed for combined heat and power systems for accurate and efficient calculation. The advantages are:

1) The proposed power flow model requires weaker assumptions on topology and control mechanisms, where the AC power flow in power systems and the heat dynamic process, loops, multiple DERs, and direction-variable mass flow in heating systems are considered simultaneously.
2) A decomposition solution method is developed to divide complicated nonlinear power flow equations into small parts and solve them sequentially and iteratively, whose convergence surpasses existing methods.
3) The accuracy and applicability of the proposed method have been demonstrated with comparisons to data from real systems and methods in the existing literature: the proposed method has an average error of 0.09% compared with real measured data and surpasses commercial software in terms of pipe temperature dynamics.

2.2 Physical Model

The combined heat and power system incorporates two different energy systems i.e., electric power system and district heating system with diverse characteristics: First, as shown in Figure 2-1, the dynamic time scales of electricity and heat are different: In the time scale of power flow analysis, the electric power system and the hydraulic process in the heating system have already reached the steady states, but the heat thermal process is still in the dynamic state [17][60], which needs to be described by the partial differential equations. Second, the power system and the heating system may have different network topologies. Third, the power system and heating system have different control mechanisms for reliability and efficiency. For example, variable mass flow adjustment is adopted in the heating system to improve efficiency [27][61], but there are no similar strategies in the electric power system.

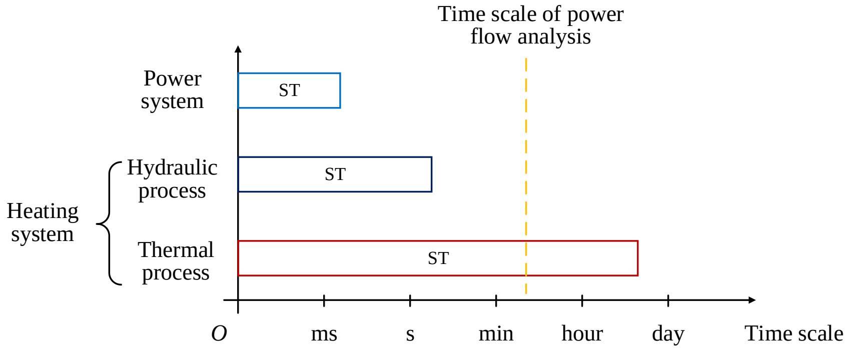

Figure 2-1. The steady-state time (ST) after disturbance of different energy systems.

Considering the above physical differences between the two energy systems, it is essential to model the power system and heating system respectively according to the characteristics of each system. Figure 2-2 uses an example to show the physical model of the combined heat and power system, where the electric power system and the heating system are coupled with electric-heat coupling devices. Energy sources include thermal generator, electric-heat coupling devices like CHP unit and electric boiler, electricity from the main grid, etc.

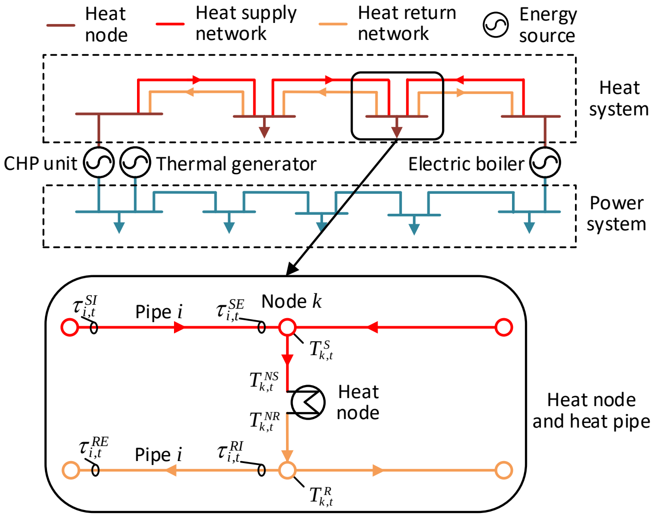

Figure 2-2. The physical structure of combined heat and power system.

As presented in Figure 2-2, the heating system consists of heat nodes, heat supply network, and heat return network. In the heating system, heat is transmitted by media, which is assumed to be water in this dissertation. Unlike electric power systems, a heat node has to use the heat exchanger to get heat from the heating network. The load node heat exchangers obtain heat from high-temperature water in the supply network and release the low-temperature water to the return network. For clarity, the variables with the form τ and *T* are used to denote the pipe temperature and the node temperature in the following parts, respectively. In the supply network, the node temperature $T_{i,t}^{S}$ indicates the temperature after mixing, and the node exchanger supply temperature $T_{i,t}^{NS}$ indicates the temperature before mixing. The same is true in the return network.

2.3 Power Flow Model

The power flow model of combined heat and power systems are relatively mature. As shown in Figure 2-1, in the power flow analysis, steady-state models are used in the electric power system and the hydraulic process in the heating system, and the dynamic model is used in the thermal process in the heating system [17].

2.3.1 Model of Electric Power System

The AC power flow model is adopted in the electric power system. The variables of the power system are bus voltage, phase angle, active power, and reactive power.

The voltage of the bus *i* is denoted by

$$V_{i,t} = |V_{i,t}|(\cos\theta_{i,t} + j\sin\theta_{i,t}) \quad \forall i \in E,\ t=1, 2, \cdots T, \tag{2-1}$$

where $|V_{i,t}|$ and $\theta_{i,t}$ are the voltage magnitude and phase angle of bus *i* at time *t*. Set *E* is the set of buses in the electric power system, and *T* indicates the number of total time sections.

The complex power injection of bus *i* are calculated by

$$S_{i,t} = p_{i,t} + jq_{i,t} = V_{i,t}\sum_{j=1}^{n_E}(Y_{ij}V_{j,t})^{*} \quad \forall i \in E,\ t=1, 2, \cdots T, \tag{2-2}$$

where $S_{i,t}$, $p_{i,t}$ and $q_{i,t}$ are the complex power, the active power, and the reactive power of bus *i* at time *t* respectively. The Y_{ij} indicates the admittance from node *i* to *j*, and the n_E is the number of buses in the electric power system.

2.3.3 Model of Heating System

This section presents the steady-state hydraulic model and the dynamic thermal model. The variables in the heating system include node/pipe mass flow, node pressure, and pipe pressure drop in the hydraulic model and node temperatures in supply/return network, node exchanger supply/return temperatures, and pipe initial/end temperatures in the thermal model.

2.3.3.1 Hydraulic Model

The hydraulic model describes the relationship between the mass flow and pressure distribution in the heating system. The hydraulic model is based on Kirchhoff's law [62], which is similar to that in the electric power system as shown in Table 2-1.

Table 2-1 The comparison of Kirchhoff's law in hydraulic system and electric power system

Kirchhoff's law in	Calculating node	Calculating loop	Calculating single branch
Electric power system	Kirchhoff's current law	Kirchhoff's voltage law	Ohm's law
Hydraulic system	Continuity of flow equation	Pressure drop equation	Head loss equation

First, the continuity of flow equation is expressed as the mass flow consumed at a node is equal to the difference between the mass flow injecting into the node, and the mass flow leaving from the node:

$$\sum_{i\in In(k)\cap P_S} m_{i,t} - \sum_{j\in Lv(k)\cap P_S} m_{j,t} = m^n_{k,t} \quad \forall k\in H,\ t=1,2,\cdots T\,, \tag{2-3a}$$

$$\sum_{i\in In(k)\cap P_R} m_{i,t} - \sum_{j\in Lv(k)\cap P_R} m_{j,t} = m^n_{k,t} \quad \forall k\in H,\ t=1,2,\cdots T\,, \tag{2-3b}$$

where $m^n_{i,t}$ is the node mass flow of node *i* at time *t*, and $m_{j,t}$ indicating the pipe mass flow of pipe *j* at time *t*. Set *H* is the set of heat nodes in the heating system. Sets P_S and P_R indicate the sets of pipelines in heat supply and return networks, respectively. Sets $In(i)$ and $Lv(i)$ are sets of pipelines injecting into and leaving from node *i*.

Second, the pressure drop equation illustrates the sum of head pressure losses of a closed-loop in the supply or return network equals to zero:

$$\sum_{i\in P_S\cap LP_S} h^p_{i,t} = 0 \quad t=1,2,\cdots T\,, \tag{2-4a}$$

$$\sum_{i\in P_R\cap LP_R} h^p_{i,t} = 0 \quad t=1,2,\cdots T\,, \tag{2-4b}$$

where $h_{i,t}^{p}$ is the head pressure loss of pipe *i* at time *t*. Sets LP_S and LP_R denote the set of loops in heat supply and return networks, respectively.

Third, the head loss equation calculates the head loss of a pipe from the mass flow:

$$h_{i,t}^{p} = K_{i,t}^{p} \left| m_{i,t} \right| m_{i,t} \quad \forall i \in P_S,\ t=1,\ 2,\ \cdots T\ , \tag{2-5a}$$

$$h_{i,t}^{p} = K_{i,t}^{p} \left| m_{i,t} \right| m_{i,t} \quad \forall i \in P_R,\ t=1,\ 2,\ \cdots T\ , \tag{2-5b}$$

where $K_{i,t}^{p}$ is the pipe resistance coefficient of pipe *i* at time *t*, and the calculation of $K_{i,t}^{p}$ is detailed in [63].

For clarity, the node-branch incidence matrix ***A*** and the loop-branch matrix ***B*** are introduced to describe the heating system topology [22], where

$$A_{i,j} = \begin{cases} +1, \text{ the mass flow of pipe } j \text{ comes into node } i \\ -1, \text{ the mass flow of pipe } j \text{ leaves from node } i \\ 0, \text{ no connection from pipe } j \text{ to node } i \end{cases},$$

$$B_{i,j} = \begin{cases} +1, \text{ the mass flow of pipe } j \text{ is the same as the direction of loop } i \\ -1, \text{ the mass flow of pipe } j \text{ is not the same as the direction of loop } i \\ 0, \text{ no connection from pipe } j \text{ to loop } i \end{cases}.$$

Then the three hydraulic equations can be written as:

$$\boldsymbol{A}\,\boldsymbol{m}_t = \boldsymbol{m}_t^{n}\,, \tag{2-6}$$

$$\boldsymbol{B}\,\boldsymbol{h}_t^{p} = \boldsymbol{0}\,, \tag{2-7}$$

$$\boldsymbol{h}_t^{p} = \boldsymbol{K}_t^{p} \left| \boldsymbol{m}_t \right| \boldsymbol{m}_t\ , \tag{2-8}$$

where $\boldsymbol{m}_t$ and $\boldsymbol{m}_t^{n}$ are matrices of $m_{i,t}$ and $m_{i,t}^{n}$, respectively. Matrix $\boldsymbol{h}_t^{p}$ is the matrix of $h_{i,t}^{p}$, and $\boldsymbol{K}_t^{p}$ is the matrix of $K_{i,t}^{p}$.

2.3.3.2 Thermal Model

Since the dynamic time of the thermal process in the heating system varies from several minutes to hours, the dynamic thermal model is formulated in this section to track the heat dynamic process. To describe the network temperature, the pipeline temperature equations and the node temperature equations are included in the thermal model as shown in Figure 2-3. Figure 2-3 also presents the steps of dealing with pipe heat conductive equation (2-9) and the relationship between different equations [22][64]. It is noticed that steps from (2-9) to (2-13) is to transform the partial differential equation (2-9) into a solvable form by simplifying the differential term and applying the finite difference method.

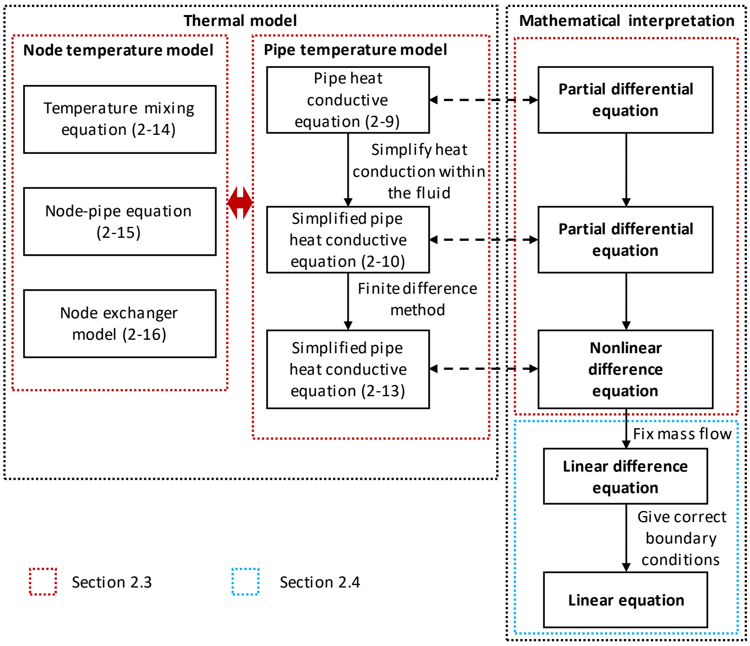

Figure 2-3. The relationship of different equations in thermal model.

The pipe heat conductive equation is a partial differential equation which describes the pipe temperature distribution $\tau_i^S(x,t)$ and $\tau_i^R(x,t)$ [18][22], take supply network for an example:

$$\rho c_p A_i \frac{\partial \tau_i^S(x,t)}{\partial t} + m_i(x,t)\cdot c_p \frac{\partial \tau_i^S(x,t)}{\partial x} = kA_i \frac{\partial^2 \tau_i^S(x,t)}{\partial x^2} + \frac{T_{i,t}^a - \tau_i^S(x,t)}{R_i} \quad \forall i \in P_S\,, \qquad (2\text{-}9)$$

where $\tau_i^S(x,t)$ and $\tau_i^R(x,t)$ denote pipe temperatures of pipe i in heat supply and return networks at distance x from the pipe start point at time t, respectively. Scalar $m_i(x,t)$ is the pipe mass flow at distance x at time t. Scalars k, ρ and c_p are thermal conductivity, density, and capacity of water, respectively. Scalars A_i and R_i are the cross-sectional area and the pipeline heat conductive coefficient of pipe i, respectively.

Since the hydraulic process is in the steady state, pipe mass flow is the same everywhere i.e., $m_i(x,t) = m_{i,t}$. Also, considering the heat conduction within the fluid can be neglected [18], (2-9) changes to:

$$\rho c_p A_i \frac{\partial \tau_i^S(x,t)}{\partial t} + m_{i,t} c_p \frac{\partial \tau_i^S(x,t)}{\partial x} = \frac{T_{i,t}^a - \tau_i^S(x,t)}{R_i} \quad \forall i \in P_S\,, \qquad (2\text{-}10)$$

Use Taylor expansion and finite difference method [71] for (2-10):

$$\frac{\partial \tau_i^S(x,t)}{\partial t}=\frac{\tau_i^S(x,t)-\tau_i^S(x,t-1)}{\Delta t} \quad \forall i\in P_S,\ t=1,2,\ \ldots T,\ x=1,2,\ldots S_i, \tag{2-11a}$$

$$\frac{\partial \tau_i^S(x,t)}{\partial x}=\frac{\tau_i^S(x,t)-\tau_i^S(x-1,t)}{\Delta x} \quad \forall i\in P_S,\ t=1,2,\ \ldots T,\ x=1,2,\ldots S_i, \tag{2-11b}$$

where Δt and Δx are the given time and length segment intervals, respectively. Scalar S_i indicates the number of segment sections of pipe *i*, in which $S_i=\lceil x_i/\Delta x\rceil$, where x_i is the length of pipe *i*. It is noticed that 1) equations in the return network has the same form as (2-9)-(2-11), and 2) the *t* and *x* in (2-11) are discrete variables. The choice of Δt and Δx should satisfy:

$$\left(\Delta x\right)_{\min}\geq\frac{m_{i,t}\Delta t}{A_i\rho} \quad \forall i\in P_S\cup P_R,\ t=1,2,\ \ldots T. \tag{2-12}$$

Finally substitute (2-11) into (2-10). The partial differential equation (2-10) is transformed into the nonlinear difference equation in (2-13) [22].

$$\tau_i^S(x,t)=\frac{1}{\dfrac{1}{\Delta t}+\dfrac{m_{i,t}}{\Delta x\rho A_i}+\dfrac{1}{\rho c_p A_i R_i}}\left[\frac{T_{i,t}^a}{\rho c_p A_i R_i}+\frac{m_{i,t}}{\Delta x\rho A_i}\tau_i^S(x-1,t)+\frac{1}{\Delta t}\tau_i^S(x,t-1)\right], \tag{2-13a}$$
$$\forall i\in P_S,\ t=1,\ 2,\ \ldots T,\ x=1,2,\ldots S_i$$

$$\tau_i^R(x,t)=\frac{1}{\dfrac{1}{\Delta t}+\dfrac{m_{i,t}}{\Delta x\rho A_i}+\dfrac{1}{\rho c_p A_i R_i}}\left[\frac{T_{i,t}^a}{\rho c_p A_i R_i}+\frac{m_{i,t}}{\Delta x\rho A_i}\tau_i^R(x-1,t)+\frac{1}{\Delta t}\tau_i^R(x,t-1)\right], \tag{2-13b}$$
$$\forall i\in P_R,\ t=1,\ 2,\ \ldots T,\ x=1,2,\ldots S_i$$

where $\tau_i^S(0,t)=\tau_{i,t}^{SI}$, $\tau_i^S(S_i,t)=\tau_{i,t}^{SE}$, $\tau_i^R(0,t)=\tau_{i,t}^{RI}$, $\tau_i^R(S_i,t)=\tau_{i,t}^{RE}$, in which $\tau_{i,t}^{SI}$ and $\tau_{i,t}^{RI}$ denote pipe start temperatures of pipe *j* at time *t* in heat supply and return networks, respectively. Scalars $\tau_{i,t}^{SE}$ and $\tau_{i,t}^{SE}$ denote the pipe end temperature of pipe *j* at time *t* in heat supply and return networks, respectively.

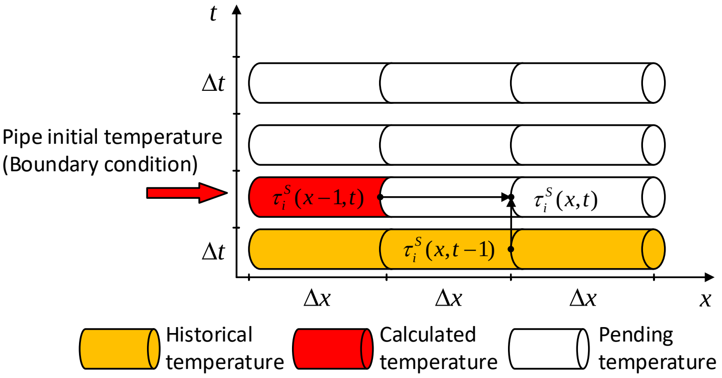

Figure 2-4. The physical illustration of pipe temperature calculation.

Figure 2-4 presents the physical illustration of (2-13), which indicates that the current temperature is calculated by not only the current state but also the former state. Hence, if the boundary condition (pipe initial temperature $\tau_{i,t}^{SI}$ and $\tau_{i,t}^{RI}$) and pipe mass flow are given, the pipe temperature distribution in a pipe can be calculated according to (2-13).

For the heat nodes, if there are more than two pipes injecting into a node, the temperature mixing equations (2-14) are applied to calculate node temperature:

$$\begin{gathered}\left(m_{i\in H_G,t}^{n}+\sum_{j} m_{j,t}\right)T_{i,t}^{S}=\left(m_{i\in H_G,t}^{n}T_{i\in H_G,t}^{NS}\right)+\left(\sum_{j} m_{j,t}\tau_{j,t}^{SE}\right),\\ \forall i\in H,\ j\in P_S\bigcap In(i),\ t=1,2,\ \ldots T\end{gathered} \tag{2-14a}$$

$$\begin{gathered}\left(m_{i\in H_L,t}^{n}+\sum_{j} m_{j,t}\right)T_{i,t}^{R}=\left(m_{i\in H_L,t}^{n}T_{i\in H_L,t}^{NR}\right)+\left(\sum_{j} m_{j,t}\tau_{j,t}^{RE}\right).\\ \forall i\in H,\ j\in P_R\bigcap In(i),\ t=1,2,\ \ldots T\end{gathered} \tag{2-14b}$$

where $T_{i,t}^{NS}$ and $T_{i,t}^{NR}$ are the exchanger supply and return temperatures of node *i* at time *t*, respectively. Scalars $T_{i,t}^{S}$ and $T_{i,t}^{R}$ are the node temperatures of node *i* at time *t* in supply and return networks. Sets H_G and H_L are sets of heat source nodes and heat load nodes, respectively, where $H=H_G\bigcup H_L$.

The pipe initial temperature equals to the temperature of its connecting node:

$$\tau_{i,t}^{SI}=T_{i,t}^{S}\quad \forall i\in H,\ j\in P_S\bigcap Lv(i),\ t=1,2,\ \ldots T\ , \tag{2-15a}$$

$$\tau_{i,t}^{RI}=T_{i,t}^{R}\quad \forall i\in H,\ j\in P_R\bigcap Lv(i),\ t=1,2,\ \ldots T\ . \tag{2-15b}$$

The nodes exchange heat power with the heat supply and return networks through heat exchangers [27][65][66]:

$$h_{i,t}=c_p m_{i,t}^{n}(T_{i,t}^{NS}-T_{i,t}^{NR})\quad i\in H,\ t=1,2,\ \ldots T\ , \tag{2-16}$$

where $h_{i,t}$ is the heat power of node *i* at time *t*. In the heat supply network, for load nodes $T_{i,t}^{NS}=T_{i,t}^{S}$, and for source nodes $T_{i,t}^{S}$ is calculated by (2-14a). Similarly, in the heat return network, for load nodes $T_{i,t}^{R}$ is calculated by (2-14b), and for source nodes $T_{i,t}^{NR}=T_{i,t}^{R}$.

2.3.2 Model of Energy Sources

As presented in (2-17), the energy sources including CHP units, thermal generators, and other DERs are modeled as the model of CHP units whose feasible region of electric power and heat power is described by the polytopes [36][67]:

$$B_{k,i}p_{i,t}+K_{k,i}h_{i,t}\le v_{k,i}\quad \forall i\in G,\ \forall k\in NK_i,\ t=1,\ 2,\ \ldots T, \tag{2-17}$$

where $B_{k,i}$, $K_{k,i}$ and $v_{k,i}$ are coefficients of the k th boundary of the feasible operating region of CHP unit i. Set NK_i is the set of boundary lines in the feasible operating region of CHP unit i, and G denotes the set of energy sources. For example, Figure 2-5 (a) and (b) present the models of an extraction condensing CHP unit and a back-pressure CHP unit described by (2-17), respectively. It is also noteworthy that a thermal unit can be modeled as a CHP unit with zero heat output, and a heat pump can be modeled as a CHP unit with the negative electric output.

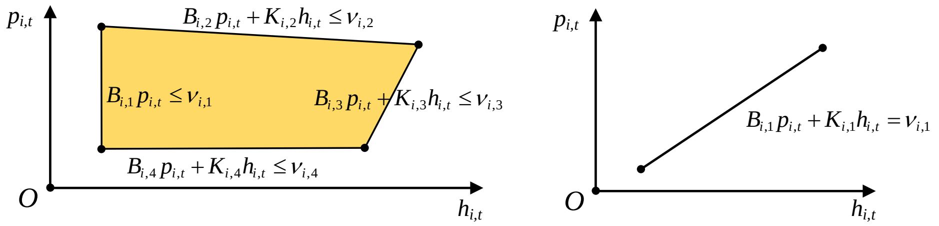

(a) (b)

Figure 2-5. The feasible region of (a) extraction condensing CHP unit and (b) back pressure CHP unit.

2.4 Solution Method: Heat Electric Forward Backward Iteration (HE-FBI) Method

2.4.1 Basic Idea

For clarity, the power flow model is generalized as the following form:

$$\boldsymbol{F}(\boldsymbol{x})=\begin{bmatrix} f_{11}(\boldsymbol{x}) & \cdots & f_{1m}(\boldsymbol{x}) \\ \vdots & \ddots & \vdots \\ f_{n1}(\boldsymbol{x}) & \cdots & f_{1n}(\boldsymbol{x}) \end{bmatrix}=\boldsymbol{0}, \tag{2-18}$$

where $\boldsymbol{x}$ is the matrix of variables and $f_{i,j}(\boldsymbol{x})$ indicates the general form of power flow equations including (2-1)-(2-2), (2-6)-(2-8), and (2-13)-(2-17).

The electric and heat power flow distribution can be obtained after solving (2-18), however, this work is challenging because:

1) There are nonlinear equations in (2-18) including (2-1), (2-2), (2-7), (2-8), (2-13), (2-14), and (2-16).
2) The initial conditions and boundary conditions of difference equation (2-13) are

unknown variables, and the boundary conditions are changing with the direction of $m_{i,t}$.

3) The close-form expression of (2-14) also depends on the direction of $m_{i,t}$.
4) The electric power system uses per-unit values, while the heating system uses the real value.

Therefore, the integrated solution method in [15] and [63] which treats (2-18) as a whole cannot be used here due to the accuracy and convergence problems caused by the above challenges. Therefore, a decomposition method based on the fixed-point iteration is proposed in this section, whose flow chart is shown in Figure 2-6.

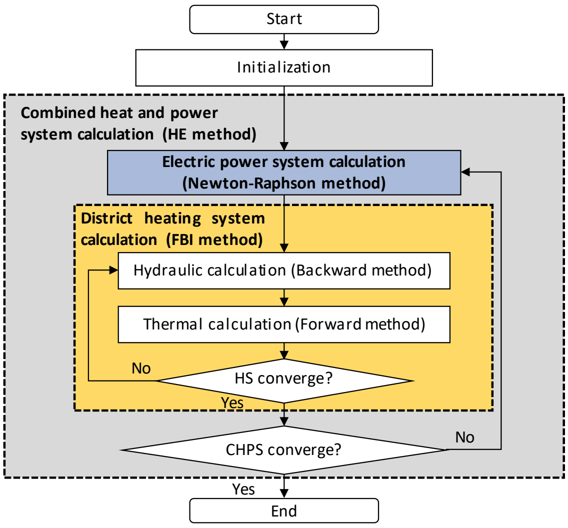

Figure 2-6. Flow chart of HE-FBI method, where HS is the abbreviation of heating system and CHPS denotes combined heat and power system.

The solution method in Figure 2-6 is called Heat-Electric Iteration with Forward-Backward Iteration (HE-FBI) method, which has a similar framework but different algorithms compared with the decomposition method in [63]. As illustrated in the gray block of Figure 2-6, the "HE" indicates Heat-Electric iteration dealing with the coupling of electricity and heat for the whole system. As presented in the yellow block in Figure 2-6, the "FBI" indicates the Forward-Backward Iteration in the heating system for the coupling of the hydraulic process and the thermal process.

Mathematically, the HE-FBI method decomposes (2-18) into small parts according to the physical nature of different energy systems and solves each part in the sequentially and iteratively.

2.4.2 Assumptions

To solve the power flow model, several general assumptions are clarified in Table 2-2. It can be observed from Table 2-2 that the proposed power flow model with the solution method is a generalized method with few assumptions on the combined heat and power systems.

Table 2-2. Assumptions of the power flow model

Type	Assumptions
Network topology	arbitrary
Mass flow in heating system	variable (including direction)
Media	water
Node type (Boundary condition)	3 types

Node types in the electric power system and the heating system are presented in Table 2-3 according to the operating and control mechanism [18][15][63]. For more details, see [63].

Table 2-3. Node types in power flow calculation

Bus type in electric power system	Node type in heating system	Example
pV bus	hT^{NS} node	Generator (CHP unit)
pQ bus	hT^{NR} node	Load user
Slack bus ($V\theta$ bus)	Slack node (h^pT^{NS} node)	Slack generator

2.4.3 Heat-Electric Iteration

As shown in the gray block at Figure 2-6, the Heat-Electric (HE) iteration for the combined heat and power system decomposes the calculation of the electric power system and the heating system by fixing and iterating the boundary powers.

$$\begin{tikzcd}
\text{Electric power balance} & p_{es} \arrow[d, "\text{eq.(2-17)}"] & + & p_{hs} & + \; p_{other} = p_{load} + p_{loss} \\
\text{Heat power balance} & h_{es} & + & h_{hs} \arrow[u, "\text{eq.(2-17)}"'] & + \; h_{other} = h_{load} + h_{loss}
\end{tikzcd}$$

Figure 2-7. Illustration of Heat-Electric iteration process.

Considering the electric power system and the heating system each has one slack node, respectively [15], in Figure 2-7, the steps of the HE iteration are:

1. Give the electric power outputs p_{other} and the heat power outputs h_{other} of other generators at non-slack nodes using equation (2-17).
2. Calculate electric power flow and then compute the heat power h_{es} of the electric slack node from its electric power p_{es}.
3. Calculate heat power flow and then compute the electric power p_{hs} of the heat slack node from its heat power h_{hs}.

The electric and heat power outputs in step 1 are given conditions that can be provided by economic dispatch and injecting power flow from other areas. The iteration of step 2 and step 3 is based on the linear equation (2-17) and continues until the heat and electric power outputs of two slack nodes converge. After that, the system power flow is obtained. The concrete calculation methods for the electric power system and the heating system are shown in the following text.

2.4.4 Electric Power System Calculation: Newton-Raphson Method

To calculate the nonlinear electric power flow equations, the well-known Newton-Raphson method is applied in the electric power system. The iterative form of the Newton-Raphson method is:

$$\begin{bmatrix} \boldsymbol{V} \\ \boldsymbol{\theta} \end{bmatrix}^{k+1} = \begin{bmatrix} \boldsymbol{V} \\ \boldsymbol{\theta} \end{bmatrix}^{k} - \left(\boldsymbol{J}_e^{-1} \begin{bmatrix} \boldsymbol{\Delta q} \\ \boldsymbol{\Delta p} \end{bmatrix} \right)^{k},$$

where k indicates the iteration times. $\boldsymbol{V}$ and $\boldsymbol{\theta}$ are the vectors of the bus voltage and the phase angle respectively. Matrix $\boldsymbol{J}_e$ is the Jacobian matrix in the electric power system. Matrices $\boldsymbol{\Delta q}$ and $\boldsymbol{\Delta p}$ are matrices of active and reactive power mismatches, respectively [68].

2.4.5 Heating System Calculation: Forward-Backward Iteration

Based on the fixed-point method, the Forward-Backward Iteration (FBI) is proposed to deal with the complexity caused by nonlinear equations and difference equations in the heating system. Figure 2-8 is the flow chart of the FBI method.

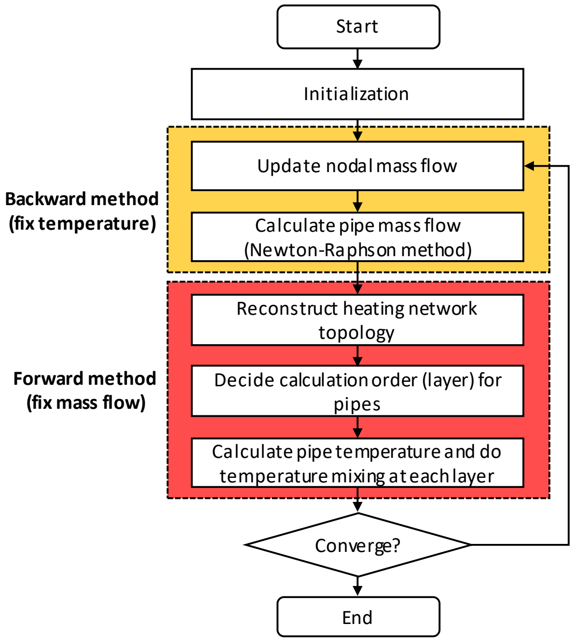

Figure 2-8. Flow chart of Forward-Backward Iteration method.

Table 2-4. Comparison of the proposed FBI method and forward-backward sweep method in the electric power system

	Similarities		**Differences**	
	Forward step	Backward step	Direction	Topology
Proposed FBI method	Calculate temperature with fixed mass flow	Calculate mass flow with fixed temperature	Mass flow cannot be negative	Topology reconstructing in each iteration
Forward-backward sweep method in the power system	Calculate voltage drop with fixed current	Calculate current with fixed voltage	Current can be negative	Fixed

The FBI method is similar to the forward-backward sweep method in the electric power system [69]. For better understanding, the comparison of the above two methods is presented in Table 2-4, in which the differences are caused by the difference equations in our power flow model. The backward step fixes temperature, where the resulting nonlinear hydraulic equations are solved by the Newton-Raphson method. The forward step fixes mass flow to linearize difference equation (2-13), gives correct pipe boundary conditions, and updates temperature mixing node dynamically according to the mass flow, which decides the form of temperature mixing equations.

2.4.5.1 Backward Step for Hydraulic Model

The Backward step is proposed for the hydraulic model considering multiple DERs, loops, and variable mass flow. In the Backward method, node exchanger supply and return temperatures ($T_{i,t}^{NS}$ and $T_{i,t}^{NR}$) are fixed; Thus, node mass flow $m_{i,t}^{n}$ can be calculated from (2-16). Then the problem is transferred to solve (2-6)-(2-8) and obtain pipe mass flow vector $\boldsymbol{m}_t$, where the Newton-Raphson method is applied [22]:

$$\left(\boldsymbol{m}_t\right)^{k+1}=\left(\boldsymbol{m}_t\right)^{k}-\left(\boldsymbol{J}_h^{-1}\Delta\boldsymbol{F}_h\right)^{k}, \tag{2-19}$$

where $\boldsymbol{J}_h$ is the Jacobian matrix in the hydraulic calculation, and $\Delta\boldsymbol{F}_h$ is the hydraulic mismatch vector in which

$$\boldsymbol{J}_h=\begin{bmatrix}\boldsymbol{A}_r\\ 2\boldsymbol{B}\boldsymbol{K}_t^{P}\left|\boldsymbol{m}_t\right|\end{bmatrix}, \tag{2-20}$$

$$\Delta\boldsymbol{F}_h=\begin{bmatrix}\boldsymbol{A}_r\boldsymbol{m}_t-\boldsymbol{m}_{r,t}^{n,r}\\ \boldsymbol{B}\boldsymbol{K}_t^{P}\boldsymbol{m}_t\left|\boldsymbol{m}_t\right|\end{bmatrix}, \tag{2-21}$$

where $\boldsymbol{m}_t^{n,r}$ is the reduced node mass flow vector which eliminates the mass flow of heat slack node, and $\boldsymbol{A}_r$ is the reduced node-branch matrix with the dimension of $(n_{node}-1)\times n_{pipe}$ after eliminating the heat slack node in the heating system. The dimension of $2\boldsymbol{B}\boldsymbol{K}_t^{P}\left|\boldsymbol{m}_t\right|$ is $n_{loop}\times n_{pipe}$, where n_{pipe}, n_{node}, and n_{loop} are the numbers of the pipelines, nodes, and loops in the heating system, respectively.

Additionally, if there is no loop in a heating system (the heating network is radial), the hydraulic model only has (2-6). Moreover, the backward step holds the same in the supply network and the return network of the heating system because of the mirror relationship.

2.4.5.2 Forward Step for Thermal Model

The forward step solves the thermal model with the nonlinear equations and difference equations, where the mass flow is fixed. After that, equation (2-13) becomes linear difference equations, and nonlinear equation (2-14) changes to the linear equation. Then the node and pipe temperatures can be calculated sequentially. Take the supply network for example, the processes are:

1) Reconstruct the heating network at time *t* by adjusting the defined direction of pipes whose mass flow is less than zero.
2) Decide the calculation order (layer) of pipelines:

$$L_i = \begin{cases} 1 & \text{if} \quad N_i^s \in H_G \\ k+1 & k = \max\{L_j \mid N_j^e = N_i^s\}, N_i^s \notin H_G \end{cases} \qquad i \in P_S \, , \tag{2-22}$$

   where L_i is the layer number of pipe *i*, which indicates the calculation sequence. N_i^s is the initial node of pipe *i*, and N_j^e is the ending node of pipe *j* in the reconstructed network. The first row of (2-22) indicates that $L_i = 1$ if the pipe *i* is connected to the heat source. The second row of (2-22) means that the layer number of pipe *i* is decided by the maximum layer number of its injecting pipe *j*, i.e. L_j, where $N_j^e = N_i^s$ indicates the relationship between pipe *i* and *j*.
3) In each layer, calculate the pipe end temperature using (2-13) and then calculate the node temperature based on (2-14) and (2-15). This step is implemented layer by layer.

For the return network in the heating system, step 1 and step 3 are the same, and the difference is to change H_G to H_L in step 2.

Remark 2-1**:** Step 1 enables pipes with the negative mass flow to have correct boundary conditions for (2-13). If no adjustment is made, when the mass flow $m_{i,t}$ of pipe *i* is less than zero at time *t*, the pipe initial temperature is not the correct boundary condition. If so, the calculation of pipe *i* will not have correct results.

Remark 2-2**:** Step 2 ensures when calculating a pipeline, the other pipelines which provide boundary conditions have been calculated.

After the Forward calculation, node temperatures, node exchanger temperatures, and the pipe temperatures are obtained. Then the results are sent to the next-time backward step to update node mass flow using (2-16). If the node mass flow difference of *k* and *k*+1 time iteration satisfies (2-23), the FBI converges with the power flow distribution of the heating system.

$$\max \left| \frac{\left(m_{i,t}^n\right)^{(k+1)} - \left(m_{i,t}^n\right)^{(k)}}{\left(m_{i,t}^n\right)^{(k)}} \right| \le \varepsilon_h \, , \tag{2-23}$$

where ε_h is the heating convergence criterion.

Additionally, the proposed FBI method can be applied in the heating system with different node types listed in Table 2-3. For example, we can change hT_r node in the heating system to $h\Delta T$ node, which indicates the given condition changes to the heat node power $h_{i,t}$ and the difference of node supply and return temperatures ΔT. After that, the backward step is the same because we can directly obtain the node mass flow with ΔT. The forward step has slight changes: the supply network is calculated first and then the return network is calculated based on the results of the supply network.

***Remark 2-3*:** The judgment (2-23) is the per-unit difference which can avoid the inaccuracy and inefficiency caused by directly using the real value of mismatch [15] and [27], especially when the mass flows of different nodes have large differences.

2.5 Convergence Analysis

To illustrate the computational stability of the proposed power flow model and solution method (called the proposed method in the following paragraphs), the calculation convergence is analyzed in this section compared with the existing steady-state method [15][63] because both methods are based on the fixed-point method.

In the hydraulic calculation i.e., backward step, the temperature is fixed to update the mass flow; In the thermal calculation i.e., forward step, the mass flow is fixed to calculate the temperature. The two calculation steps iterate until converge. Thus, the convergence condition for the above fixed-point iteration [70] is:

$$\left|\nabla f_m\right| \cdot \left|J_h\right| \leq 1, \tag{2-24}$$

where $\left|J_h\right|$ is the 1 norm of the Jacobian matrix of hydraulic calculation in (2-20), and $\left|\nabla f_m\right|$ is the 1 norm of the partial derivative of the temperature terms in (2-18) with respect to mass flow.

2.5.1 Mathematical Analysis for Simple Heating System

This section analyzes the convergence characteristics of the proposed method from the mathematical point of view. The heating system is shown in Figure 2-9, where node 1 is a heat source, and node 2 is a heat load. For this system, take the supply network for example,

$$\nabla f = \frac{\partial \boldsymbol{\tau}(x,t)}{\partial \boldsymbol{m}_t}, \tag{2-25}$$

where $\boldsymbol{\tau}(x,t)$ is the vector of pipe temperature distribution function $\tau_i^S(x,t)$.

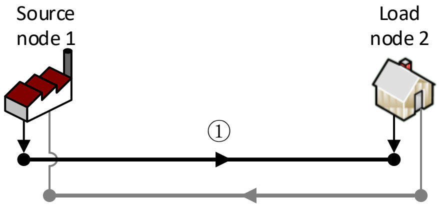

Figure 2-9. Test heating system for convergence analysis.

Assume that the length of pipe 1 is short enough:

$$0 < x_1 = \Delta x \cdot \tag{2-26}$$

In the supply network, the pipe end temperature of pipe 1 equals to the node temperature of node 2:

$$\tau_1^S(L_1, t) = T_{2,t}^S \cdot \tag{2-27}$$

Thus, temperatures of node 1 at time *t* and node 2 at time *t*-1 have little difference according to (2-13), which implies:

$$\left| T_{1,t}^S - T_{2,t\text{-}1}^S \right| < \delta_o , \tag{2-28}$$

where the δ_o is a small temperature difference and generally is less than 5°C because the Δt is not too large based on the equation (2-12) and the fact that the sharp change of temperature seldom happens in a real heating system [18]. The reduced node-branch matrix $\boldsymbol{A}_r$ of Figure 2-9 is:

$$\boldsymbol{A}_r = [1]_{1\times 1} \quad . \tag{2-29}$$

And the loop-branch matrix $\boldsymbol{B}$ does not exist because of the absence of loops. Thus, according to (2-20), the hydraulic Jacobian matrix for the topology in Figure 2-9 equals to 1, i.e., $J_h = [1]_{1\times 1}$.

For the proposed method, substitute (2-13) and (2-27) to (2-25):

$$\nabla f_{d,m} = \frac{\dfrac{T_{1,t}^S - T_{2,t\text{-}\Delta t}^S}{\Delta t \Delta x \rho A_1} + \dfrac{T_{1,t}^S - T_{1,t}^a}{\Delta x \rho^2 A_1^2 c_p R_1}}{\left(\dfrac{1}{\Delta t} + \dfrac{m_{1,t}}{\Delta x \rho A_1} + \dfrac{1}{\rho c_p A_1 R_1} \right)^2} , \tag{2-30}$$

where $\nabla f_{d,m}$ is the 1 norm of the partial derivative of the supply temperature at time *t* with respect to mass flow in the proposed power flow model.

For the steady-state method in [15] and [63], the pipeline model (2-13) is replaced by the simplified pipe conductive equation without heat dynamic process:

$$\tau_1^S(x,t) = (T_{1,t}^S - T_{1,t}^a)e^{-\frac{R_1 x_1}{c_p m_{1,t}}} + T_{1,t}^a. \tag{2-31}$$

Substitute (2-31) into (2-25)

$$\nabla f_{s.m} = (T_{1,t}^S - T_{1,t}^a)e^{-\frac{R_1 L}{c_p m_{1,t}}}\left(\frac{R_1 x_1}{c_p}\right)\frac{1}{\left(m_{1,t}\right)^2}, \tag{2-32}$$

where $\nabla f_{s.m}$ is the 1 norm of the partial derivative of the supply temperature of node 2 at time *t* with respect to mass flow in the steady-state method.

In the proposed method and the steady-state method, the hydraulic models are the same, and the Jacobian matrix is

$$J_{d,h} = J_{s,h} = J_h = \left[1\right]_{1\times 1}, \tag{2-33}$$

where $J_{d,h}$ and $J_{s,h}$ are hydraulic Jacobian matrices of the proposed method and the steady-state method, respectively.

According to [18], choose $\Delta t = 15\,\mathrm{min}$, $\Delta x = 5\mathrm{m}$, and $A_1 = 0.1\mathrm{m}$ which satisfy the constraint (2-12). After that:

$$\nabla f_{d.m} = \frac{\dfrac{T_{1,t}^N - T_{2,t\text{-}\Delta t}^N}{2335} + \dfrac{T_{1,t}^N - T_{1,t}^a}{2070516}}{\left(\dfrac{1}{15} + \dfrac{m_{1,t}}{157} + \dfrac{1}{13188}\right)^2} < \frac{\dfrac{\delta_o}{2335}}{\left(\dfrac{1}{15}\right)^2} << 1, \tag{2-34a}$$

$$\nabla f_{s,m} = \frac{1}{46.67\left(m_{1,t}\right)^2}. \tag{2-34b}$$

Equation (2-34) indicates for the proposed model, even when the pipe mass flow is zero, $\left|\nabla f_{d.m}\right|\left|J_{d,h}\right|$ is much less than 1, which means that the proposed method is robust. But for the steady-state model, while the pipe mass flow $m_{i,t}$ is less than 0.416 kg/s, the $\left|\nabla f_{s.m}\right|\left|J_{s,h}\right|$ will be larger than 1, which cannot guarantee the convergence. Therefore, under the given conditions, the steady-state method has convergence problems when mass flow is slow, but the proposed method is robust even when the mass flow is zero.

2.5.2 Numerical Tests for Complex Heating System

2.5.2.1 Test System and Results

This section aims to extend the convergence analysis from the simple heating system to the complex heating system using numerical tests. The analysis is based on a real heating system situated in Barry Island, South Wales [72] with 3 DERs and a loop in the heating system, which is shown in Figure 2-10.

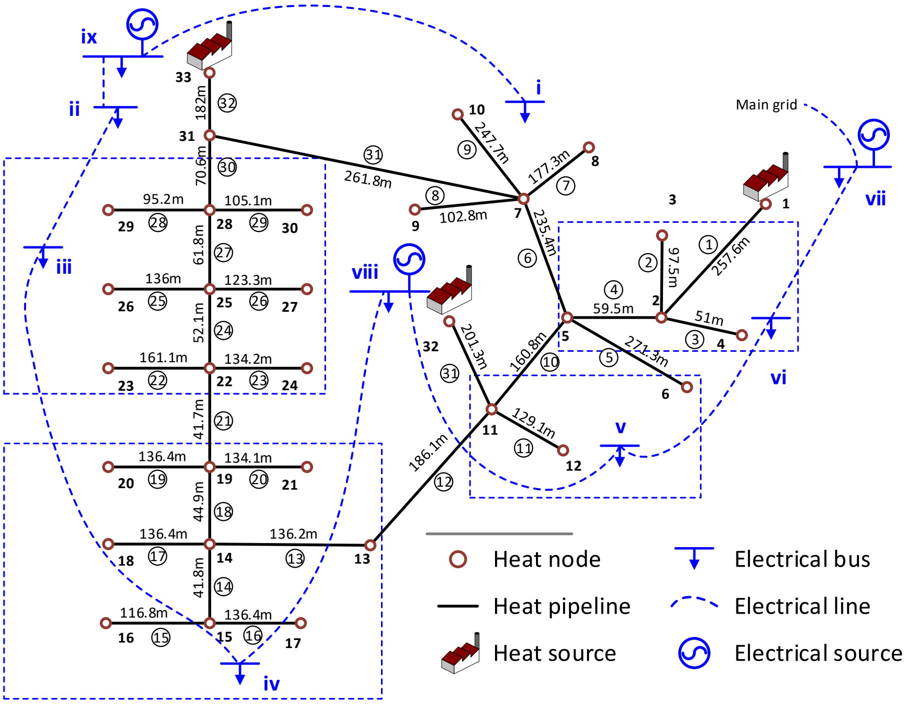

Figure 2-10. The combined heat and power system in Barry Island.

Figures 2-11 and 2-12 present the results of the proposed method and the steady-state method, including the node mass flow and the per-unit difference between two Forward-Backward iterations. The stopping criterion ε_h is 10^{-4} in (2-23).

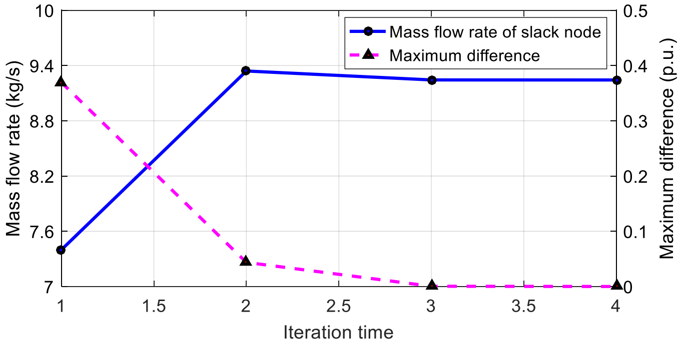

Figure 2-11. Mass flow of heat slack node 33 and maximum difference between two iterations of the proposed model.

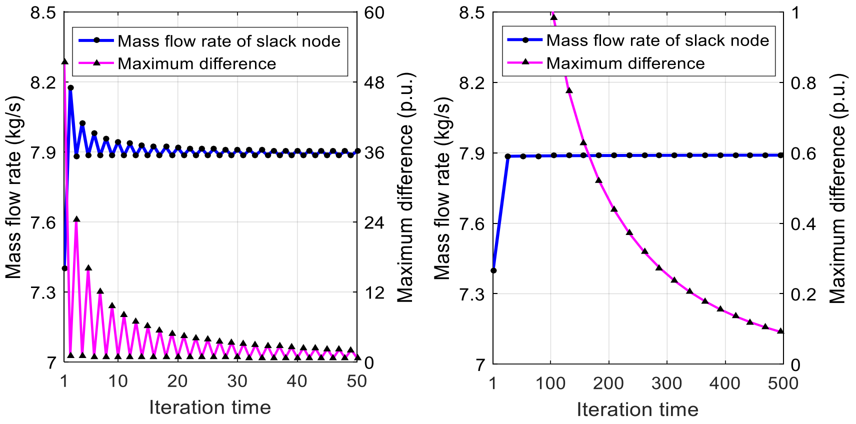

(a) (b)

Figure 2-12. Mass flow of heat slack node 33 and maximum difference between two iterations of steady-state method after (a) 20 iterations and (b) 500 iterations.

2.5.2.2 Discussion of Results

It can be observed from Figure 2-11 that the proposed method converges after 4 iterations, but the steady-state method does not converge after 20 iterations and has large differences. Even after 500 times, the steady-state method does not converge. To explain the reason for the above phenomenon, the explanations of the two methods are presented in Figure 2-13, where *n* and n_{max} are iteration time and maximum iteration time here, respectively. For better understanding, the physical illustrations of the pipe temperature models of the proposed method and steady-state method are compared in Figure 2-14.

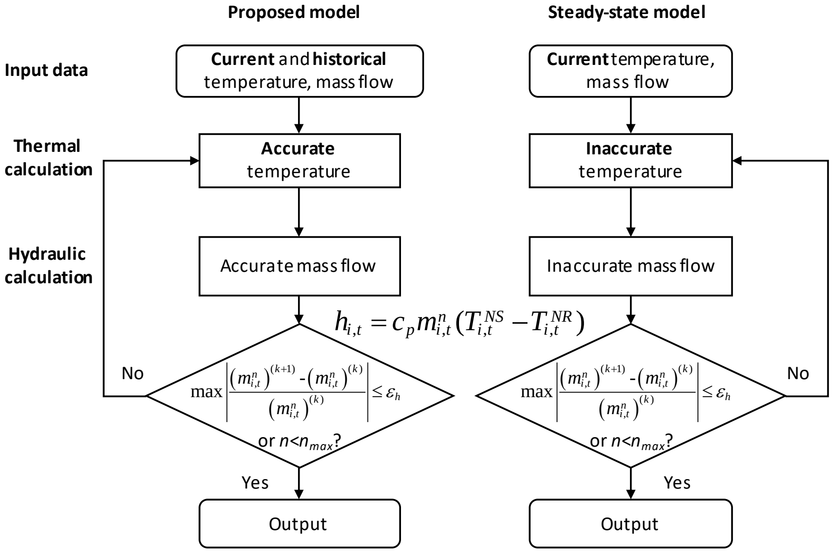

Figure 2-13. The illustration of the calculating process in the proposed method and steady-state method

In Figure 2-14 (a), the proposed method uses both current state and historical state i.e., pipe historical temperature distribution, to calculate current temperature results. Thus, the temperature results are accurate in the proposed thermal calculation (Forward step) because physically the thermal system is in the dynamic process under given Δt. Then in the iteration process, it provides the hydraulic calculation (Backward step) with an accurate iteration point. As a result, the calculation of the heating system can converge to a result quickly and accurately in the proposed method.

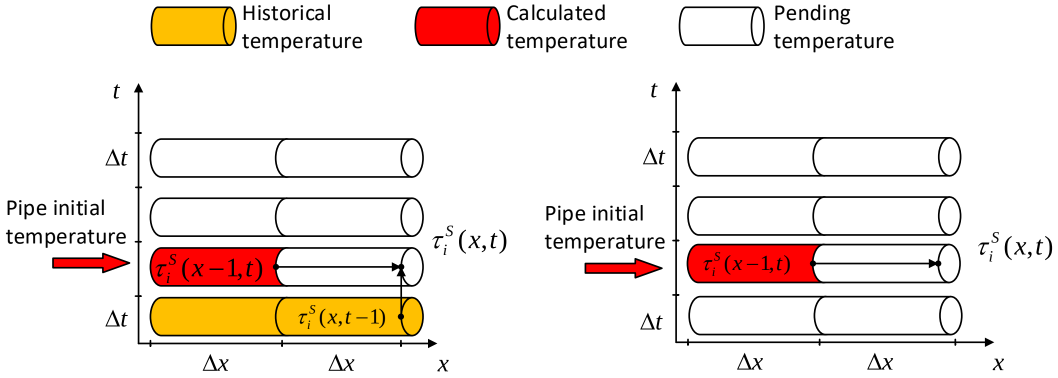

(a) (b)

Figure 2-14. The comparison of pipe temperature calculation in (a) proposed method and (b) steady-state method.

However, the steady-state method in (2-31) presented by Figure 2-14 (b) neglects the influence from historical temperature and only uses the current state to calculate current temperature results, which ignores the thermal dynamic process. Therefore, the temperature results of the steady-state method are not accurate, and then the inaccuracy is transmitted to the hydraulic calculation of mass flow by the fixed-point method (2-16). As a result, in the steady-state method, the “chain of inaccuracy” may lead to the non-convergence of the heat power flow calculation.

To validate the computational stability of the proposed method from another angle, different scales of the heating systems are tested from a 5-node system to a 119-node system. As shown in Figure 2-15, the maximum mass flow differences of all nodes between two iterations are all less than the given convergence difference $\varepsilon_h = 10^{-3}$, which indicates the proposed method can converge under the heating system with different complexities. Furthermore, the average difference is below 2.2×10^{-4} p.u., demonstrating the efficiency and the accuracy of the proposed method.

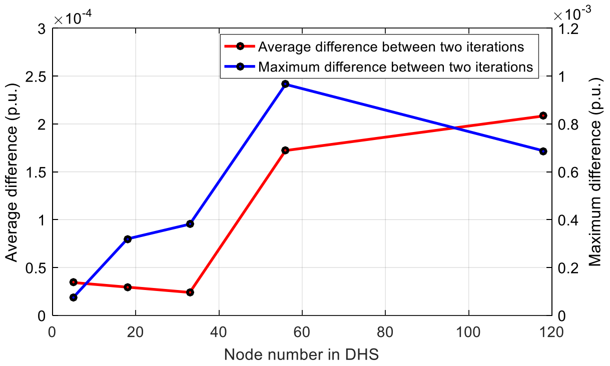

Figure 2-15. The maximum difference and average difference between two iterations in different power flow methods

In brief, the proposed method improves the convergence performance and accuracy by using the accurate heat pipeline model considering the heat dynamic process.

***Remark 2-4*:** Limited to direction-variable mass flow, the strict boundary condition of pipe temperature calculation in (2-13), and the coupling of algebraic equations and difference equations, the function of the heating system cannot be expressed analytically and use (2-24) or other methods such as Laplace transformation to analyze.

2.6 Case Study

Based on the data from the real world, the method in literature, and the result of commercial software, the case studies are carried out to validate the proposed method.

2.6.1 Case 1: Validation Using Real-World Data

To verify the proposed heating system model, the calculated data of the proposed method are compared with the measured data of a real heating system in Figure 2-16 located in the suburb of Shijiazhuang, China [21]. The hot water is transported from the Luhua CHP unit to the heat exchanger station through the 9.25 km pipeline, where the supply temperature of the Luhua CHP unit and mass flow are time-varying.

The validation applies the measured supply temperature at Luhua CHP unit and the mass flow to calculate the temperature at the heat exchanger station using the proposed method, which is compared with the measured temperature at the heat exchanger station from 0:00 to 24:00 on Dec 15th, 2015 [21].

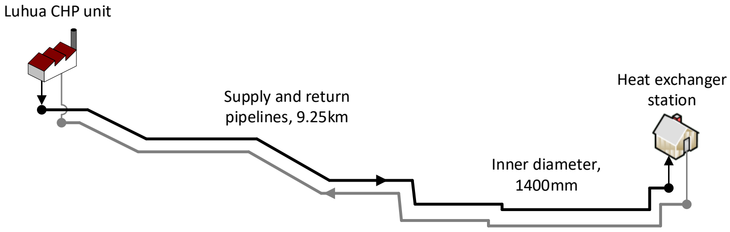

Figure 2-16. Topology of the heating in Shijiazhuang, China.

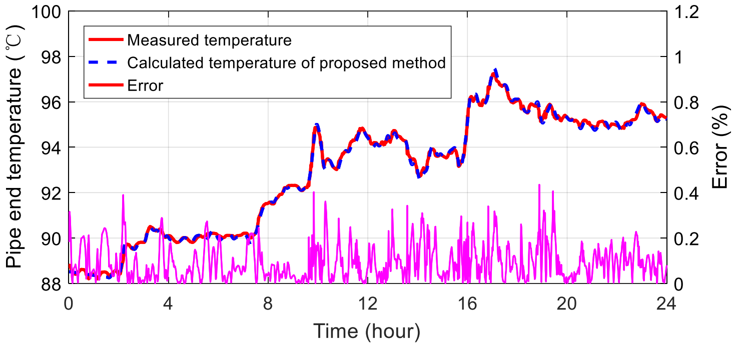

Figure 2-17. The calculated pipe end temperature and the error of the proposed model and measured data.

Figure 2-17 presents the results of the calculated temperature of the heat exchanger station and the error between the proposed model and the measured data, which demonstrates that the proposed method has high accuracy with an average error of 0.09% (0.0864℃) and the maximum error of 0.44% (0.4148℃) compared with the measured data. Considering the structure and devices of the real heating system, the error may come from the temperature sensor at the heat exchanger station and the inaccurate estimation of the pipe parameter and the environmental temperature.

2.6.2 Case 2: Dynamic Performance in Test Heating System

Case 2 is designed to validate the proposed method in the dynamic process based on the results from the commercial software *Bentley sisHYD*. As shown in Figure 2-18, the test heating system has a loop with two DER.

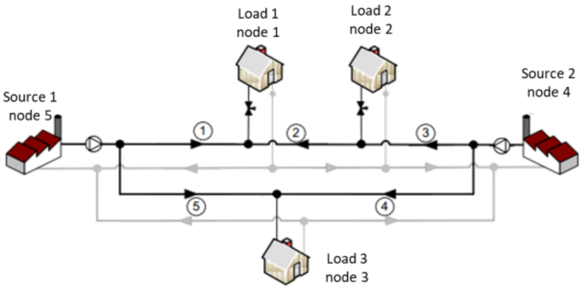

Figure 2-18. Topology of the test heating system in Case 2.

In Figure 2-18, the circled numbers are numbers of pipes, and the node numbers are below the names of sources and loads. The nodes 4 and 5 are heat sources, where node 5 is a heat slack node, while the node 4 is a hT^{NS} node. Under the same conditions, the pipe temperature results of the two methods are shown from Figure 2-19 (a) to (e).

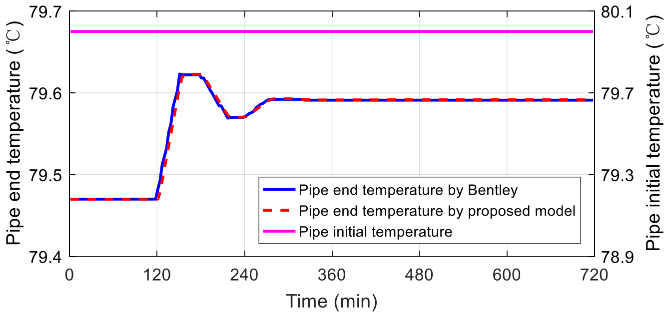

Figure 2-19 (a)**.** Pipe initial temperature and end temperature of pipe 1.

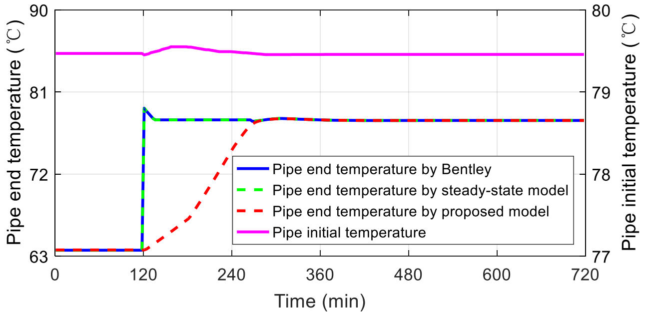

Figure 2-19 (b)**.** Pipe initial temperature and end temperature of pipe 2.

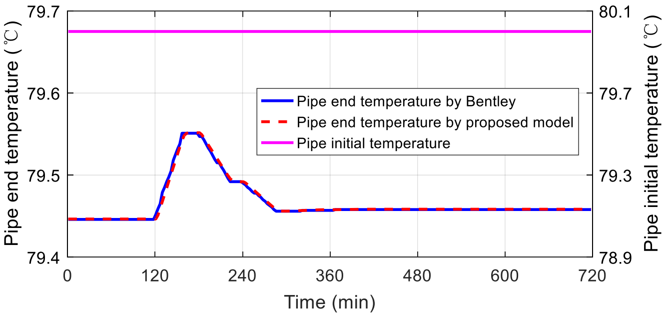

Figure 2-19 (c)**.** Pipe initial temperature and end temperature of pipe 3.

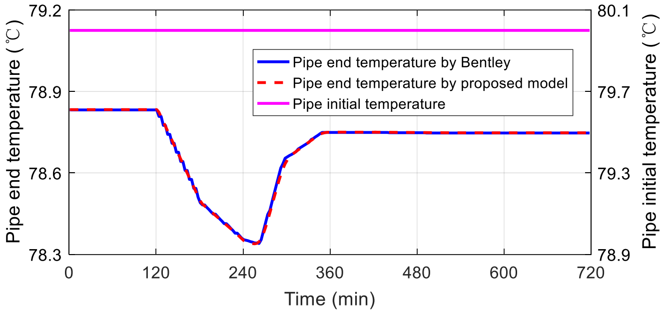

Figure 2-19 (d)**.** Pipe initial temperature and end temperature of pipe 4.

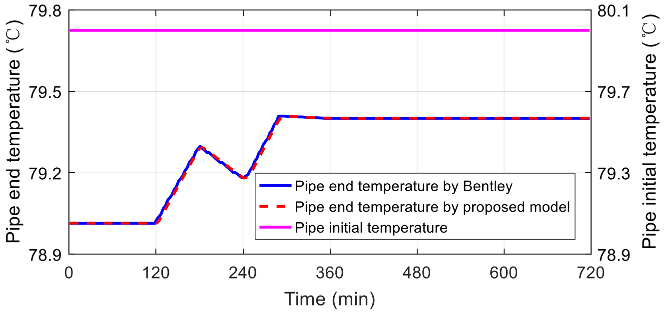

Figure 2-19 (e)**.** Pipe initial temperature and end temperature of pipe 5.

From the temperature results in Figure 2-19, except for the pipe 2, the proposed method and the *Bentley sisHYD* have the same pipe temperature results because these pipes are connected to heat sources with the same boundary conditions. However, from 120 minutes to 250 minutes at pipe 2, the result of *Bentley sisHYD* has a sharp temperature increase with no time delays and temperature dynamics, failing to reflect the heat dynamic process. To explore the reason for this failure, the pipe end temperature calculated by the steady-state method [63] is presented using a green dotted line in Figure 18 (b). Obviously, the commercial heat dynamic calculation software *Bentley sisHYD* has the same results as the steady-state model which ignores the heat dynamic process. One possible explanation is that the *Bentley sisHYD* cannot decide the accurate boundary condition of the pipe 2 while the mass flow is variable in the heating system with loops. Under this circumstance, the *Bentley sisHYD* compromises to apply steady-state results for pipe 2. Yet the proposed method can attain correct boundary conditions and reflect temperature change accurately for pipe 2 in the dynamic process.

In brief, under given conditions, the proposed method is valid and has better dynamic performance compared with the commercial software *Bentley sisHYD.*

2.6.3 Case 3: Steady-state Process in Barry Island

The aim of Case 3 is to validate the proposed method of combined heat and power systems in the steady-state process, which indicates the loads and sources have no adjustment or change. This case is based on the topology of Barry Island in Figure 2-10 which has a 9-node electric power system and a 33-node heating system with the meshed heating network and 3 DERs.

To verify the accuracy, the proposed method is compared with the steady-state power flow method [15] under the same topology and data. The electric and heat power flows are both analyzed, and the bus voltage in the electric power system and node supply temperature in the heating system are drawn in Figure 2-20 and 2-21, respectively.

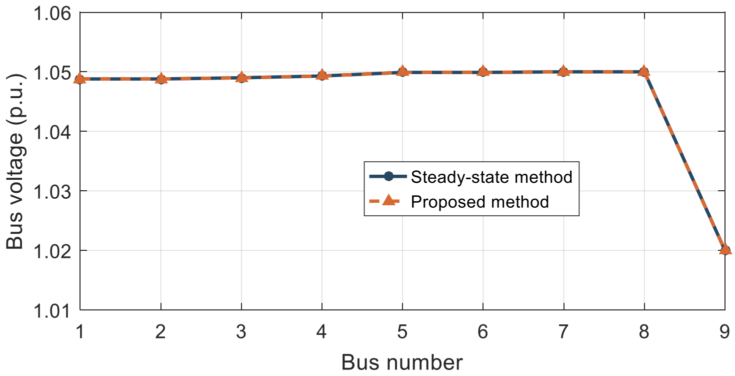

Figure 2-20. Bus voltage of proposed method and steady-state method in steady-state process.

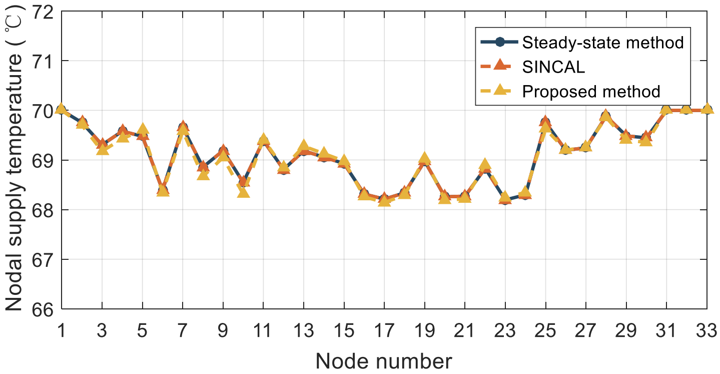

Figure 2-21. Node supply temperature of proposed method, steady-state method and SINCAL in steady-state process.

Figure 2-20 shows that the bus voltages of the proposed method and the steady-state method are the same with no error because of applying the same electric power system model under the same conditions. Moreover, in Figure 2-21 for the heating system, the comparison of two models and another commercial software SINCAL holds same results even though the heating system models are different, where the average errors of the proposed method are 0.0998% and 0.0997% compared with the steady-state method and SINCAL, respectively. To explain the reason of this same result, the steady-state pipeline model and the proposed pipeline model are compared under the steady-state process.

The steady-state pipeline model (2-31) is the simplification of the dynamic thermal model (2-10) by neglecting the partial derivative of time *t* i.e. ignoring the heat dynamic process. But in the steady-state process simulated in this case, the pipe temperature $\tau_i^S(x,t)$ and $\tau_i^R(x,t)$ have already reached a steady state, indicating:

$$\tau_i^S(x,t)=\tau_i^S(x),$$

$$\tau_i^R(x,t)=\tau_i^R(x).$$

Thus, the partial derivative of time *t* at (2-10) equals to zero exactly:

$$\frac{\partial\tau_i^S(x,t)}{\partial t}=\frac{\partial\tau_i^S(x)}{\partial t}=0, \tag{2-35a}$$

$$\frac{\partial\tau_i^R(x,t)}{\partial t}=\frac{\partial\tau_i^R(x)}{\partial t}=0. \tag{2-35b}$$

Therefore, take (2-35) into (2-10) can we obtain (2-36), which can directly derive the steady-state pipeline model (2-31) [15]. As a result, under the steady-state process, because the heat variable is not time-varying, the results of the proposed method in this chapter equal to the steady-state model (2-31).

$$m_{i,t} \cdot c_p \frac{d\tau_i^S(x)}{dx} = \frac{T_{i,t}^a - \tau_i^S(x)}{R_i}, \tag{2-36a}$$

$$m_{i,t} \cdot c_p \frac{d\tau_i^R(x)}{dx} = \frac{T_{i,t}^a - \tau_i^R(x)}{R_i}. \tag{2-36b}$$

2.6.4 Case 4: Dynamic Process in Barry Island

Based on the combined heat and power system in Figure 2-10, Case 4 simulates the electric and heat power flow under the dynamic process, which indicates there are time-varying changes in the electric power system and the heating system. Because the electric power system models in the existing steady-state method and the proposed method are the same and the difference of two models originates from the heating system model, the bus voltage is omitted, and the node supply temperature is shown in Figure 2-22 for example.

It can be observed that in the dynamic process, as shown in Figure 2-22, the two models have three main differences: time delay, temperature dynamics, and convergence. Firstly, the light blue circle indicates the steady-state method fails to track time delays because of ignoring the dynamic heat transmission process. Secondly, circled by the red circle, the steady-state method does not converge at 4:45, 5:00, 20:30, and 21:00 because the steady-state thermal method transmits the inaccurate iteration point to hydraulic calculation, which leads to the non-converge of the fixed-point iteration. Finally, as circled in the deep blue color, the steady-state method has unreasonable sharp temperature fluctuations as a result of ignoring heat dynamic process, failing to illustrate real temperature dynamics.

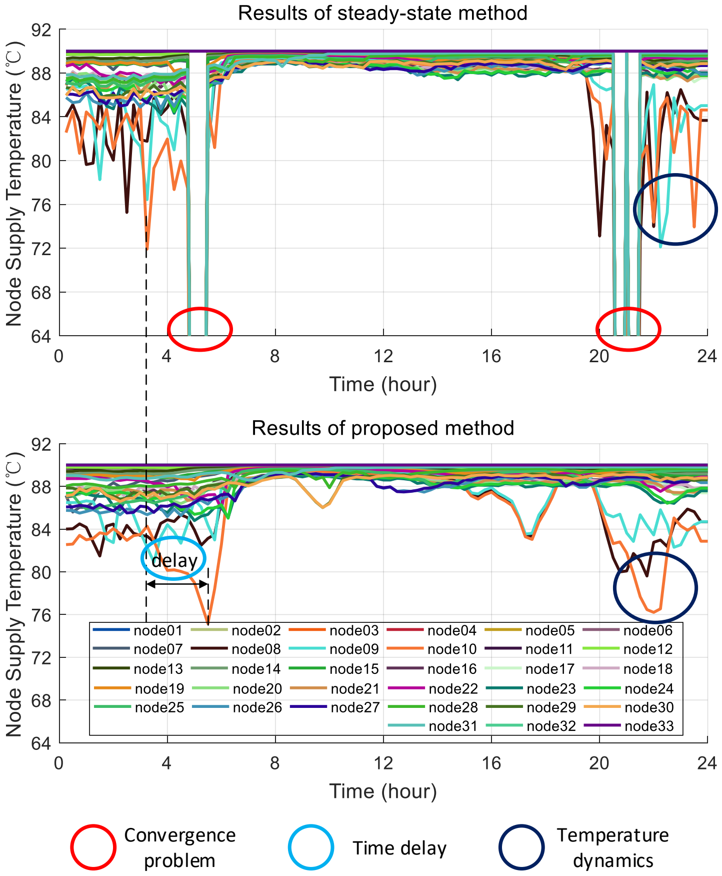

Figure 2-22. Node supply temperature of proposed method and steady-state method in dynamic process.

Based on the energy system of Barry Island, the proposed method has better characteristics in terms of convergence and reflecting heat dynamic process which is ignored by the steady-state method. Besides, the proposed method has high efficiency with the calculation time of 134.4 seconds for 96 time sections.

2.7 Conclusion

A generalized power flow model is proposed for combined heat and power systems considering heat dynamic process, loops, multiple DERs, and variable mass flow simultaneously, which makes it widely applicable in solving real-world power flow problem. To overcome the difficulty of calculating complexity, the HE-FBI method is developed to decompose the model equations into small parts and solve them sequentially and iteratively based on the physical nature of combined heat and power systems. Mathematical and numerical convergence studies demonstrate that the proposed method improves convergence characteristics by providing the fixed-point method with accurate iteration points compared with the steady-state method. In case studies, the proposed method has high accuracy compared with the measured data, which outperforms both the commercial software and the steady-state method. Moreover, it has also been proved by case studies that the heat dynamic process can be reflected, and better convergence can be guaranteed by the proposed model and HE-FBI method, which indicates the effectiveness and necessity of the research.

Based on the proposed power flow model, the next two chapters, i.e., the Chapter 3 and 4 will develop the economic dispatch problem of combined heat and power systems considering the flexibility from the heating system.

Chapter 3: Synchronous Economic Dispatch with Variable Mass Flow

3.1 Overview

In the synchronous economic dispatch of combined heat and power systems, the temperature and mass flow are the two most important types of control variables in heating systems [30][31]. However, if the mass flow is variable, the existing research models the economic dispatch problem as an MINLP with integers and bilinear constraints. To deduce the complexity, many research papers fix mass flow and only consider varying temperature adjustment, which limits the flexibility of combined heat and power systems [32]. To further increase the adjustable range of heat power and improve the flexibility of electric power adjustment, this chapter studies how to adjust both mass flow and temperature in synchronous dispatch.

On the synchronous economic dispatch, the electric power system and the heating system have the same adjustment time scale. Based on this framework, the dispatch model and the solution method for the combined heat and power system are proposed, and the contributions of this chapter are:

1) A non-convex economic dispatch model is developed, which removes integers in existing models without compromising on the accuracy considering the flexibility from adjusting mass flow and the integration of DERs in the electric power system and the heating system.
2) An efficient solution method is proposed for the non-convex optimization model with acceleration and convergence based on the framework of GBD, which is faster than the original GBD and overcomes the simplifications on the optimization models and solution methods.

3.2 Optimization Model

Based on the physical model of combined heat and power systems in Figure 2-1, the optimization model of the synchronous dispatch is developed in this section.

3.2.1 Objective Function

The objective function is to minimize the total generation cost of all energy sources at all time sections:

$$\min_{p_{i,t},h_{i,t}} f = \min \sum_{i \in G} \sum_{t=1}^{T} C_{i,t}(p_{i,t}, h_{i,t}) , \tag{3-1}$$

where $C_{i,t}$ is the cost function of energy source *i* (including electric-heat coupling devices) at time *t*, which is expressed using a quadratic function of electricity and heat productions [27]:

$$C_{i,t} = \eta_{i,t,0} + \eta_{i,t,1} p_{i,t} + \eta_{i,t,2} p_{i,t}^2 + \eta_{i,t,3} h_{i,t} + \eta_{i,t,4} h_{i,t}^2 + \eta_{i,t,5} p_{i,t} h_{i,t} ,$$

where $\eta_{i,t,0}$ - $\eta_{i,t,5}$ are time-varying cost coefficients of source *i* at time *t*, which are given by generation costs and time-of-use. For example, for thermal generators which only generate electricity, coefficients of heat-related terms are zero. For electric boilers, electricity-related coefficients are negative and heat-related coefficients are positive.

3.2.2 Electric Power System Constraints

In the economic dispatch, the DC power flow model is adopted in the electric power system. The real-time electric power balance is required between the generation side and the load side:

$$\sum_{i \in E} p_{i,t} = \sum_{i \in E} d_{i,t} \quad \forall t = 1, 2, \cdots T , \tag{3-2}$$

where $d_{i,t}$ is the load active power of bus *i* at time *t*.

The electric power $l_{i,t}$ of line *i* at time *t* is calculated by

$$l_{i,t} = \sum_{j \in E} SF_{i,j} \cdot (p_{j,t} - d_{j,t}) \quad \forall i \in L,\ t = 1, 2, \cdots T , \tag{3-3}$$

where $SF_{i,j}$ indicates the shift factor of bus *j* to line *i*. Set *L* is the set of electric lines.

The line power flow should be below its thermal limitation:

$$\underline{l}_{i,t} \le \sum_{j \in E} SF_{i,j} \cdot (p_{j,t} - d_{j,t}) \le \overline{l}_{i,t} \quad \forall i \in L,\ t = 1, 2, \cdots T , \tag{3-4}$$

where $\underline{l}_{i,t}$ and $\overline{l}_{i,t}$ are the lower and upper limits of the electric power of line *i* at time *t*.

3.2.3 Heating System Constraints

In heat systems, it is assumed that 1) the heat supply network and the heat return network are radial, respectively, and 2) the direction of mass flow is the same as the given reference direction. These assumptions hold in most practical heating systems and are widely adopted in the literature of economic dispatch [27][38][39].

3.2.3.1 Heat Pipeline Constraints

The node temperature mixing equations are applied to calculate node temperature from its injecting pipe end temperature:

$$\begin{gathered}\left(m^{n}_{i\in H_G,t}+\sum_{j} m_{j,t}\right)T^{S}_{i,t}=\left(m_{i\in H_G,t}T^{NS}_{i\in H_G,t}\right)+\left(\sum_{j} m_{j,t}\tau^{SE}_{j,t}\right),\\ \forall i\in H,\ j\in P_S\cap In(i),\ t=1,\ 2,\ \cdots T\end{gathered}\tag{3-5a}$$

$$\begin{gathered}\left(m^{n}_{i\in H_L,t}+\sum_{j} m_{j,t}\right)T^{R}_{i,t}=\left(m^{n}_{i\in H_L,t}T^{NR}_{i\in H_L,t}\right)+\left(\sum_{j} m_{j,t}\tau^{RE}_{j,t}\right).\\ \forall i\in H,\ j\in P_R\cap In(i),\ t=1,\ 2,\ \cdots T\end{gathered}\tag{3-5b}$$

The pipe initial temperature equals to the temperature of its connecting node:

$$\tau^{SI}_{j,t}=T^{S}_{i,t}\quad j\in P_S\cap Lv(i),\ i\in H,\ t=1,\ 2,\ \cdots T\ ,\tag{3-6a}$$

$$\tau^{RI}_{j,t}=T^{R}_{i,t}\quad j\in P_R\cap Lv(i),\ i\in H,\ t=1,\ 2,\ \cdots T\ .\tag{3-6b}$$

In existing research like [27] and [39], the heat pipeline models with variable mass flow use integers to reflect time delays of the heat dynamic process, which makes the optimization problem hard to solve. In this paper, the pipe temperature segment model from (2-13) is adopted in (3-7) to describe the heat dynamic process using a series of time-related and space-related nonlinear equations. As a result, the complexity caused by integers is reduced without compromising on accuracy [10][18].

$$\begin{gathered}\left(a_i\, m_{i,t}+b_i\right)\tau^{S}_{i}(j,t)=c_i\,\tau^{S}_{i}(j,t-1)+\left(b_i\, m_{i,t}\right)\tau^{S}_{i}(j-1,t)+e_i\\ \forall i\in P_S,\ t=1,\ 2,\ \cdots T,\ j=1,2,\cdots S_i,\end{gathered}\ ,\tag{3-7a}$$

$$\begin{gathered}\left(a_i\, m_{i,t}+b_i\right)\tau^{R}_{i}(j,t)=c_i\,\tau^{R}_{i}(j,t-1)+\left(b_i\, m_{i,t}\right)\tau^{R}_{i}(j-1,t)+e_i\\ \forall i\in P_R,\ t=1,\ 2,\ \cdots T,\ j=1,2,\cdots S_i,\end{gathered}\ ,\tag{3-7b}$$

where scalars a_i-d_i are coefficients related to the characteristics of pipe i, which can be calculated by:

$$a_i=\frac{1}{\Delta t}+\frac{1}{\rho c_p A_i R_i}\ ,\quad b_i=\frac{1}{\Delta x\rho A_i}\ ,\quad c_i=\frac{1}{\Delta t}\ ,\quad d_i=\frac{T^{a}_{i,t}}{\rho c_p A_i R_i}\ .$$

Also, there are supplemental constraints including $\tau^{S}_{i}(0,t)=\tau^{SI}_{i,t}$, $\tau^{S}_{i}(S_i,t)=\tau^{SE}_{i,t}$ in the heat supply network and $\tau_i^R(0,t)=\tau_{i,t}^{RI}$, $\tau_i^R(S_i,t)=\tau_{i,t}^{RE}$ in the heat return network.

4.2.3.2 Heat Node Constraints

The node mass flow should satisfy hydraulic Kirchhoff's law: the difference of pipe mass flows injecting into a node and leaving from the node equals to the node consumed mass flow:

$$\boldsymbol{A}\boldsymbol{m}_t=\boldsymbol{m}_t^n \quad t=1,2,\cdots T. \tag{3-8}$$

The heat nodes exchange heat power with the heat supply and return networks through heat exchangers:

$$h_{i,t}=c_p m_{i,t}^n(T_{i,t}^{NS}-T_{i,t}^{NR}) \quad \forall i\in H,\ t=1,2,\cdots T. \tag{3-9}$$

In the heat supply network, for load nodes $T_{i,t}^{NS}=T_{i,t}^{S}$, and for source nodes $T_{i,t}^{S}$ is calculated by (3-5a). Similarly, in the heat return network, for load nodes $T_{i,t}^{R}$ is calculated by (3-5b), and for source nodes $T_{i,t}^{NR}=T_{i,t}^{R}$.

To ensure the reliable operation of node heat exchangers, node mass flow should not exceed the limit:

$$\underline{m}_{i,t}^n\le m_{i,t}^n\le \bar{m}_{i,t}^n \quad \forall i\in H,\ t=1,2,\cdots T, \tag{3-10}$$

where $\underline{m}_{i,t}^n$ and $\bar{m}_{i,t}^n$ are the lower and upper limits of the node mass flow of node *i* at time *t*. The pipe mass flow $m_{i,t}^n$ should satisfy:

$$\underline{m}_{i,t}\le m_{i,t}\le \bar{m}_{i,t} \quad \forall i\in P_S\cup P_R,\ t=1,2,\cdots T, \tag{3-11}$$

$$m_{i,t}\ge 0 \quad \forall i\in P_S\cup P_R,\ t=1,2,\cdots T, \tag{3-12}$$

where $\underline{m}_{i,t}$ and $\bar{m}_{i,t}$ are the lower and upper limits of pipe mass flow of pipe *i* at time *t* calculated by (3-8) and (3-10) considering the pipe pressure limits. The (3-12) guarantees the pipe mass flow is the same as the given direction when multiple DERs integrated.

To prevent the exhaustion of the heat pipeline storage, the total generated heat is required to be no less than the total heat load within scheduling periods:

$$\sum_{t=1}^{T}\left(\sum_{i\in H_G}h_{i,t}-\sum_{i\in H_L}h_{i,t}\right)\Delta t\ge 0. \tag{3-13}$$

The node exchanger supply and return temperature should satisfy the security limits:

$$\underline{T}_{i,t}^{NS} \le T_{i,t}^{NS} \le \overline{T}_{i,t}^{NS} \quad \forall i \in H,\ t=1,\,2,\,\cdots T\,, \tag{3-14a}$$

$$\underline{T}_{i,t}^{NR} \le T_{i,t}^{NR} \le \overline{T}_{i,t}^{NR} \quad \forall i \in H,\ t=1,\,2,\,\cdots T\,. \tag{3-14b}$$

where the $\underline{T}_{i,t}^{NS}$ and $\overline{T}_{i,t}^{NS}$ are the lower and upper limits of exchanger supply temperature at node *i*, respectively. Scalars $\underline{T}_{i,t}^{NR}$ and $\overline{T}_{i,t}^{NR}$ are the lower and upper limits of exchanger return temperature at node *i*, respectively.

3.2.4 Energy Sources Constraints

The feasible regions of energy sources are described by polytopes [36][67].

$$B_{k,i}\,p_{i,t} + K_{k,i}h_{i,t} \le v_{k,i} \quad \forall i \in G,\ t=1,\,2,\,\cdots T\,. \tag{3-15}$$

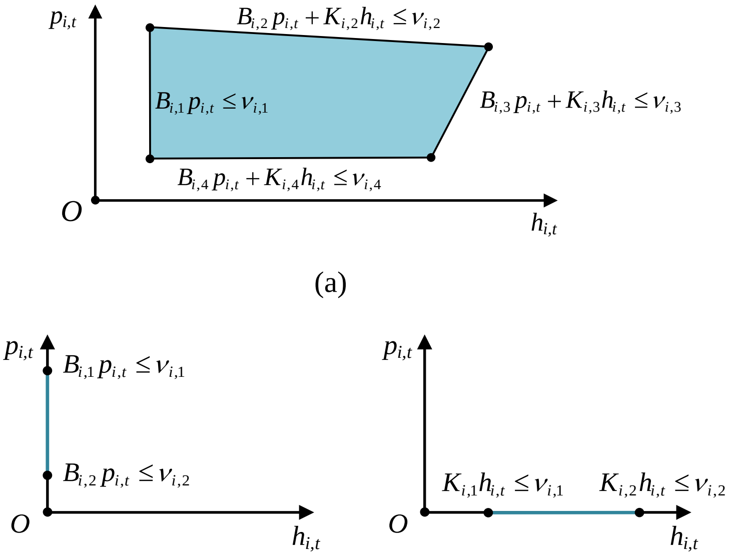

(a)

(b) (c)

Figure 3-1. The feasible regions of (a) CHP units, (b) thermal generators, and (c) natural gas boilers.

For example,

1) As shown in Figure 3-1 (a), if a source generates electricity and heat simultaneously such as a CHP unit, its polytope is in the first quadrant, where $p_{i,t} \ge 0$ and $h_{i,t} \ge 0$. Similarly, the polytope of an electric boiler resembles that of the CHP unit, but it is in the fourth quadrant.
2) As shown in Figure 3-1 (b), if a source only generates electricity such as a thermal generator, the coefficient $K_{k,i}$ related to heat power output is zero, where $p_{i,t} \ge 0$ and $h_{i,t} = 0$.

3) As shown in Figure 3-1 (c), if a source only generates heat such as a natural gas boiler, the coefficient $B_{k,i}$ related to electric power output is zero, where $p_{i,t}=0$ and $h_{i,t}\geq 0$.

The ramping constraint indicates the increment or decrement of the source power outputs within a single period should not exceed the ramping capacity:

$$D_{e,i}\cdot\Delta t\leq p_{i,t}-p_{i,t-1}\leq U_{e,i}\cdot\Delta t \quad \forall i\in G,\ t=1,\ 2,\ \cdots T, \tag{3-16a}$$

$$D_{h,i}\cdot\Delta t\leq h_{i,t}-h_{i,t-1}\leq U_{h,i}\cdot\Delta t \quad \forall i\in G,\ t=1,\ 2,\ \cdots T, \tag{3-16b}$$

where $D_{e,i}$ and $U_{e,i}$ are the downward and upward electric ramping capacities of source *i*, respectively. Scalars $D_{h,i}$ and $U_{h,i}$ are the downward and upward heat ramping capacities of source *i*.

Moreover, the CHP unit's supply temperature satisfies:

$$T_{j,t}^{NS}=T_{i,t}^{Set} \quad \forall i\in G,\ j=\mathit{\Gamma}_G(i),\ t=1,\ 2,\ \cdots T. \tag{3-17}$$

where $T_{i,t}^{Set}$ indicates the set temperature of energy source *i* at time *t*.

3.2.5 Model Generalization

To summarize the objective function (3-1) and constraints (3-2)-(3-17) in a succinct way, hereafter let $\boldsymbol{m}=\left[\boldsymbol{m}_t\right]$ be the vector of pipe mass flow, in which the dimension of $\boldsymbol{m}$ is $\left(n_{pipe}\cdot T\right)\times 1$. Then let $\boldsymbol{x}=[\boldsymbol{p},\boldsymbol{h},\boldsymbol{l},\boldsymbol{T}^{NS},\boldsymbol{T}^{NR},\boldsymbol{T}^{S},\boldsymbol{T}^{R},\boldsymbol{\tau}^{SI},\boldsymbol{\tau}^{SE},\boldsymbol{\tau}^{RI},$ $\boldsymbol{\tau}^{RE},\boldsymbol{\tau}^{S},\boldsymbol{\tau}^{R}\big]$ denote the vector of other decision variables. Next, use the pipe mass flow vector $\boldsymbol{m}_t$ to eliminate node mass flow vector $\boldsymbol{m}_t^n$ according to (3-11). Therefore, the optimization problem of the economic dispatch for combined heat and power systems can be written as:

$$\begin{aligned}&\min_{\boldsymbol{x},\boldsymbol{m}} f(\boldsymbol{x}),\\&s.t.\ h_1(\boldsymbol{x},\boldsymbol{m})=0,\ h_2(\boldsymbol{x})=\boldsymbol{\alpha}_0^T\boldsymbol{x}+\boldsymbol{\beta}_0=0,\\&g_1(\boldsymbol{x})=\boldsymbol{\alpha}_1^T\boldsymbol{x}+\boldsymbol{\beta}_1\leq 0,\ \ g_2(\boldsymbol{m})=\boldsymbol{\alpha}_2^T\boldsymbol{m}+\boldsymbol{\beta}_2\leq 0,\end{aligned} \tag{3-18}$$

where the objective function $f(\boldsymbol{x})$ denotes the f in (3-1). Matrices $\boldsymbol{\alpha}_0$-$\boldsymbol{\alpha}_2$ and $\boldsymbol{\beta}_0$-$\boldsymbol{\beta}_2$ are coefficient matrices. The equality constraint h_1 indicates the bilinear coupling constraints between ***x*** and ***m***, including (3-5), (3-7), and (3-9). The equality constraint h_2 denotes the linear constraints on ***x*** only, including (3-2)-(3-3), (3-6), and supplemental constraints related to (3-7). The inequality constraint g_1 represents the linear constraints on ***x*** only, including (3-4) and (3-13)-(3-17). The inequality constraint

g_2 denotes the linear constraints on ***m*** only, including (3-11)-(3-12). Since the equation (3-8) is applied to eliminate the node mass flow, there are not equality constraints on ***m*** only.

3.3 Model Analysis and Decomposition

The challenge of solving the optimization model (3-18) is that it is a non-convex program with bilinear constraints $h_1(\boldsymbol{x},\boldsymbol{m})=0$. Although the problem (3-18) is non-convex, if ***m*** is fixed, it will become a standard quadratic problem, which is easy and convenient to solve.

In the proposed solution method, the ***m*** is treated as the complicating variable. Thus, as shown in Figure 3-2, the problem (3-18) can be decomposed into a convex sub-problem with fixed ***m*** and a master problem which optimizes and updates ***m***:

1) If the sub-problem is feasible, the master problem updates ***m*** based on the sensitivity calculated by the sub-problem;
2) If the sub-problem is infeasible, the master problem revises the ***m*** by removing infeasible ***m*** according to cutting planes generated by sub-problems.

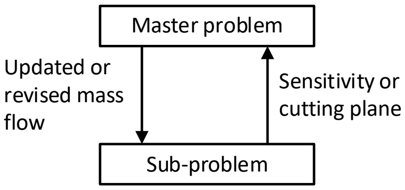

Figure 3-2. The architecture of the proposed decomposition method.

Similar to GBD, if a feasible initial case is given, the proposed solution method can find a local optimum which is better than or equal to the initial case.

3.3.1 Convex Sub-Problem

The sub-problem solves the convex problem (3-19) constructed by fixing ***m***:

$$\begin{aligned}&\min_{\boldsymbol{x}} f(\boldsymbol{x}),\\ &s.t.\ h_1(\boldsymbol{x},\boldsymbol{m}^k)=0,\ \ h_2(\boldsymbol{x})=\boldsymbol{\alpha}_0^T\boldsymbol{x}+\boldsymbol{\beta}_0=0, g_1(\boldsymbol{x})=\boldsymbol{\alpha}_1^T\boldsymbol{x}+\boldsymbol{\beta}_1\le 0,\end{aligned} \tag{3-19}$$

where $\boldsymbol{m}^k$ indicates the variable ***m*** at *k* th iteration.

The problem (3-19) is a standard convex problem because 1) the objective function is convex, and 2) all constraints are linear.

3.3.2 Master Problem

The master problem is a mapping of the optimal cost function respect to the mass flow ***m***, which is formulated with fixed ***x***:

$$\begin{aligned}&\min_{\boldsymbol{m}} J^*(\boldsymbol{m}),\\ &s.t.\ \ \boldsymbol{m} \in M \bigcap FC,\end{aligned} \tag{3-20}$$

where $J^*(\boldsymbol{m})$ is the optimal cost function of mass flow ***m***. M indicates the parameter space of pipe mass flow ***m*** constructed by (3-11) and (3-12), and FC indicates the feasible cuts i.e., cutting planes.

3.4 Solution Method

The sub-problem and master problem are solved iteratively according to the following two steps:

First, the sub-problem (3-19) is solved. If the sub-problem is feasible, the envelope theorem is used to analyze the sensitivity of ***m***. If the sub-problem is infeasible, Outer Approximation [73] [74] is utilized to produce cutting planes.

Second, the master problem (3-20) uses the gradient projection [75] to update ***m*** if the sub-problem is feasible. And it removes infeasible ***m*** from the original parameter space based on cutting planes if the sub-problem is infeasible.

3.4.1 Sub-Problem

With fixed ***m***, the sub-problem (3-19) is a standard convex problem. In this paper, CPLEX is employed to solve the sub-problem.

3.4.1.1 Feasible Sub-Problem

If the sub-problem is feasible, the sensitivity of the optimal cost function with respect to the mass flow ***m***, which denotes the gradient, is calculated by the envelope theorem:

$$\frac{\partial J^*(\boldsymbol{m}^k)}{\partial m_{i,t}} = \left.\frac{\partial f^*(\boldsymbol{x})}{\partial m_{i,t}}\right|_{\boldsymbol{x}=\boldsymbol{x}^k,\boldsymbol{m}=\boldsymbol{m}^k} = \left.\frac{\partial L(\boldsymbol{x},\boldsymbol{m})}{\partial m_{i,t}}\right|_{\boldsymbol{x}=\boldsymbol{x}^k,\boldsymbol{m}=\boldsymbol{m}^k}, \tag{3-21}$$

where f^* is the optimal cost function, and $L(\boldsymbol{x},\boldsymbol{m})$ is the Lagrangian function of the sub-problem. Scalar $\boldsymbol{x}^k$ is the variable ***x*** at *k* th iteration.

3.4.1.2 Infeasible Sub-Problem

If the sub-problem is infeasible, the cutting planes are generated for the master problem to remove corresponding infeasible $\boldsymbol{m}$ from the original parameter space M. First, the relaxed sub-problem in (3-22) is solved:

$$\begin{aligned}&\min_{\boldsymbol{x},\boldsymbol{s}} \sum_i s_i,\\ &s.t.\ h_1(\boldsymbol{x},\boldsymbol{m}^k)=0, h_2(\boldsymbol{x})=\boldsymbol{\alpha}_0^T\boldsymbol{x}+\boldsymbol{\beta}_0=0, g_1(\boldsymbol{x})=\boldsymbol{\alpha}_1^T\boldsymbol{x}+\boldsymbol{\beta}_1\le\boldsymbol{s},\end{aligned}\quad, \tag{3-22}$$

where s_i is the slack variable for the i th inequality constraint, and $\boldsymbol{s}$ is the vector of slack variables.

Second, the cutting plane is calculated by Outer Approximation [73][74] since the problem (3-22) is a convex program with all constraints linear:

$$\left(\bar{\boldsymbol{\lambda}}^k\right)^T\left[\nabla_{\boldsymbol{m}}h_1(\boldsymbol{x}^k,\boldsymbol{m}^k)^T(\boldsymbol{m}-\boldsymbol{m}^k)\right]+\left(\bar{\boldsymbol{\mu}}^k\right)^T g_1(\boldsymbol{x}^k)\le 0, \tag{3-23}$$

where $\bar{\boldsymbol{\lambda}}^k$ and $\bar{\boldsymbol{\mu}}^k$ are Lagrangian multipliers of h_1 and g_1 in the problem (3-22) at k th iteration, respectively.

After (3-21) is solved, the values of $\bar{\boldsymbol{\lambda}}^k$, $\bar{\boldsymbol{\mu}}^k$, $\nabla_{\boldsymbol{m}}h_1(\boldsymbol{x}^k,\boldsymbol{m}^k)^T$, and $g_1(\boldsymbol{x}^k)$ are all known. Thus, inequality (3-23) is linear with variable $\boldsymbol{m}$ only, and it defines a cutting plane which removes infeasible $\boldsymbol{m}$ from the original parameter space M. Given by Outer Approximation, the cutting plane (3-23) is an over-estimation of the accurate cutting plane that can accelerate the calculation by reducing iteration times [76].

3.4.2 Master Problem

The challenge of solving the master problem (3-20) is that the closed-form expression of J^* is unknown. In this section, the gradient projection is applied to linearize the J^* around the $\boldsymbol{m}^k$ [75]. Therefore, the master problem can be solved iteratively with a local optimum.

4.4.2.1 Feasible Sub-Problem

If the sub-problem (3-19) is feasible, the mass flow is updated by moving along the anti-gradient direction:

$$\boldsymbol{m}^{k+1}=\boldsymbol{m}^k-\left(\alpha^k\boldsymbol{P}^k\right)\frac{\partial J^*(\boldsymbol{m}^k)}{\partial\boldsymbol{m}}, \tag{3-24}$$

where α^k is the step size at k th iteration, and the fixed step size is adopted in this chapter. The gradient term in (3-24) is provided by the sub-problem as in (3-22). Matrix $\boldsymbol{P}^k$ is the projection matrix at *k* th iteration which incorporates possible active boundary constraints (3-11)-(3-12) and cutting planes (3-23):

$$\boldsymbol{P}^k = \boldsymbol{I} - \boldsymbol{H}_A^k\left(\left(\boldsymbol{H}_A^k\right)^T \boldsymbol{H}_A^k\right)^{-1}\left(\boldsymbol{H}_A^k\right)^T, \tag{3-25}$$

where $\boldsymbol{H}_A^k$ is the matrix of possible active constraints, for more details, see [77].

4.4.2.2 Infeasible Sub-Problem

If the sub-problem (3-18) is infeasible, the master problem revises $\boldsymbol{m}$ according to cutting planes, in which the revised mass flow $\boldsymbol{m}^{k+1}$ in (3-26) denotes the intersection of the gradient direction and the cutting plane:

$$\boldsymbol{m}^{k+1} = \boldsymbol{m}^r - \beta^k \frac{\partial J^*(\boldsymbol{m}^r)}{\partial \boldsymbol{m}}, \tag{3-26}$$

where *r* indicates the last successful iteration, and β^k indicates the revised step size:

$$\beta^k = \frac{\left(\bar{\boldsymbol{\lambda}}^k\right)^T \left[\nabla_{\boldsymbol{m}} h_1(\boldsymbol{x}^k, \boldsymbol{m}^k)^T \left(\boldsymbol{m}^r - \boldsymbol{m}^k\right)\right] + \left(\bar{\boldsymbol{\mu}}^k\right)^T g_1(\boldsymbol{x}^k)}{\left(\bar{\boldsymbol{\lambda}}^k\right)^T \left[\nabla_{\boldsymbol{m}} h_1(\boldsymbol{x}^k, \boldsymbol{m}^k)^T\right]\left(\dfrac{\partial f(\boldsymbol{x}^r, \boldsymbol{m}^r)}{\partial \boldsymbol{m}}\right)}, \tag{3-27}$$

Remark 3-1: When solving the master problem, if the sub-problem is feasible, compared with the "optimal cut" in the GBD [33], the proposed solution method does not cut the parameter space which has a higher overall cost than the upper bound but moves to the direction of reducing overall cost.

For clarity, the calculation process of the master problem is illustrated in Figure 3-3.

1) First, from $\boldsymbol{m}^k$ to $\boldsymbol{m}^{k+1}$, the master problem updates mass flow based on the gradient with projection according to (3-24), because if the projection is not considered, the mass flow will step out the parameter space *M* (blue area).
2) Second, the process from $\boldsymbol{m}^{k+1}$ to $\boldsymbol{m}^{k+2}$ updates the mass flow according to (3-24) in the gradient direction without projection, where $\boldsymbol{P}^k = \boldsymbol{I}$.
3) Next, after the process from $\boldsymbol{m}^{k+2}$ to $\boldsymbol{m}^{k+3}$, the new mass flow $\boldsymbol{m}^{k+3}$ is not in the parameter space *M*, which causes the infeasible sub-problem. Thus, the cutting plane (yellow area) is generated according to (3-23).
4) Forth, the process from $\boldsymbol{m}^{k+3}$ to $\boldsymbol{m}^{k+4}$ indicates the process (3-26) of revising mass flow, which removes infeasible mass flow from *M*. The $\boldsymbol{m}^{k+4}$ is the

intersection point of the gradient direction and the cutting plane.

5) Last, the process from $\boldsymbol{m}^{k+4}$ to $\boldsymbol{m}^{k+5}$ finds the local optimum point $\boldsymbol{m}^{k+5}$ which satisfies stopping criterion; Therefore, the iteration stops at $\boldsymbol{m}^{k+5}$.

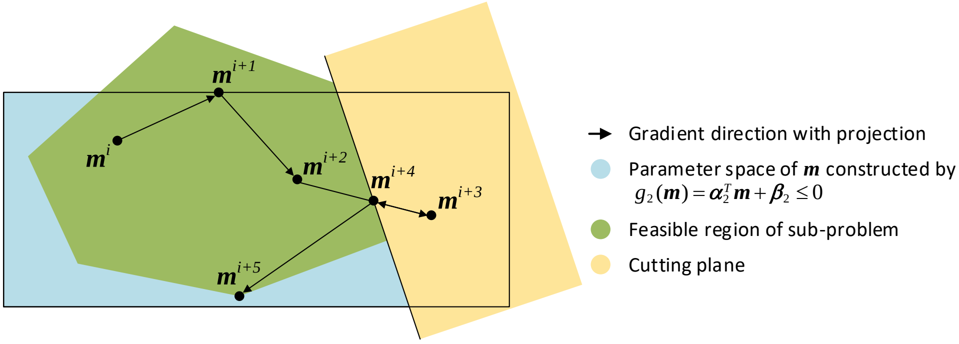

Figure 3-3. The iteration processes of the master problem.

The convergence criterion is defined as:

$$\left|\frac{(J^*)^k-(J^*)^{k-1}}{(J^*)^1}\right|\le\varepsilon_{ED}. \tag{3-28}$$

where ε_{ED} is the maximum tolerance. If (3-28) is satisfied, the iteration will stop at k th iteration with the optimal cost $(J^*)^k$.

3.5 Case Studies

In case studies, the proposed method is tested and compared with two existing approaches:

1) The economic dispatch (3-18) directly solved by the solver IPOPT which is effective and efficient for non-convex programs (direct method);
2) The traditional fixed mass flow method [78] solved by CPLEX (traditional method).

It is noticed that in the traditional method, mass flow is the given value rather than the decision variable. Programs are coded using MATLAB, where the YALMIP is used to provide the socket between the optimizers and the MATLAB. And the computational time are calculated based on a PC with i5-4590 CPU and 8GM RAM.

3.5.1 Case 1: Simulation Based on the Test System

The combined heat and power system in Figure 3-4 has a 6-node electric power system and a 6-node heat system with a CHP unit [27][39]. The proposed method is tested under the following two scenarios.

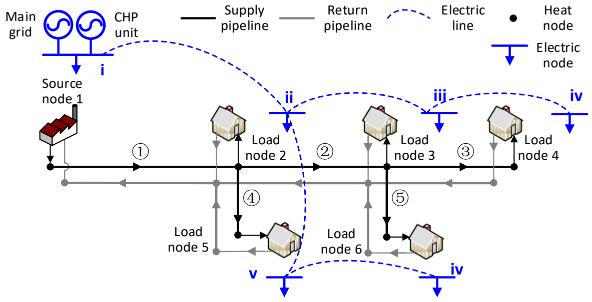

Figure 3-4. The topology of the combined heat and power test system.

3.5.1.1 Scenario 1: Test of Optimality

In the first scenario, the optimality of the proposed method is compared with the direct method and the traditional method. As shown in Table 3-1, the proposed method has the optimal cost of \$594.31, which is very close to the result \$594.19 solved by the direct method. Influenced by the step-size and convergence tolerance, although there are small gaps between the solutions of the proposed method and the direct method, the optimality of the proposed method is the same as the direct method. Also, it is noticed that both the direct method and the proposed method have lower costs compared with the traditional method, which demonstrates varying mass flow improves the system's overall efficiency.

Table 3-1. The given condition and result of scenario 1

Methods	Traditional method	Direct method	Proposed method
Given mass flow	$1.05\hat{\boldsymbol{m}}^* + \boldsymbol{r}_d$	$1.05\hat{\boldsymbol{m}}^* + \boldsymbol{r}_d$	$1.05\hat{\boldsymbol{m}}^* + \boldsymbol{r}_d$
Overall costs	598.40	594.19	594.31

where $\hat{\boldsymbol{m}}^*$ indicates a local optimum of the problem (3-18). Matrix $\boldsymbol{r}_d$ denotes the matrix of random variables from 0-1.

3.5.1.2 Scenario 2: Test of Convergence

In the second scenario, the proposed method reduces 3.63% of the overall cost compared with the traditional method. However, the direct method fails to converge. The possible reason is the initial mass flow for the direct method in scenario 2 is not good for solver IPOPT to converge under finite iterations.

Table 3-2. The given condition and result of scenario 2

Methods	Traditional method	Direct method	Proposed method
Given mass flow	$\widehat{\boldsymbol{m}}$	$\widehat{\boldsymbol{m}}$	$\widehat{\boldsymbol{m}}$
Overall costs	635.44	-	612.40

where $\widehat{\boldsymbol{m}}$ is a feasible solution of (3-18) given from experience, in which the mass flow is 15kg/s for all load nodes.

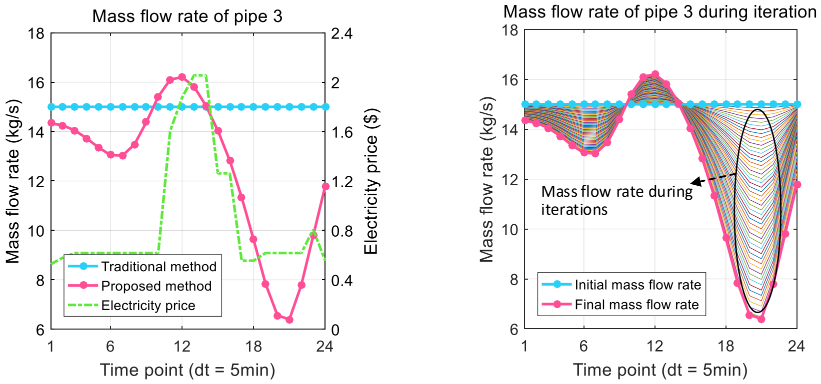

(a) (b)

Figure 3-5. Mass flow of pipe 3 (a) of the traditional method and the proposed method and (b) of the proposed method during iterations in the second scenario.

In scenario 2, as presented in Figure 3-5 (a), compared with the traditional method, the mass flow in the proposed method is iteratively optimized following the electricity price, which could be observed in Figure 3-5 (b). As a result, the heat pipeline storage ability can be better utilized, which improves the electric power system's flexibility. Therefore, in Figure 3-6, the CHP unit in the proposed method generates more heat power during 11:50-12:20 than the traditional method. Considering the positive correlation of CHP electric and heat power outputs shown in Figure 3-6, the CHP unit generates more electricity during 11:50-12:20 to reduce high-price electricity purchase from the grid. In conclusion, the efficiency of the total system is improved using the flexibility from adjusting mass flow.

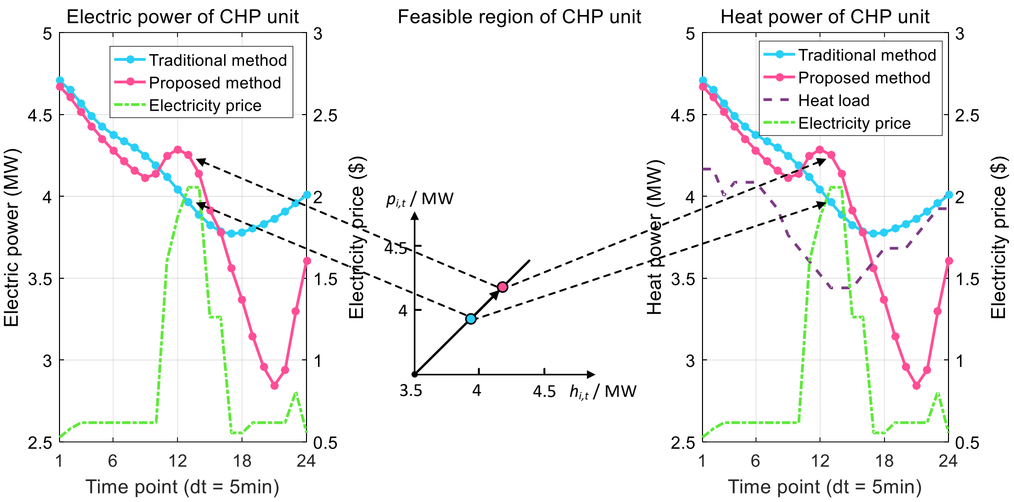

Figure 3-6. The CHP electric and heat power outputs of the traditional method and the proposed method in scenario 2.

In summary, the proposed method can iteratively solve the optimization problem (3-21) and find a local optimum which is better than the traditional method. Under the small disturbance, the local optimums of the proposed method and the IPOPT are very close; Under different given initial values, the proposed method can avoid the divergence problem of solver IPOPT.

3.5.2 Case 2: Simulation Based on the Barry Island System

In Figure 3-7, the proposed method is investigated based on a real system in the modified Barry Island system situated in South Wales with a 9-node electric power system and a 33-node heat system [72].

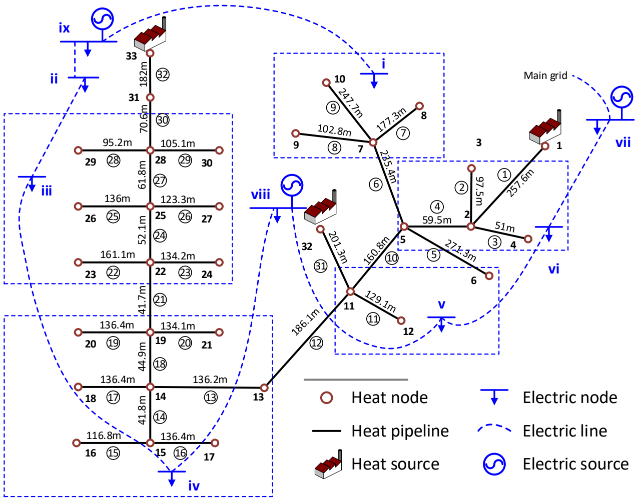

Figure 3-7. The topology of the modified Barry Island system.

Table 3-3. Performance Comparison for Barry Island System

Approach	Traditional method	Direct method	Proposed method
Overall costs ($)	1.704×10^3	-	1.692×10^3

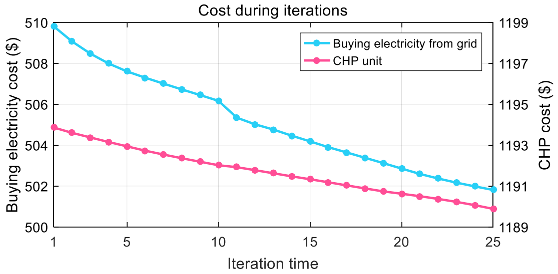

Figure 3-8. The cost of the proposed method during iterations.

As shown in Table 3-3 and Figure 3-8, the proposed method reduces the overall cost by 0.95% compared with the traditional method. During iterations, the costs of CHP units and buying electricity from the grid are both reduced. However, the direct method fails to converge, which may be a result of the initial mass flow or the complexity from DERs: The initial mass flow could affect the interior point method used by IPOPT to find a better case, and the multiple DERs increase bilinear constraints (3-5) and (3-9), making the problem extremely complex to solve. But as shown in Figure 3-9, the proposed method can overcome the above difficulties and find a local optimum.

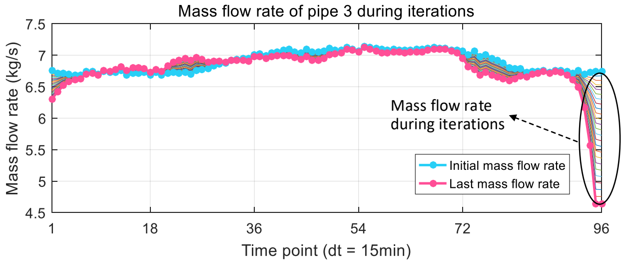

Figure 3-9. The mass flow rate of pipe 3 during iterations.

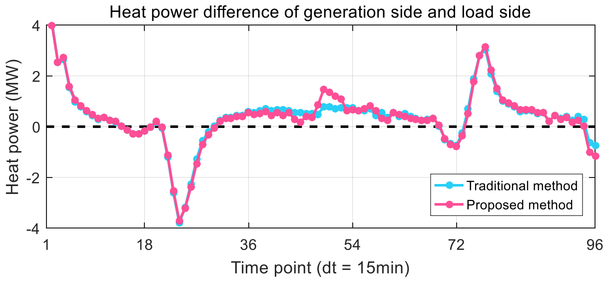

Figure 3-10. The difference of heat power between generation side and load side.

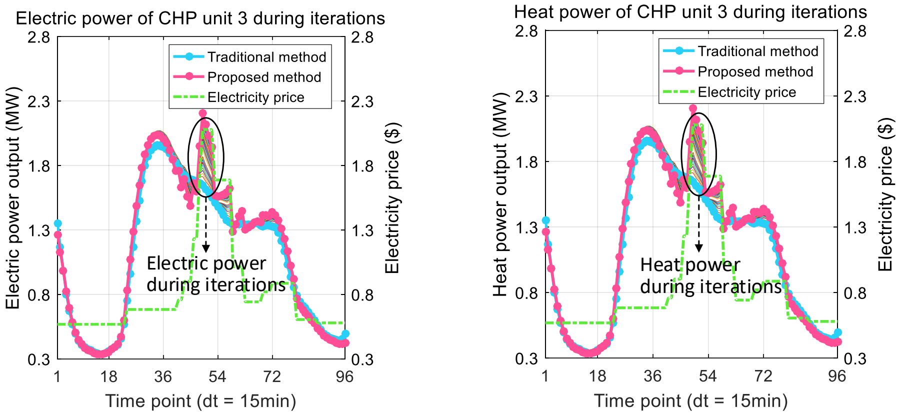

(a) (b)

Figure 3-11. The (a) electric power and (b) heat power outputs of CHP unit 3.

On the one hand, compared with the traditional method, the proposed method reduces 1.57% of electricity purchase cost from the grid. This improvement is achieved from the adjustment of mass flow in Figure 3-9 because the heat pipeline storage is better utilized: when the mass flow is optimized, the allowed heat unbalanced power between the generation side and the load side increases during 11:45 to 13:15 in Figure 3-10. As a result, in the proposed method, the CHP units can generate more heat power during 11:45 to 13:15. Due to the electric-heat coupling characteristics, CHP units can generate more electric power during 11:45 to 13:15 when the electricity price is high. This phenomenon is obvious in Figure 3-11 (a) and (b) as circled.

On the other hand, adjusting the mass flow can reduce heat loss according to the heat pipeline model (3-7). In this case, the proposed method has reduced 3.43% heat energy loss compared with the traditional method. Thus, the system operator can satisfy the same load demand with higher efficiency compared with the traditional method.

Briefly, the proposed method can overcome the non-convergence problem of the direct method. Compared with the traditional method, the proposed method can reduce the overall costs by utilizing flexibility from adjusting mass flow.

In terms of calculation efficiency, total calculation time is about 12.025s, where the average solving CPU time is 0.165s for each convex sub-problem, and the average time consumption of the master problem is 0.316s. Under the convergence tolerance $\delta = 2\times10^{-4}$ the proposed method converged at 25 times, which can be used in the day-ahead or intra-day dispatch.

3.6 Conclusion

In this chapter, the proposed synchronous dispatch increases the flexibility of combined heat and power dispatch through adjusting mass flow. By developing a nonlinear heating system model, the complexity from the integers in existing MINLPs is eliminated without compromising on accuracy. The proposed solution method overcomes the simplification of the optimization model in existing methods and accelerates the calculation. In case studies, compared with the traditional method, the proposed method has a lower overall cost without any additional devices. Compared with the direct method solved by IPOPT, the proposed method can avoid divergence problems.

Chapter 4: Asynchronous Economic Dispatch

4.1 Overview

Limited by the long dynamic process and large heat inertia, the heating system may not be adjusted as fast as the electric power system [5][17]. For example, the electric power system is usually dispatched in minutes because of the short dynamic time and the requirement of real-time power balance, while some heating systems are adjusted in hours. However, the different adjustment time scales of electricity and heat are ignored in traditional synchronous dispatch methods, which threatens the system security and efficiency. Thus, the asynchronous dispatch method is proposed in this chapter to incorporate the different adjustment time scales of the two energy systems, and the contributions are:

1) Two asynchronous economic dispatch models i.e., hybrid model and identical model, are proposed which incorporates the different adjustment time scales of the electric power system and the heating system.
2) The influence of dispatch intervals on the overall costs and computational efficiency is studied in the case simulation.
3) The necessity of using the asynchronous time scale dispatch method is demonstrated from the comparison with the synchronous dispatch method.

It is noticed the asynchronous dispatch is a generalization of synchronous dispatch, which indicates the synchronous dispatch is a special case of asynchronous dispatch with the same dispatch interval of electricity and heat. The asynchronous dispatch can be used for the economic dispatch with both variable mass flow and fixed mass flow. For clarity of model formulation and case analysis, we adopt the fixed mass flow adjustment in this chapter for example.

4.2 Hybrid Time Scale Model

The first asynchronous dispatch model is the hybrid time scale model (hybrid model). In the hybrid model, as illustrated in the Figure 4-1, the adjustment time scale of the two energy systems are different: The electric power system adopts a shorter dispatch interval Δt_E for its real-time generation-demand balance, while the heating system uses a longer dispatch interval Δt_H due to its control mechanism and large inertia.

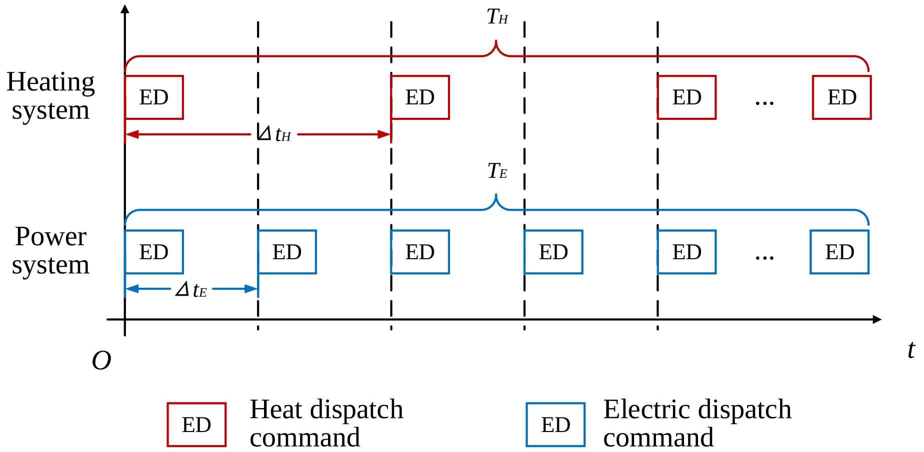

Figure 4-1. The dispatch command in the hybrid time scale model.

In Figure 4-1, T_E and T_H are the total number of dispatch time sections in the electric power system and the heating system, respectively. Generally, in the hybrid model, $T_H \leq T_E$. As a result, the number of constraints in the heating system is less than the electric power system.

4.2.1 Objective Function

The objective function of the hybrid model is to minimize the total generation costs of all energy sources at all time sections:

$$\begin{aligned}\min_{p_{i,t},h_{i,t}} f = &\sum_{i\in G}\sum_{t=1}^{T_E}\left[CT_{i,t}(p_{i,t})+CG_{i,t}(p_{i,t})\right]\Delta t_E \\ &+\sum_{i\in G}\left[\sum_{t=1}^{T_E} CC_{i,t}(p_{i,t},h_{i,t})\Delta t_E + \sum_{t=1}^{T_H} CC_{i,t}(h_{i,t})\Delta t_H\right],\end{aligned} \tag{4-1}$$

where $CT_{i,t}(p_{i,t})$ and $CG_{i,t}(p_{i,t})$ indicates the cost function of thermal generators and electricity purchase from the grid, respectively. Scalars $CC_{i,t}(p_{i,t},h_{i,t})$ and $CC_{i,t}(h_{i,t})$ denote the different terms in the cost functions of CHP units which related to and do not related to electric power, respectively.

The cost function of thermal generators and CHP units are expressed using quadratic functions of electricity and heat productions [27]:

$$CT_{i,t}(p_{i,t}) = \eta_{i,t,0} + \eta_{i,t,1} p_{i,t} + \eta_{i,t,2} p_{i,t}^2, \tag{4-2a}$$

$$CC_{i,t} = \underbrace{\eta_{i,t,0} + \eta_{i,t,1} p_{i,t} + \eta_{i,t,2} p_{i,t}^2 + \eta_{i,t,5} p_{i,t} h_{i,t}}_{CC_{i,t}(p_{i,t},h_{i,t})} + \underbrace{\eta_{i,t,3} h_{i,t} + \eta_{i,t,4} h_{i,t}^2}_{CC_{i,t}(h_{i,t})} . \tag{4-2b}$$

The cost function of the electricity purchase from the main grid is:

$$CG_{i,t}(p_{i,t}) = C_t^G p_{i,t} , \tag{4-2c}$$

where C_t^G is the time-of-use at time *t*.

4.2.2 Electric Power System Constraints

In the electric power system, the DC power flow model is adopted. The real-time electric power balance is required between the generation side and the load side:

$$\sum_{i\in G} p_{i,t} = \sum_{i\in E} d_{i,t} \quad t=1,\,2,\,\cdots T_E . \tag{4-3}$$

The electric line power $l_{i,t}$ of line *i* at time *t* is calculated by

$$l_{i,t} = \sum_{j\in E} SF_{i,j} \cdot (p_{j,t} - d_{j,t}) \quad \forall i \in L,\ t=1,\,2,\,\cdots T_E , \tag{4-4}$$

The line power flow should be below its thermal limitation:

$$\underline{l}_{i,t} \le \sum_{j\in E} SF_{i,j} \cdot (p_{j,t} - d_{j,t}) \le \overline{l}_{i,t} \quad \forall i \in L,\ t=1,\,2,\,\cdots T_E . \tag{4-5}$$

4.2.3 Heating System Constraints

In the heating system, the mass flow is the given variable value, which is widely adopted in the literature [24][25][36].

The heat nodes exchange heat power with the heat supply and return networks through heat exchangers:

$$h_{i,t} = c_p m_{i,t}^n (T_{i,t}^{NS} - T_{i,t}^{NR}) \quad \forall i \in H,\ t=1,\,2,\,\cdots T_H . \tag{4-6}$$

In the heat supply network, for load nodes $T_{i,t}^{NS} = T_{i,t}^S$, and for source nodes $T_{i,t}^S$ is calculated by (4-9a). Similarly, in the heat return network, for load nodes $T_{i,t}^R$ is calculated by (4-9b), and for source nodes $T_{i,t}^{NR} = T_{i,t}^R$. It is noticed here all $t=1,\,2,\,\cdots T_H$.

To ensure the heat exchanger's working conditions, the exchanger supply and return temperatures should satisfy:

$$\underline{T}_i^{NS} \le T_{i,t}^{NS} \le \overline{T}_i^{NS} \quad \forall i \in H,\ t=1,\,2,\,\cdots T_H , \tag{4-7a}$$

$$\underline{T}_i^{NR} \le T_{i,t}^{NR} \le \overline{T}_i^{NR} \quad \forall i \in H,\ t=1,\ 2,\ \cdots T_H\ . \tag{4-7b}$$

To avoid the heat pipeline storage is exhausted, the generated heat energy is required to be no less than the load heat energy within scheduling periods:

$$\sum_{t=1}^{T_H}\left(\sum_{i\in H_G} h_{i,t} - \sum_{i\in H_L} h_{i,t}\right)\Delta t_H \ge 0\,. \tag{4-8}$$

The node temperature mixing equations are applied to calculate node temperature from its injecting pipe end temperature:

$$\begin{gathered}\left(m^n_{i\in H_G,t} + \sum_j m_{j,t}\right)T^S_{i,t} = \left(m^n_{i\in H_G,t}T^{NS}_{i\in H_G,t}\right) + \left(\sum_j m_{j,t}\tau^{SE}_{j,t}\right),\\ \forall i\in H,\ j\in P_S \cap In(i),\ t=1,\ 2,\ \cdots T_H\end{gathered} \tag{4-9a}$$

$$\begin{gathered}\left(m^n_{i\in H_L,t} + \sum_j m_{j,t}\right)T^R_{i,t} = \left(m^n_{i\in H_L,t}T^{NR}_{i\in H_L,t}\right) + \left(\sum_j m_{j,t}\tau^{RE}_{j,t}\right).\\ \forall i\in H,\ j\in P_R \cap In(i),\ t=1,\ 2,\ \cdots T_H\end{gathered} \tag{4-9b}$$

The pipe initial temperature equals to the temperature of its connecting node:

$$\tau^{SI}_{j,t} = T^S_{i,t} \quad j\in P_S \cap Lv(i),\ \ i\in H,\ t=1,\ 2,\ \cdots T_H\ , \tag{4-10a}$$

$$\tau^{RI}_{j,t} = T^R_{i,t} \quad j\in P_R \cap Lv(i),\ \ i\in H,\ t=1,\ 2,\ \cdots T_H\,. \tag{4-10b}$$

The pipeline model describes heat dynamic process based on the dynamic pipeline model [27][10]:

$$\tau'^{SE}_{i,t} = \sum_{k=t-\varphi_{i,t}}^{t-\gamma_{i,t}} K_{i,t,k}\tau^{SI}_{i,k} \quad \forall i\in P_S,\ t=1,\ 2,\ \cdots T_H\ , \tag{4-11a}$$

$$\tau'^{RE}_{i,t} = \sum_{k=t-\varphi_{i,t}}^{t-\gamma_{i,t}} K_{i,t,k}\tau^{RI}_{i,k} \quad \forall i\in P_R,\ t=1,\ 2,\ \cdots T_H\ , \tag{4-11b}$$

where $\tau'^{SE}_{i,t}$ and $\tau'^{RE}_{i,t}$ are pipe end temperature without heat loss of pipe *i* at time *t*. Coefficients $K_{i,t,k}$ indicate the weights of the historical temperature:

$$K_{i,t,k} = \begin{cases} \dfrac{m_{i,t}\Delta t_H - S_{i,t} + \rho A_i x_i}{m_{i,t}\Delta t_H}, k = t-\varphi_{i,t} \\ \dfrac{m_{i,k}\Delta t_H}{m_{i,t}\Delta t_H}, k = t-\varphi_{i,t}+1, \ldots, k = t-\gamma_{i,t}+1 \\ \dfrac{R_{i,t} - \rho A_i x_i}{m_{i,t}\Delta t_H}, k = t-\gamma_{i,t} \\ 0, otherwise \end{cases}, \tag{4-12}$$

in which the integer intermediate variables $\gamma_{i,t}$ and $\varphi_{i,t}$ denote the time delays calculated by:

$$\gamma_{i,t} = \min_{n} \left\{ n : s.t. \sum_{k=0}^{n} (m_{i,t-k} \cdot \Delta t_H) \geq \rho A_i x_i, n \geq 0, n \in Z \right\}, \tag{4-13a}$$

$$\varphi_{i,t} = \min_{m} \left\{ m : s.t. \sum_{k=1}^{m} (m_{i,t-k} \cdot \Delta t_H) \geq \rho A_i x_i, m \geq 0, m \in Z \right\}, \tag{4-13b}$$

where $R_{i,t}$ and $S_{i,t}$ are two intermediate variables:

$$R_{i,t} = \sum_{k=0}^{\gamma_{i,t}} (m_{i,t-k} \cdot \Delta t_H), \tag{4-14a}$$

$$S_{i,t} = \begin{cases} \sum_{k=0}^{\varphi_{i,t}-1} (m_{i,t-k} \cdot \Delta t_H), if\, \varphi_{i,t} \geq \gamma_{i,t} + 1 \\ R_{i,t}, otherwise \end{cases}. \tag{4-14b}$$

The heat pipe end temperature is calculated by considering the heat loss:

$$\tau_{i,t}^{SE} = T_{i,t}^{a} + (\tau_{i,t}'^{SE} - T_{i,t}^{a}) \times \exp\left[-\frac{\lambda_i \Delta t_H}{A_i \rho c_p} \left(\gamma_{i,t} + \frac{1}{2} + \frac{S_{i,t} - R_{i,t}}{m_{i,t-\gamma_{i,t}} \Delta t_H} \right) \right], \quad \forall i \in P_S,\ t=1, 2, \cdots T_H \tag{4-15a}$$

$$\tau_{i,t}^{RE} = T_{i,t}^{a} + (\tau_{i,t}'^{RE} - T_{i,t}^{a}) \times \exp\left[-\frac{\lambda_i \Delta t_H}{A_i \rho c_p} \left(\gamma_{i,t} + \frac{1}{2} + \frac{S_{i,t} - R_{i,t}}{m_{i,t-\gamma_{i,t}} \Delta t_H} \right) \right]. \quad \forall i \in P_R,\ t=1, 2, \cdots T_H \tag{4-15b}$$

4.2.4 Energy Sources Constraints

4.2.4.1 Combined Heat and Power Units

The feasible regions of different CHP units are shown in Figure 2-5 (a) and (b) and described by polytopes in equation (4-16a) and (4-16b), respectively [36][67]. Different from the extraction condensing CHP units, the electric and heat power outputs of back-pressure CHP units have a linear relationship. Therefore, the electric power of back-pressure units follows the heat adjustment time scale.

$$B_{k,i} p_{i,t} + K_{k,i} h_{i,t} \leq v_{k,i} \quad \forall i \in G,\ t=1, 2, \cdots T_E, \tag{4-16a}$$

$$B_{k,i} p_{i,t} + K_{k,i} h_{i,t} = v_{k,i} \quad \forall i \in G,\ t=1, 2, \cdots T_H. \tag{4-16b}$$

The ramping constraint indicates the increment or decrement of the source power outputs within a single period should not exceed the ramping capacity:

$$D_{e,i} \cdot \Delta t_E \le p_{i,t} - p_{i,t-1} \le U_{e,i} \cdot \Delta t_E \quad \forall i \in G,\ t=1,2,\cdots T_E, \tag{4-17}$$

$$D_{h,i} \cdot \Delta t_H \le h_{i,t} - h_{i,t-1} \le U_{h,i} \cdot \Delta t_H \quad \forall i \in G,\ t=1,2,\cdots T_H. \tag{4-18}$$

Moreover, the CHP unit's supply temperature is usually set by operators:

$$T_{j,t}^{NS} = T_{i,t}^{Set} \quad \forall i \in G,\ j=\mathit{\Gamma}_G(i),\ t=1,2,\cdots T_H, \tag{4-19}$$

where $\mathit{\Gamma}_G(i)$ is a mapping between a heat node and an energy source node.

4.2.4.2 Thermal Generator and Main Grid

Since the thermal generator and the main grid only outputs electric power, the dispatch interval follows the electric adjustment time scale. The power outputs of the thermal generator and the main grid at energy source *i* follow (4-20), and at the same time the thermal generator should satisfy ramping constraints (4-18).

$$\underline{p}_{i,t} \le p_{i,t} \le \overline{p}_{i,t} \quad \forall i \in G,\ t=1,2,\cdots T_E, \tag{4-20}$$

where the $\underline{p}_{i,t}$ and $\overline{p}_{i,t}$ indicate the minimum and maximum electric power outputs of energy source *i* at time *t*.

4.3 Identical Time Scale Model with Additional Constraints

Another asynchronous economic dispatch model is called the identical time scale model (identical model): The idea is to add equality constraints to the traditional synchronous dispatch model. As shown in Figure 4-2, the electric power system and the heating system both adopt the short electric dispatch interval, i.e., $\Delta t = \Delta t_E$ where Δt is the dispatch interval in the identical model.

To deal with the long adjustment time scale of the heating system, additional equality constraints (yellow blocks in Figure 4-2) are added to guarantee the heat decision variables are invariable during each Δt_H. With these additional constraints, the asynchronous economic dispatch can be realized which satisfies the different adjustment abilities of the two energy systems. Compared with the hybrid model, the identical model has more constraints but the same results, which will be verified in case studies.

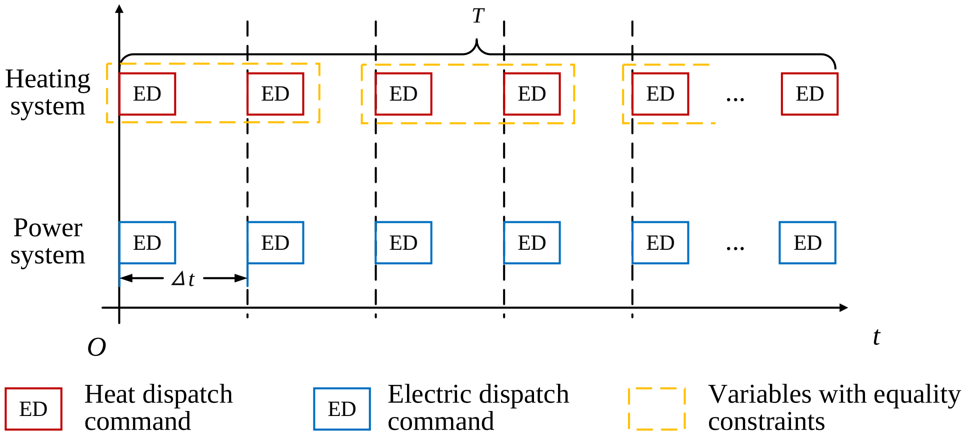

Figure 4-2. The dispatch command in the identical model.

4.3.1 Objective Function

The objective function of the identical model is to minimize the total generation costs of all energy sources at all time intervals:

$$\min_{p_{i,t},h_{i,t}} f=\sum_{i\in G}\sum_{t=1}^{T_E}\left[CT_{i,t}(p_{i,t})+CG_{i,t}(p_{i,t})\right]\Delta t+\sum_{i\in G}\sum_{t=1}^{T_E}\left[CC_{i,t}(p_{i,t},h_{i,t})+CC_{i,t}(h_{i,t})\right]\Delta t\,. \tag{4-21}$$

Derive $k_E\Delta t=k_E\Delta t_E=\Delta t_H$ into (4-21), the (4-21) equals to (4-1), where k_E is an integer coefficient to describe the relationship between the time interval of the electric power system and the heating system.

4.3.2 Electric Power System Constraints

In the electric power system, the constraints in the identical model are the same as that in the hybrid method:

$$\sum_{i\in G} p_{i,t}=\sum_{i\in E} d_{i,t} \quad t=1,\,2,\,\cdots T\,, \tag{4-22}$$

$$l_{i,t}=\sum_{j\in E} SF_{i,j}\cdot(p_{j,t}-d_{j,t}) \quad \forall i\in L,\ t=1,\,2,\,\cdots T\,, \tag{4-23}$$

$$\underline{l}_{i,t}\le\sum_{j\in E} SF_{i,j}\cdot(p_{j,t}-d_{j,t})\le\overline{l}_{i,t} \quad \forall i\in L,\ t=1,\,2,\,\cdots T\,. \tag{4-24}$$

4.3.3 Heating System Constraints

In heat systems, the time interval is Δt in the identical model. The heat nodes constraints are:

$$h_{i,t} = c_p m^n_{i,t}(T^{NS}_{i,t} - T^{NR}_{i,t}) \quad \forall i \in H,\ t=1,\ 2,\ \cdots T\,. \tag{4-25}$$

In the heat supply network, for load nodes $T^{NS}_{i,t} = T^{S}_{i,t}$, and for source nodes $T^{S}_{i,t}$ is calculated by (4-30a), where $t=1,\ 2,\ \cdots T$. In the heat return network, for load nodes $T^{R}_{i,t}$ is calculated by (4-30b), and for source nodes $T^{NR}_{i,t} = T^{R}_{i,t}$, where $t=1,\ 2,\ \cdots T$.

The exchanger supply and return temperatures should satisfy:

$$\underline{T}_i^{NS} \le T^{NS}_{i,t} \le \overline{T}_i^{NS} \quad \forall i \in H,\ t=1,\ 2,\ \cdots T_H\,, \tag{4-26a}$$

$$\underline{T}_i^{NR} \le T^{NR}_{i,t} \le \overline{T}_i^{NR} \quad \forall i \in H,\ t=1,\ 2,\ \cdots T_H\,. \tag{4-26b}$$

Also, we have pipeline storage constraint (4-27) which is similar to (4-7):

$$\sum_{t \in T_H} \left(\sum_{i \in H/H_L} h_{i,t} - \sum_{i \in H_L} h_{i,t} \right) \Delta t \ge 0\,. \tag{4-27}$$

Moreover, additional equality constraints are added to ensure variables during each Δt_H are invariable:

$$h_{i,t} = h_{j,t} \quad \forall i \in H,\ t, j \in W_k,\ k=1,\ 2,\ \ldots T_H\,, \tag{4-28}$$

$$T^{NS}_{i,t} = T^{NS}_{i,j} \quad \forall i \in H,\ t, j \in W_k,\ k=1,\ 2,\ \ldots T_H\,, \tag{4-29a}$$

$$T^{NR}_{i,t} = T^{NR}_{i,j} \quad \forall i \in H,\ t, j \in W_k,\ k=1,\ 2,\ \ldots T_H\,, \tag{4-29b}$$

where W_k denotes the electric time sections included in the corresponding heat time section *k*. For example, if the heat time interval is 1 hour and the electric time interval is 15 minute, $W_1 = \{1,2,3,4\}$, $W_2 = \{5,6,7,8\}$, $W_3 = \{9,10,11,12\}$, etc. Constraints (4-28) and (4-29) denote the heat power and temperatures are invariable within each heat time interval.

The node temperature mixing equations are:

$$\begin{gathered} \left(m^n_{i\in H_G,t} + \sum_j m_{j,t} \right) T^S_{i,t} = \left(m^n_{i\in H_G,t} T^{NS}_{i\in H_G,t} \right) + \left(\sum_j m_{j,t} \tau^{SE}_{j,t} \right), \\ \forall i \in H,\ j \in P_S \bigcap In(i),\ t=1,\ 2,\ \cdots T_H \end{gathered} \tag{4-30a}$$

$$\begin{gathered} \left(m^n_{i\in H_L,t} + \sum_j m_{j,t} \right) T^R_{i,t} = \left(m^n_{i\in H_L,t} T^{NR}_{i\in H_L,t} \right) + \left(\sum_j m_{j,t} \tau^{RE}_{j,t} \right). \\ \forall i \in H,\ j \in P_R \bigcap In(i),\ t=1,\ 2,\ \cdots T_H \end{gathered} \tag{4-30b}$$

The equality constraints are added to (4-30) to satisfy the heat adjustment time scale:

$$T_{i,t}^{S}=T_{i,j}^{S} \quad \forall i\in H,\ t,j\in W_k,\ k=1,\ 2,\ \ldots T_H\,, \tag{4-31a}$$

$$T_{i,t}^{R}=T_{i,j}^{R} \quad \forall i\in H,\ t,j\in W_k,\ k=1,\ 2,\ \ldots T_H\,, \tag{4-31b}$$

$$\tau_{i,t}^{SE}=\tau_{i,j}^{SE} \quad \forall i\in P_S,\ t,j\in W_k,\ k=1,\ 2,\ \ldots T_H\,, \tag{4-32a}$$

$$\tau_{i,t}^{RE}=\tau_{i,j}^{RE} \quad \forall i\in P_R,\ t,j\in W_k,\ k=1,\ 2,\ \ldots T_H\,. \tag{4-32b}$$

The pipe initial temperature equals to the temperature of its connecting node:

$$\tau_{j,t}^{SI}=T_{i,t}^{S} \quad j\in P_S\bigcap Lv(i),\ \ i\in H,\ t=1,2,\cdots T\,, \tag{4-33a}$$

$$\tau_{j,t}^{RI}=T_{i,t}^{R} \quad j\in P_R\bigcap Lv(i),\ \ i\in H,\ t=1,2,\cdots T\,. \tag{4-33b}$$

And the additional constraints with (4-33) are:

$$\tau_{i,t}^{SI}=\tau_{i,j}^{SI} \quad \forall i\in P_S,\ t,j\in W_k,\ k=1,\ 2,\ \ldots T_H\,, \tag{4-34a}$$

$$\tau_{i,t}^{RI}=\tau_{i,j}^{RI} \quad \forall i\in P_R,\ t,j\in W_k,\ k=1,\ 2,\ \ldots T_H\,. \tag{4-34b}$$

The pipeline model includes:

$$\tau_{i,t}^{\prime SE}=\sum_{k=t-\varphi_{i,t}}^{t-\gamma_{i,t}} K_{i,t,k}\tau_{i,k}^{SI} \quad \forall i\in P_S,\ t=1,2,\cdots T\,, \tag{4-35a}$$

$$\tau_{i,t}^{\prime RE}=\sum_{k=t-\varphi_{i,t}}^{t-\gamma_{i,t}} K_{i,t,k}\tau_{i,k}^{RI} \quad \forall i\in P_R,\ t=1,2,\cdots T\,, \tag{4-35b}$$

$$\begin{aligned}\tau_{i,t}^{SE}&=T_{i,t}^{a}+(\tau_{i,t}^{\prime SE}-T_{i,t}^{a})\times\exp\left[-\frac{\lambda_i\Delta t}{A_i\rho c_p}\left(\gamma_{i,t}+\frac{1}{2}+\frac{S_{i,t}-R_{i,t}}{m_{i,t-\gamma_{i,t}}\Delta t}\right)\right],\\ &\forall i\in P_S,\ t=1,2,\cdots T\end{aligned} \tag{4-36a}$$

$$\begin{aligned}\tau_{i,t}^{RE}&=T_{i,t}^{a}+(\tau_{i,t}^{\prime SE}-T_{i,t}^{a})\times\exp\left[-\frac{\lambda_i\Delta t}{A_i\rho c_p}\left(\gamma_{i,t}+\frac{1}{2}+\frac{S_{i,t}-R_{i,t}}{m_{i,t-\gamma_{i,t}}\Delta t_H}\right)\right],\\ &\forall i\in P_R,\ t=1,2,\cdots T\end{aligned} \tag{4-36b}$$

where $K_{i,t,k}$, $\varphi_{i,t}$, $\gamma_{i,t}$, $S_{i,t}$, and $R_{i,t}$ are calculated according to (4-11)-(4-13).

4.3.4 Energy Sources Constraints

4.3.4.1 Combined Heat and Power Units

In the identical time scale model, the CHP constraints are:

$$B_{k,i} p_{i,t} + K_{k,i} h_{i,t} \le v_{k,i} \quad \forall i \in G,\ t=1,2,\cdots T, \tag{4-37a}$$

$$B_{k,i} p_{i,t} + K_{k,i} h_{i,t} = v_{k,i} \quad \forall i \in G,\ t=1,2,\cdots T. \tag{4-37b}$$

The ramping constraints of CHP units are:

$$D_{e,i} \cdot \Delta t \le p_{i,t} - p_{i,t-1} \le U_{e,i} \cdot \Delta t \quad \forall i \in G,\ t=1,2,\cdots T, \tag{4-38}$$

$$D_{h,i} \cdot \Delta t \le h_{i,t} - h_{i,t-1} \le U_{h,i} \cdot \Delta t \quad \forall i \in G,\ t=1,2,\cdots T. \tag{4-39}$$

Moreover, the CHP unit’s supply temperature satisfies:

$$T_{j,t}^{NS} = T_{i,t}^{Set} \quad \forall i \in G,\ j=\Gamma_G(i),\ t=1,2,\cdots T_H. \tag{4-40}$$

4.3.4.2 Thermal Generator and Main Grid

The power output of the thermal generator and the main grid at energy source *i* is:

$$\underline{p}_{i,t} \le p_{i,t} \le \overline{p}_{i,t} \quad \forall i \in G,\ t=1,2,\cdots T, \tag{4-41}$$

And the ramping constraint of the thermal generator follows constraint (4-38).

4.4 Case Studies

In the case studies, the following questions will be answered: 1) Do the two proposed asynchronous economic dispatch models have the same results? 2) Does the heat dispatch interval influence the results? 3) Is it necessary to use asynchronous dispatch considering we already have the traditional synchronous dispatch method?

The simulations are based on the combined heat and power system in Figure 4-3 (a) [36], where the test system has a 6-node electric power system and a 6-node heat system with a CHP unit and a thermal unit. The electric power system can purchase electricity from the main grid through the tie-line. The sums of electric load and heat load are shown in the orange and blue curves in Figure 4-3 (b), respectively, where the load at node (bus) 3 is the residential load and the loads at other nodes (buses) are industrial loads. The adjustment time scales of the electric power system and the heating system are 15 minutes and 60 minutes, respectively.

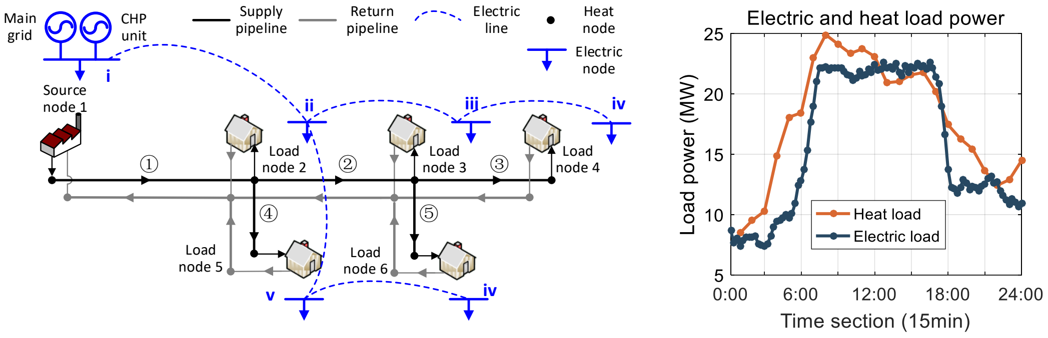

(a) (b)

Figure 4-3. The (a) topology of combined heat and power system for asynchronous economic dispatch and (b) electric and heat load power.

4.4.1 Case 1: Comparison of the Two Asynchronous Economic Dispatch Models

This simulation answers question 1: whether the hybrid model and the identical model have the same results. In the hybrid model, $\Delta t_E = 15\,\text{min}$ and $\Delta t_H = 60\,\text{min}$; In the identical mode, $\Delta t = 15\,\text{min}$ with additional equality constraints to guarantee during each $\Delta t_H = 60\,\text{min}$ heat variables are invariable.

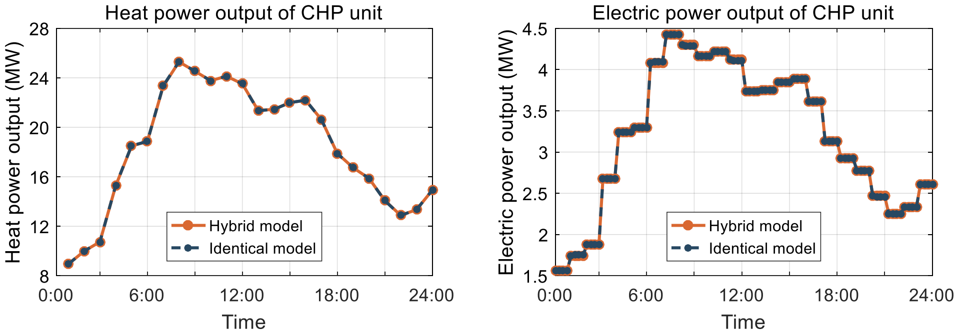

(a) (b)

Figure 4-4. The (a) electric power and (b) heat power outputs of CHP unit in the hybrid model and identical model.

Obviously, from the results shown from Figure 4-4 to 4-6, the hybrid model and the identical model have the same results. This phenomenon is more apparent in Figure 4-6, where temperatures at heat node 6 of the two models have no difference. The reason is that the additional equality constraints in the identical model ensure the heat variables equal to each other during each Δt_H, which has an equivalent effect as the hybrid model.

In Figure 4-4, as the only heat source, the CHP unit adjusts the electric and heat power outputs every 60 minutes even if it has the ability to adjust electric power every

15 minutes. This is caused by the linear relationship between electric and heat power outputs: the slow adjustment of heat power limits the fast adjustment ability of electric power. As a result, the fast-changing electric load is satisfied by the thermal generator and the main grid in Figure 4-5. This result illustrates in a combined heat and power system, although an electric-heat coupling device (here is the CHP unit) has the fast adjustment ability for the electric variables, the slow adjustment of heat variables will restrict its fast adjustment ability. Therefore, additional flexible electric sources are needed to maintain the electric supply-demand balance even if the capacities of electric-heat coupling devices are enough for the electric load.

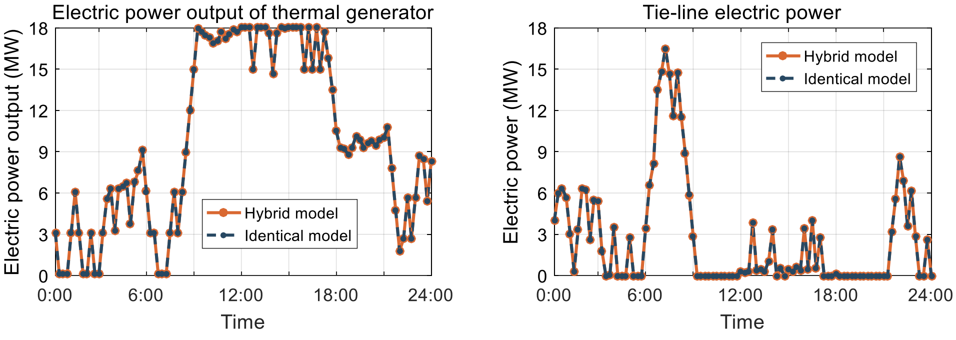

(a) (b)

Figure 4-5. The electric power (a) of thermal generator and (b) bought from the main grid.

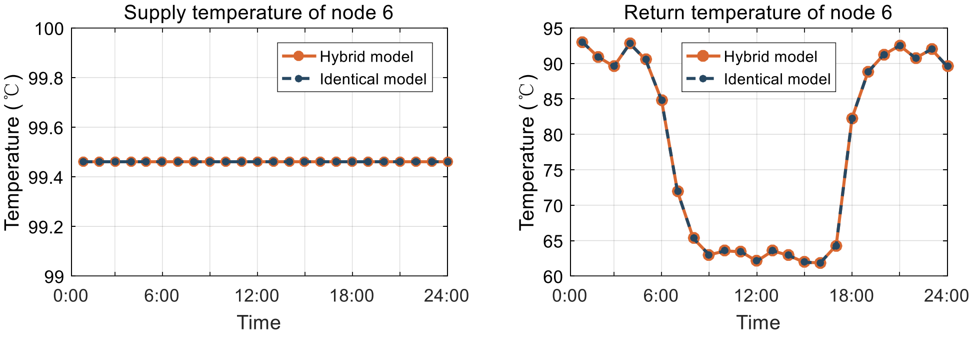

(a) (b)

Figure 4-6. The node exchanger (a) supply temperature and (b) return temperature of node 6 in heating system.

4.4.2 Case 2: Performance under Different Dispatch Interval

This case is carried out to answer question 2: How can the heat dispatch interval Δt_H influence the results of the asynchronous economic dispatch.

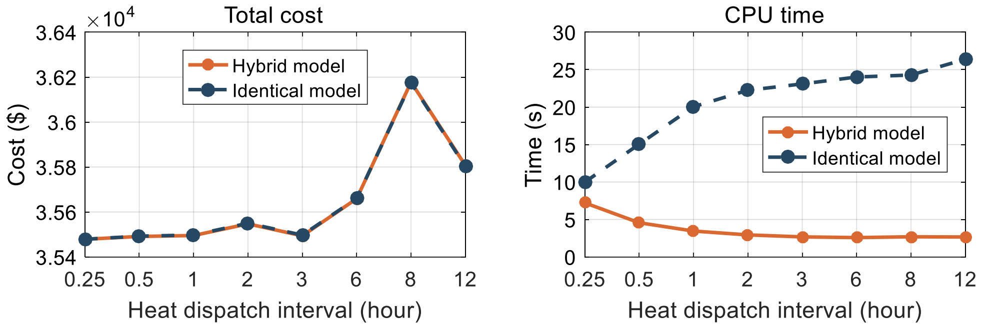

(a) (b)

Figure 4-7. The (a) total generation cost and (b) CPU time of calculation under different Δt_H .

As shown in Figure 4-7 (a), when increasing the heat dispatch interval Δt_H , the total generation cost has experienced a slight increase (<2%) because the adjustment flexibilities of CHP units and the heating network are restricted by the increasing heating adjustment time scale. As special cases, the total costs do not increase significantly at $\Delta t_H = 3\,\text{hour}$ and $\Delta t_H = 12\,\text{hour}$ since the heat power within Δt_H may not be satisfied.

Obviously, in Figure 4-7 (b) the CPU time of solving the hybrid model is much less than the identical model. With Δt_H increasing, the CPU time of the hybrid model is decreasing, while that of the identical model is increasing as a result of constraint numbers: Since the total dispatch time is the same, i.e., 24 hours when heat dispatch interval Δt_H is longer, there are less heating constraints in the hybrid model but more constraints in the identical model as a result of adding more additional equality constraints like (4-28). Thus, when Δt_H becomes longer, the computational efficiency of the hybrid model goes higher but that of the identical model goes lower.

Moreover, this case simulation can serve as a supplemental answer for question 1: under different Δt_H , the hybrid model has the same results as the identical model. For example, in Figure 4-8, the result of the node exchanger temperature at heat node 6 clearly demonstrates that the temperatures calculated by the two models are the same even adjusting the *y*-axis to very high precision.

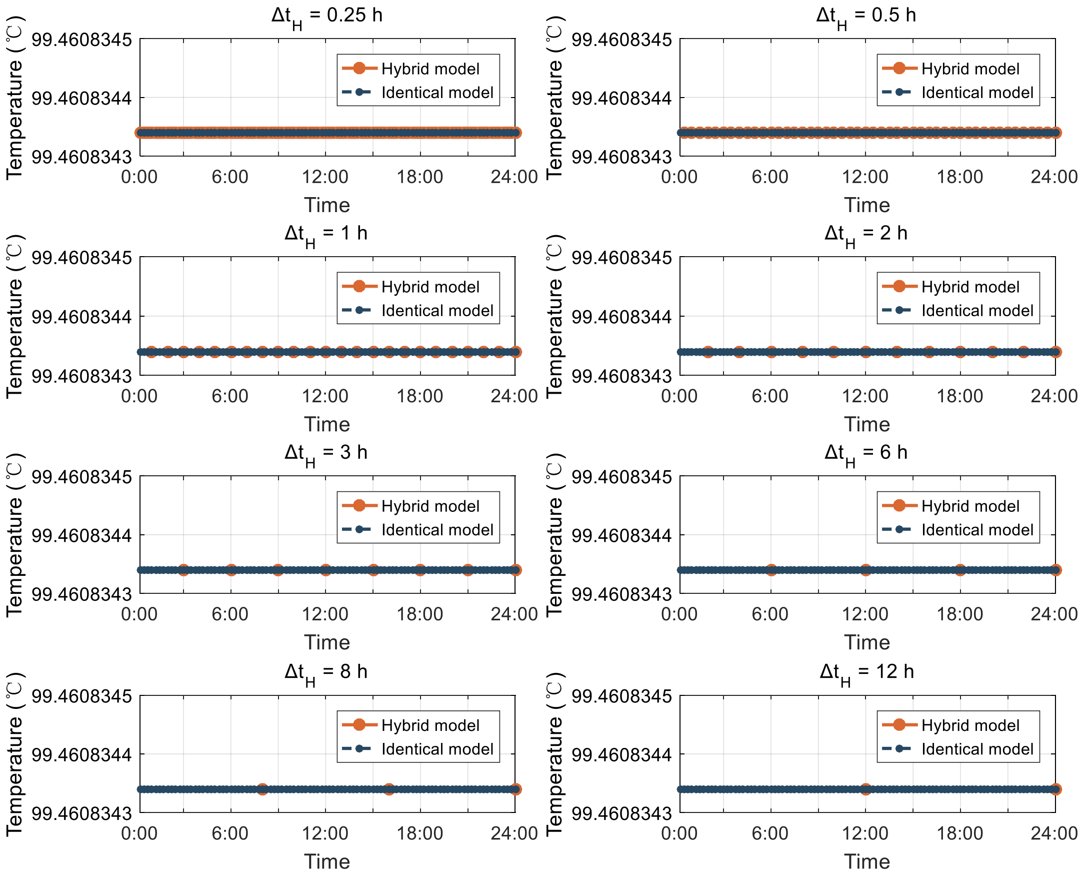

Figure 4-8. The node exchanger supply temperature of node 6 in heating system.

4.4.3 Case 3: Necessity of Using Asynchronous Dispatch

For question 3, two cases are simulated to demonstrate the necessity of using the asynchronous dispatch method rather than the traditional synchronous dispatch method ignoring the different adjustment time scales of electricity and heat. Since the adjustment time scales of the electric power system and the heating system are 15 minutes and 60 minutes, respectively, if a new dispatch command is not 15 minutes later in the electric power system and 60 minutes later in the heating system than the last dispatch command, it cannot be executed in practice.

4.4.3.1 Comparison to Traditional Dispatch with Heat Time scale

Here the synchronous dispatch following the adjustment time scale $\Delta t = 60\,\text{min}$ is compared with the asynchronous dispatch with $\Delta t_E = 15\,\text{min}$ and $\Delta t_H = 60\,\text{min}$. For clarity, the key given conditions and results are summarized in Table 4-1:

Table 4-1 Comparison of asynchronous method and synchronous method with $\Delta t = 60\,\text{min}$

Methods	Asynchronous method	Synchronous method
Electric command interval (min)	15	60
Heat command interval (min)	60	60
Total electric load (MWh)	379.4	379.4
Total electric generation (MWh)	379.4	378.8
Total electric unbalanced energy (MWh)	0	14.3
Total heat load (MWh)	429.8	429.8
Total heat generation (MWh)	431.7	431.7

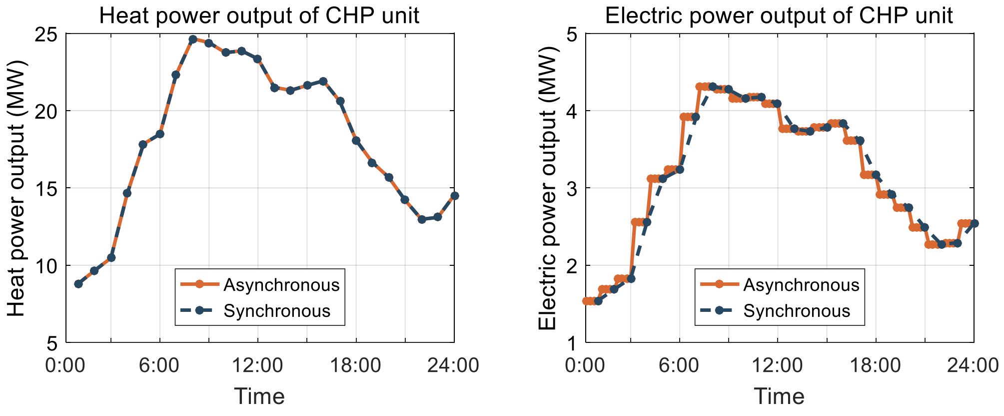

(a) (b)

Figure 4-9. The (a) electric power and (b) heat power outputs of CHP unit in asynchronous dispatch (asynchronous) and synchronous dispatch (synchronous).

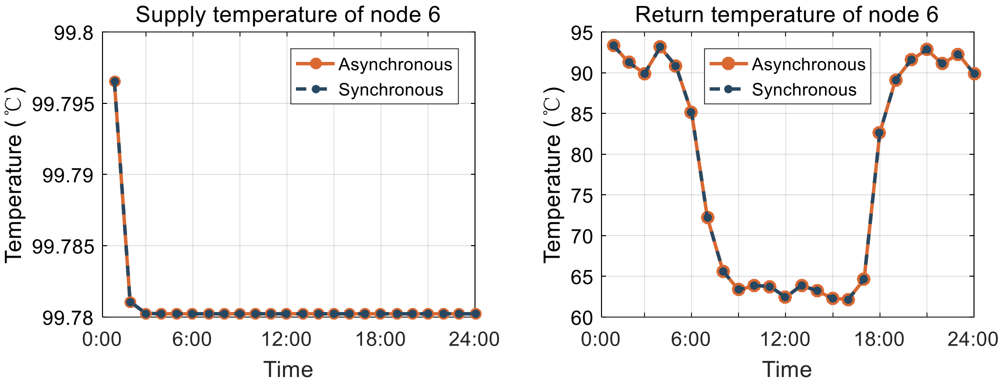

(a) (b)

Figure 4-10. The node exchanger (a) supply temperature and (b) return temperature of node 6 in heating system.

Under the above conditions, the two dispatch methods all find the global optimum and satisfy the heat load successfully. For example, heat power output and temperatures have the same results as presented in Figures 4-9 and 4-10, respectively.

However, as shown in Figure 4-11 (a) and Table 4-1, the synchronous dispatch fails to satisfy electric load: The power balance between the generation side and load side is not satisfied for 18 hours in a day, and the total unbalanced electric energy is 14.3MWh as presented in the grey block of Table 4-1. By calculating the power unbalance rate between the generation side and the load side according to $r_{i,t} = (p_{i,t} - d_{i,t}) / d_{i,t} \times 100\%$ and plotting it in Figure 4-11 (b), we find that the traditional method seriously threatens the security of electric power system operation. For example, at 17:15, about 35% of electric load power is not satisfied, and at 3:15, 5:15, and 6:15, the system has about 30% generation surplus. The reason for the synchronous dispatch's failure is that the dispatch interval Δt is too large that the electric load within Δt cannot be satisfied. Thus, in the synchronous dispatch model, selecting the dispatch interval Δt based on the heat adjustment time scale can lead to the violation of the electric generation-load power balance, which threatens the security of the electric power system. In contrast, the proposed asynchronous method can satisfy both electric and heat demands successfully without any violation as shown in the orange curve in Figure 4-11.

In brief, it is not secure to dispatch the combined heat and power system using the synchronous method with the heat adjustment time scale.

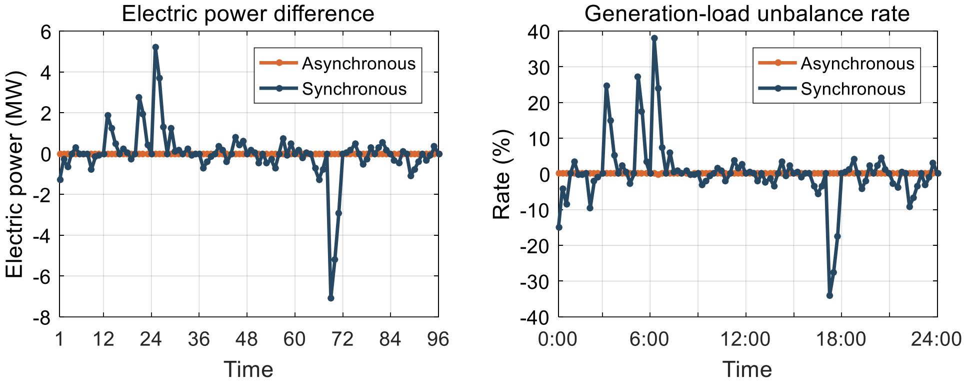

(a) (b)

Figure 4-11. The (a) electric power difference and (b) electric power unbalance rate between generation side and load side.

4.4.3.1 Comparison to Traditional Dispatch with Electric Time Scale

To address the electric power system security problem in the above case, the synchronous dispatch following the adjustment time scale $\Delta t = 15\,\text{min}$ is compared with the asynchronous dispatch with $\Delta t_E = 15\,\text{min}$ and $\Delta t_H = 60\,\text{min}$.

Under the given condition, practically the heating system cannot execute all but a part of dispatch commands due to its long adjustment time scale. Therefore, in Figure 4-12, there are three curves named Asynchronous, Synchronous (ideal), and Synchronous (practical) which are the abbreviations of the asynchronous method, synchronous method adjusting heating system every 15 minutes, and synchronous method's adjustment in practice. In Table 4-2, both asynchronous dispatch and the synchronous dispatch (ideal) find the global optimums, while the synchronous dispatch (practical) is an infeasible problem.

Table 4-2 Comparison of asynchronous method and synchronous method with $\Delta t = 15\,\text{min}$

Methods	Asynchronous method	Synchronous method (ideal)	Synchronous method (practical)
Electric command interval (min)	15	15	15
Heat command interval (min)	60	15	60
Successfully solved	Yes	Yes	No

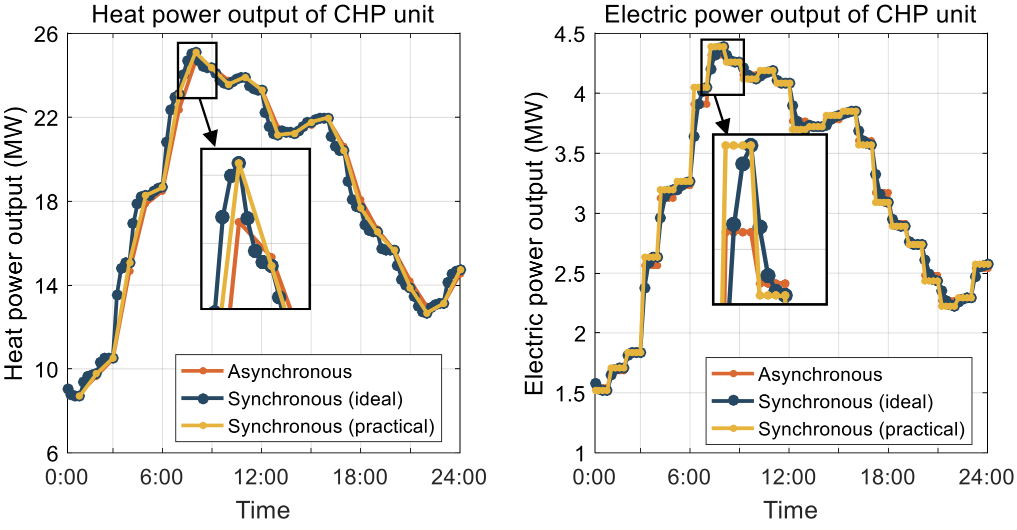

(a) (b)

Figure 4-12. The (a) electric power and (b) heat power outputs of CHP unit.

To study the results of the synchronous dispatch (practical) if some constraints are allowed to be violated, in this case we slack heat exchanger temperature limits and the CHP temperature constraints. After that, the optimization problem can be successfully solved, whose temperatures are marked as "Synchronous (slacked practical)" in the yellow curves with blocks in Figure 4-13. From Figure 4-13, if the results of the synchronous dispatch are implemented in practice without the consideration of temperature constraints, the heat exchanger supply temperature is approaching 120℃ as shown in Figure 4-13 (a), which indicates the hot water becomes steam. As a result, the heat exchanger will not work as a normal state and probably have serious security problems.

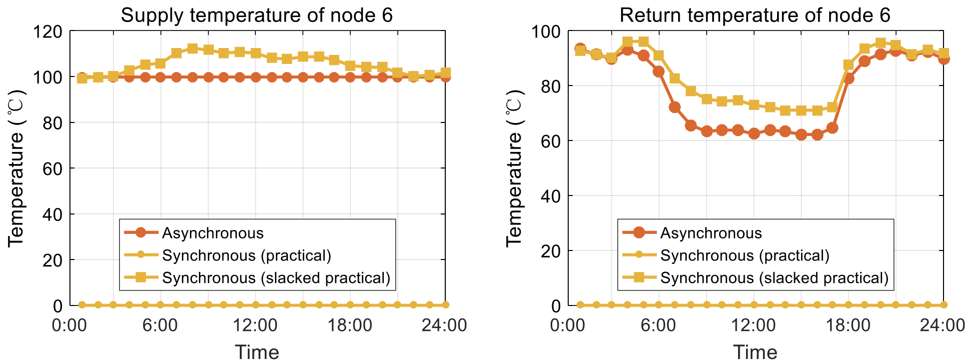

(a) (b)

Figure 4-13. The node exchanger (a) supply temperature and (b) return temperature of node 6 in heating system.

In contrast, as shown in the blue curve in Figure 4-13, the economic dispatch based on the asynchronous dispatch method can be successfully solved and implemented in practice with all constraints satisfied because different adjustment time scales of the electric power system and the heating system are incorporated.

In brief, the synchronous method based on the electric time scale is infeasible to be executed practically if the two energy systems have different adjustment time scales, but this problem can be overcome by the proposed asynchronous method.

4.5 Conclusion

In this chapter, two asynchronous economic dispatch models, i.e., hybrid mode and identical model, are proposed for combined heat and power systems, which incorporate different adjustment time scale of electricity and heat and have the same results. From the comparisons of case studies, if the electricity and heat have different adjustment time scales, the traditional synchronous dispatch method will either have security problems in the electric power system or become infeasible to implement practically. Therefore, it is essential to adopt asynchronous dispatch when the electric power system and the heating system have different adjustment time scales. In the asynchronous dispatch, with the heat dispatch interval increasing, the efficiency of the hybrid model is increasing while that of the identical model is decreasing, but the results of variables in the two models hold the same.

Chapter 5: Distributed Optimal Frequency Control

5.1 Overview

As presented in Figure 5-1, when there are prediction errors and uncertainties, the real-time electric and heat load powers will have disturbances around the values in the economic dispatch in Chapter 3 and 4. Thus, the secondary frequency control is needed to restore the frequency by adjusting the generation power and eliminating the power mismatch between generation and load sides.

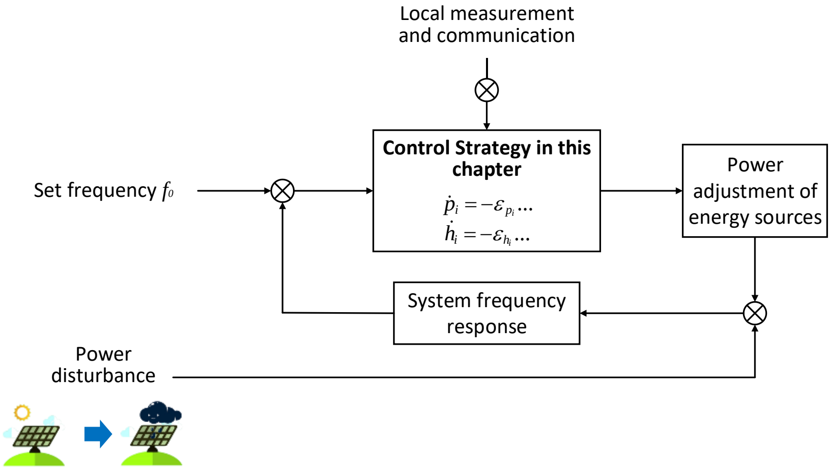

Figure 5-1. The control block of the proposed distributed frequency control.

In this chapter, a distributed frequency control method is proposed with system-wide optimality, which is used for the secondary control (AGC) of combined heat and power systems. Compared with traditional AGC methods, the proposed method is an economic AGC whose power adjustments are system-wide optimal. So the proposed frequency control method is called “optimal frequency control”.

The contributions of the proposed model and the solution method are:

1) The fully-distributed frequency control manner is proposed with system-wide optimality and globally asymptotically stable.
2) The electric-heat coupling device model is considered in the frequency control to prevent the violation of the generator’s feasible region of electric and heat outputs.
3) The electric line power constraints and flexibility from the heating system are considered in the control model.

4) The proposed solution method is robust to inaccurate damping coefficients and does not need the measurement of the phase angle.

For clarity, the process of designing the optimal frequency control strategy is presented in Figure 5-2, where the optimal control models are detailed in Section 5.3 and the distributed solution method is designed in Section 5.4.

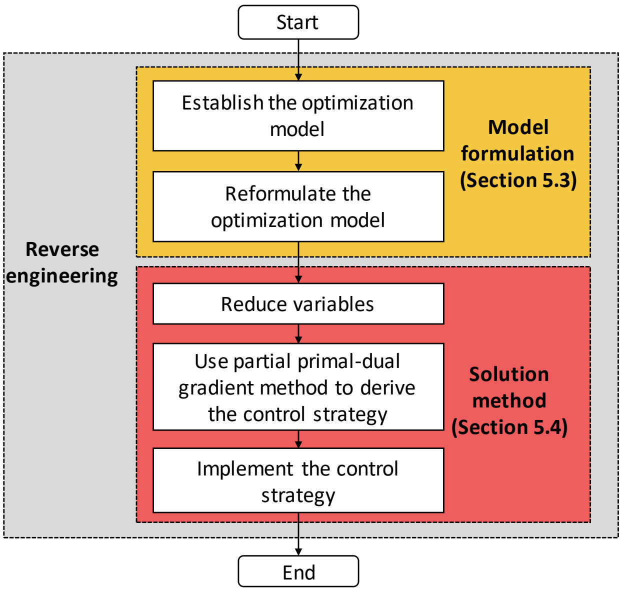

Figure 5-2. The flow chart of designing frequency control strategy in this chapter.

5.2 Physical Model

In this section, preliminaries are firstly presented to describe the topology of combined heat and power systems, and then the network model is developed to describe the physical control model. It is noticed that the method in this chapter is most applicable to the combined heat and power system in the microgrid scale.

5.2.1 Preliminaries

In the optimal frequency control of combined heat and power systems, a heat node is assumed to link to an electric bus, and the heat network is not considered because the frequency control is in seconds or milliseconds. Thus, the heating system can be described by the topology of the electric power system, which is described as a directed graph $\Lambda=(E,L_s)$, where $E=\{1,2,3,...,n\}$ denotes the set of electric buses, and $L_s=E\times E$ is the set of single-direction power lines. The buses generate or consume electricity and heat, and the electricity is transmitted through power lines. The buses are divided into two sets: generator bus set E_G and load bus set E_{LD} with $E = E_G \bigcup E_{LD}$. The generator buses contain generators and may contain attached loads, but the load buses only contain loads. We define $C \in |E| \times |L_s|$ as the incidence matrix of the graph $\Lambda = (E, L_s)$ where $C_{i,l} = 1$ if $l = ij \in L_s$, $C_{i,l} = -1$ if $l = ji \in L_s$, and $C = 0$ otherwise.

5.2.2 Network Model

Based on the DC power flow model, the electric line power flow P_{ij} can be calculated by:

$$P_{ij} = \tilde{B}_{ij}(\theta_i - \theta_j) \quad i, j \in E,\ ij \in L_s, \tag{5-1}$$

where $\tilde{B}_{ij}$ is a coefficient related to the voltage magnitudes at buses *i* and *j*. For simplicity, all variables such as $P_{ij}, \theta_i, \theta_j$ in this chapter are defined as the deviations from their nominal values P_{ij}^0, θ_i^0, θ_j^0 which are calculated by economic dispatch.

Consider the dynamic network model of a combined heat and power system in Figure 5-3 with the electric power system (in blue) and the heating system (in red) [79]:

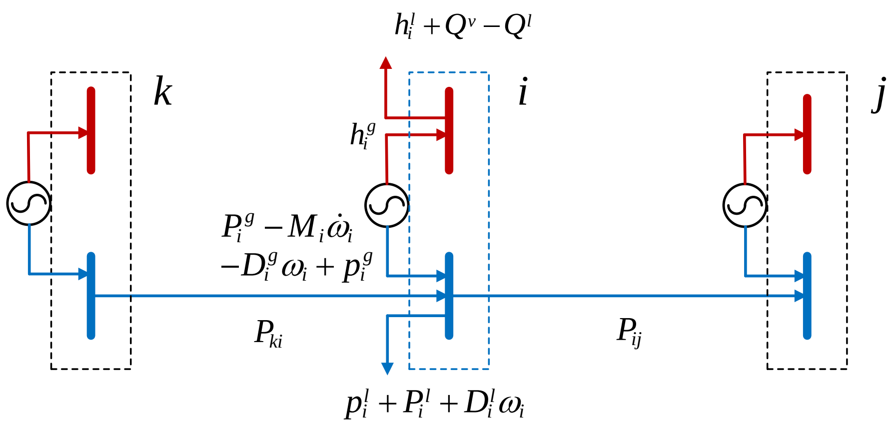

Figure 5-3. Dynamics of network model at bus *i*

Scalar ω_i is the per-unit frequency derivation of bus *i*, which indicates $\omega_i = (\omega_i^{real} - \omega_0) / \omega_0$, where ω_i^{real} is the real value of the frequency and ω_0 indicates the nominal frequency, i.e., 50Hz or 60Hz. Scalars p_i and h_i are the controllable electric and heat outputs, in which $p_i = p_i^l - p_i^g$ and $h_i = h_i^l - h_i^g$. Scalar M_i denotes the generator inertia at bus *i*, and the aggregated uncontrollable power injection P_i^{in} is the difference of the uncontrollable generator power output P_i^g and the load power P_i^l, i.e., $P_i^{in} = P_i^g - P_i^l$, and the uncontrollable heat power injection Q_i^{in} is the uncontrollable load power $-Q_i^l$, i.e., $Q_i^{in}=-Q_i^l$. Damping coefficient D_i is the sum of the generator and load damping coefficients denoted by D_i^g and D_i^l respectively, i.e., $D_i=D_i^g+D_i^l$. Since the time scale of the optimal control command is less than 1 second, the building and network heat inertia is considered:

$$Q_i^{in}-h_i=Q_i^v \quad i\in E\,, \tag{5-2}$$

where Q_i^v is the heat inertia which is limited by the lower boundary $\underline{Q}_i^v$ and the upper boundary $\bar{Q}_i^v$. By introducing Q_i^v, small mismatch of heat power can be compensated by its heat inertia, which makes use of the flexibility of the heating system for the electric frequency control. In the practice, Q_i^v can be estimated by the operator according to the building area and outdoor temperature.

Electricity and heat are coupled via electric-heat coupling devices, which are modeled as the CHP unit whose feasible region is a polytope [27]. Here two inequality constraints which describe the feasible region of CHP units are used to divide a united constraint (4-16) in Chapter 4 into upper and lower boundary constraints:

$$h_i\le\frac{B_{k,i}}{K_{k,i}}p_i+\frac{v_{k,i}}{K_{k,i}} \quad \forall k\in K_+,\ i\in E_G\,,$$

$$h_i\ge\frac{B_{n,i}}{K_{n,i}}p_i+\frac{v_{n,i}}{K_{n,i}} \quad \forall n\in K_-,\ i\in E_G\,,$$

where K_+ and K_- are sets of upper and lower boundaries, respectively.

To derive the electric network dynamics, consider the swing equation:

$$\dot{\theta}_i=\omega_i \quad \forall i\in E\,,$$

$$M_i\dot{\omega}_i=\left(\breve{P}_{i,m}-\breve{P}_{i,e}\right)-D\omega_i \quad \forall i\in E_G\,,$$

where $\breve{P}_{i,m}$ and $\breve{P}_{i,e}$ are mechanical power and electromagnetic power of the generator at bus *i*, respectively. It is noticed that $\omega_i=(\omega_i^{real}-\omega_0)/\omega_0$. Based on the swing equation, defining $P^e=CP$, where $P=\left\{P_{ij}\right\}_{i\in E}$ as the leaving line power from bus *i*, electric network dynamics can be derived by changing $\breve{P}_{i,m}$ and $\breve{P}_{i,e}$ with the variables in Figure 5-3 [55][56]:

$$M_i\dot{\omega}_i=P_i^{in}-p_i-D_i\omega_i-P_i^e \quad i\in E_G\,, \tag{5-3}$$

$$0=P_i^{in}-p_i-D_i\omega_i-P_i^e \quad i\in E_{Ld}\,, \tag{5-4}$$

$$\dot{P}_{ij}=\tilde{B}_{ij}(\omega_i-\omega_j) \quad i,j\in E,\ ij\in L_s \tag{5-5}$$

where (5-3) and (5-4) represent the dynamics of generator buses and load buses. Equation (5-5) reflects electric line power flow dynamics under the assumption of small frequency deviations.

Remark 5-1**:** Practically, the uncontrollable electric power injection P_i^{in} and damping coefficient D_i are difficult to measure accurately [56]. However, if we use these inaccurate variables in the control, the errors may lead to frequency instability. Innovatively, the proposed method does not need the measurement of P_i^{in} and is robust to the inaccurate coefficient D_i, which will be strictly proved in Theorem 5-3.

5.3 Optimal Control Model

The steady state of the combined heat and power system is provided by economic dispatch in Chapters 3 and 4, which means equations (5-3)-(5-5) are adopted around an equilibrium with $\dot{\omega}_i = 0$ and $\dot{P}_{ij} = 0$. If the disturbance reflected by any step change of P_i^{in} or Q_i^{in} occurs in the combined heat and power systems, the goal of the frequency control is to

1) Restore frequency to the nominal value i.e. 50Hz or 60Hz;
2) Rebalance system electric and heat power outputs and let each control area absorb its power imbalance;
3) Achieve minimal cost under electric and heat operating constraints.

To realize the goal 2 and 3, the optimization problem (5-6) is formulated:

$$\min_{p,h,\theta} f = \sum_{i \in E} C_{i,e}(p_i) + C_{i,h}(h_i), \tag{5-6a}$$

$$\text{s.t.} \quad P_i^{in} - p_i - \sum_{j:ij \in L_{s,in}} \tilde{B}_{ij}(\theta_i - \theta_j) + \sum_{k:ki \in L_{s,in}} \tilde{B}_{ki}(\theta_k - \theta_i) = 0 \quad i \in E, \tag{5-6b}$$

$$h_i - Q_i^{in} = Q_i^v \quad i \in E, \tag{5-6c}$$

$$h_i \le \frac{B_{k,i}}{K_{k,i}} p_i + \frac{v_{k,i}}{K_{k,i}} \quad \forall k \in K_+,\ i \in E_G, \tag{5-6d}$$

$$h_i \ge \frac{B_{n,i}}{K_{n,i}} p_i + \frac{v_{n,i}}{K_{n,i}} \quad \forall n \in K_-,\ i \in E_G, \tag{5-6e}$$

$$\underline{Q}_i^v \le Q_i^v \le \overline{Q}_i^v \quad i \in E, \tag{5-6f}$$

$$\underline{p}_i \le p_i \le \overline{p}_i \quad i \in E, \tag{5-6g}$$

$$\underline{P}_{ij} \le B_{ij}(\theta_i - \theta_j) \le \overline{P}_{ij} \quad i, j \in E,\ ij \in L_s\ , \tag{5-6h}$$

where $\underline{p}_i$ and $\overline{p}_i$ are lower and upper limits of the electric power generation. Scalars $\underline{P}_{ij}$ and $\overline{P}_{ij}$ are lower and upper limits of the electric line power, respectively. Set $L_{s,in}$ is the subset of lines that connect buses within the same control area.

The (5-6a) is the objective function aiming to minimize the cost of electric and heat power adjustments. (5-6b) ensures that power imbalance is eliminated by adjusting the power within each control area and maintaining the power of the inter-area line. (5-6c) is the heat power balance. (5-6d) and (5-6e) are electric and heat power limit of CHP units. (5-6e)-(5-6h) are the limits of heat inertia, controllable load, and line power flow. For optimality and convergence analysis, the assumptions are:

***Assumption 5-1*:** The cost functions $C_{i,e}(p_i)$ and $C_{i,h}(h_i)$ are strictly convex and continuously differentiable with $C''_{i,e}(p_i) \ge \alpha_e > 0$, and $C''_{i,h}(h_i) \ge \alpha_h > 0$.

***Assumption 5-2*:** The Problem (5-6) is feasible.

Since the problem (5-6) ignores the goal of restoring system frequency and needs the measurement of bus phase angle, the reformulated problem (5-7) is developed:

$$\min_{\omega, p, h, P, \varphi} f = \sum_{i \in E} [C_{i,e}(p_i) + C_{i,h}(h_i)] + \sum_{i \in N} \frac{1}{2} k_i^D D_i \omega_i^2\ , \tag{5-7a}$$

$$\text{s.t.} \qquad P_i^{in} - p_i - D_i \omega_i - \sum_{j:ij \in L_s} P_{ij} + \sum_{k:ki \in L_s} P_{ki} = 0 \quad i \in E\ , \tag{5-7b}$$

$$P_i^{in} - p_i - D_i \omega_i - \sum_{j:ij \in L_{s,in}} B_{ij}(\varphi_i - \varphi_j) + \sum_{k:ki \in L_{s,in}} B_{ki}(\varphi_k - \varphi_i) = 0 \quad i \in E\ , \tag{5-7c}$$

$$h_i \le \frac{B_{k,i}}{K_{k,i}} p_i + \frac{v_{k,i}}{K_{k,i}} \quad \forall k \in K_+,\ i \in E_G\ , \tag{5-7d}$$

$$h_i \ge \frac{B_{n,i}}{K_{n,i}} p_i + \frac{v_{n,i}}{K_{n,i}} \quad \forall n \in K_-,\ i \in E_G\ , \tag{5-7e}$$

$$\underline{p}_i \le p_i \le \overline{p}_i \quad i \in E\ , \tag{5-7f}$$

$$\underline{Q}_i^v \le Q_i^v \le \overline{Q}_i^v \quad i \in E\ , \tag{5-7g}$$

$$\underline{P}_{ij} \le B_{ij}(\varphi_i - \varphi_j) \le \overline{P}_{ij} \quad i, j \in E,\ ij \in L_s\ , \tag{5-7h}$$

where φ_i is the virtual phase angle [55] to eliminate the measurement of the real phase angle θ_i . Scalar k_i^D is a penalty coefficient, whose value is 1 in this chapter. Equation

(5-7a) is the reformulated objective function which adds the penalty term of restoring frequency, and (5-7b) is a redundant equation for algorithm design.

Theorem 5-1**:** Let $(\omega^*, p^*, h^*, P^*, \varphi^*)$ become an optimum of the problem (5-7). When $\omega_i^* = 0$ is satisfied for $\forall i \in E$, the p^* and h^* are optimal for the problem (5-6).

5.4 Distributed Solution Method

In this section, a fully-distributed algorithm is designed to solve the reformulated problem (5-7) based on reverse engineering. To make it clear, the derivation of the solution method is divided into three steps: 1) derive Lagrangian function; 2) apply partial primal-dual gradient method to construct a distributed control scheme; 3) propose the implementation framework of the scheme.

5.4.1 Lagrangian Function Derivation

From the reformulated problem (5-7), the Lagrangian function is derived:

$$\begin{aligned}
L = & \sum_{i \in E} C_{i,e}(p_i) + C_{i,h}(h_i) + \sum_{i \in E} \frac{1}{2} D_i \omega_i^2 + \sum_{i \in E} \lambda_i (P_i^{in} - p_i - D_i \omega_i - \sum_{j:ij \in L_s} P_{ij} + \sum_{k:ki \in L_s} P_{ki}) \\
& + \sum_{i \in E} \mu_i [P_i^{in} - p_i - \sum_{j:ij \in L_{s,in}} B_{ij}(\varphi_i - \varphi_j) + \sum_{k:ki \in L_{s,in}} B_{ki}(\varphi_k - \varphi_i)] \\
& + \sum_{m \in K^+} \sum_{i \in E} \zeta_i^m \left(h_i - \frac{B_{m,i}}{K_{m,i}} p_i - \frac{\nu_{m,i}}{K_{m,i}} \right) - \sum_{n \in K^-} \sum_{i \in E} \zeta_i^n \left(h_i - \frac{B_{n,i}}{K_{n,i}} p_i - \frac{\nu_{n,i}}{K_{n,i}} \right) \\
& + \sum_{i \in E} \gamma_i^+ \left(p_i - \underline{p}_i \right) - \sum_{i \in E} \gamma_i^- \left(p_i - \bar{p}_i \right) + \sum_{i \in E} \delta_i^+ \left(-h_i + Q_i^{in} - \bar{Q}_i^v \right) + \sum_{i \in E} \delta_i^- \left(h_i - Q_i^{in} + \underline{Q}_i^v \right) \\
& + \sum_{i \in E, ij \in L_s} \sigma_{ij}^+ [\tilde{B}_{ij}(\varphi_i - \varphi_j) - \underline{P}_{ij}] - \sum_{i \in E, ij \in L_s} \sigma_{ij}^- [\tilde{B}_{ij}(\varphi_i - \varphi_j) - \bar{P}_{ij}],
\end{aligned} \tag{5-8}$$

where the λ, μ, γ, ζ, γ, δ, σ indicate the dual variables for corresponding constraints.

5.4.2 Partial Primal-Dual Gradient Method Application

A partial primal-dual gradient method is applied to reduce the number of variables and derive the control mechanism of the reformulated problem. Define $\alpha = [\gamma, \delta, \sigma]$. Then reduce the variable ω by:

$$\bar{L}(p, h, P, \varphi, \lambda, \mu, \zeta, \alpha) = \min_{\omega} L(\omega, p, h, P, \varphi, \lambda, \mu, \zeta, \alpha). \tag{5-9}$$

Furthermore, eliminate variable λ_{Ld} by defining:

$$\hat{L}(p,h,P,\varphi,\lambda_G,\mu,\zeta,\alpha)=\min_{\lambda_{Ld}}\bar{L}(p,h,P,\varphi,\lambda,\mu,\zeta,\alpha), \qquad (5\text{-}10)$$

where $\lambda=\left[\lambda_G,\lambda_{Ld}\right]$, in which λ_G and λ_{Ld} indicate the Lagrange multiplier for generator buses and load buses, respectively.

Notice that (5-11) needs the measurement of the aggregated power injection P_i^{in}:

$$\dot{\mu}_i=\varepsilon_{\mu_i}[P_i^{in}-p_i-\sum_{j:ij\in\varepsilon_{in}}B_{ij}(\varphi_i-\varphi_j)+\sum_{k:ki\in\varepsilon_{in}}B_{ki}(\varphi_k-\varphi_i)]. \qquad (5\text{-}11)$$

To eliminate the measurement of P_i^{in}, an intermediate variable r_i is introduced in the solution method where

$$r_i=\frac{K_i^C}{\varepsilon_{\mu_i}}\mu_i-\frac{K_i^C}{\varepsilon_{\lambda_i}}\lambda_i \quad . \qquad (5\text{-}12)$$

where K_i^C is a positive coefficient.

Other variables in the partial primal-dual gradient method are:

$$\dot{p}_i=-\varepsilon_{p_i}(C'_{i,e}(p_i)-\frac{\varepsilon_{\lambda_i}}{\varepsilon_{\lambda_i}+\varepsilon_{\mu_i}}\omega_i-\frac{\varepsilon_{\mu_i}}{K_i}r_i+\gamma_i^+-\gamma_i^--\sum_{m\in K^+}\zeta_i^m\frac{B_{m,i}}{K_{m,i}}+\sum_{n\in K^-}\zeta_i^n\frac{B_{n,i}}{K_{n,i}}) \quad i\in E_G, \qquad (5\text{-}13a)$$

$$\dot{h}_i=-\varepsilon_{h_i}\left[C'_{i,h}(h_i)-\delta_i^++\delta_i^-+\sum_{m\in K^+}\zeta_i^m-\sum_{n\in K^-}\zeta_i^n\right] \quad i\in E_G, \qquad (5\text{-}13b)$$

$$\dot{P}_{ij}=\varepsilon_{P_{ij}}(\omega_i-\omega_j) \quad i,j\in E,\ ij\in L_s, \qquad (5\text{-}13c)$$

$$\dot{\varphi}_i=-\varepsilon_{\varphi_i}[\sum_{j:ij\in L_{s,in}}B_{ij}(\mu_i-\mu_j-\sigma_{ij}^++\sigma_{ij}^-)-\sum_{k:ki\in L_{s,in}}B_{ki}(\mu_k-\mu_i-\sigma_{ki}^++\sigma_{ki}^-)] \quad i,j,k\in E, \qquad (5\text{-}13d)$$

$$\dot{r}_i=K_i[D_i\omega_i+\sum_{j:ij\in L_s}P_{ij}-\sum_{k:ki\in L_s}P_{ki}-\sum_{j:ij\in L_{s,in}}\tilde{B}_{ij}(\varphi_i-\varphi_j)+\sum_{k:ki\in L_{s,in}}\tilde{B}_{ki}(\varphi_k-\varphi_i)] \quad i,j,k\in E, \qquad (5\text{-}13e)$$

$$\dot{\zeta}_i^n=\varepsilon_{\zeta_i^n}\left[h_i-\frac{B_{n,i}}{K_{n,i}}p_i-\frac{\nu_{n,i}}{K_{n,i}}\right]_{\zeta_i^n}^+ \quad i\in E, \qquad (5\text{-}13f)$$

$$\zeta_i^m=\varepsilon_{\zeta_i^m}\left[h_i-\frac{B_{m,i}}{K_{m,i}}p_i-\frac{\nu_{m,i}}{K_{m,i}}\right]_{\zeta_i^m}^+ \quad i\in E, \qquad (5\text{-}13g)$$

$$\dot{\gamma}_i^+=\varepsilon_{\gamma_i^+}\left[p_i-\overline{p}_i\right]_{\gamma_i^+}^+ \quad i\in E, \qquad (5\text{-}13h)$$

$$\dot{\gamma}_i^-=\varepsilon_{\gamma_i^-}\left[p_i-\underline{p}_i\right]_{\gamma_i^-}^+ \quad i\in E, \qquad (5\text{-}13i)$$

$$\dot{\delta}_i^{+} = \varepsilon_{\delta_i^{+}} [Q_i^{in} - h_i - \bar{Q}_i^{v}]_{\delta_i^{+}}^{+} \quad i \in E\,, \tag{5-13j}$$

$$\dot{\delta}_i^{-} = \varepsilon_{\delta_i^{-}} [-Q_i^{in} + h_i + \underline{Q}_i^{v}]_{\delta_i^{-}}^{+} \quad i \in E\,, \tag{5-13k}$$

$$\dot{\sigma}_{ij}^{+} = \varepsilon_{\sigma_{ij}^{+}} [\tilde{B}_{ij}(\varphi_i - \varphi_j) - \underline{P}_{ij}]_{\sigma_{ij}^{+}}^{+} \quad i, j \in E,\ ij \in L_s\,, \tag{5-13l}$$

$$\dot{\sigma}_{ij}^{-} = \varepsilon_{\sigma_{ij}^{-}} [-\tilde{B}_{ij}(\varphi_i - \varphi_j) + \bar{P}_{ij}]_{\sigma_{ij}^{-}}^{+} \quad i, j \in E,\ ij \in L_s\,, \tag{5-13m}$$

where notations related to ε are positive step sizes. The operator $[w]_v^+$ indicates if $w > 0$ or $v > 0$, $[w]_v^+ = w$, otherwise $[w]_v^+ = 0$, so as proved in [55] $[w]_v^+ \le w$. Scalar μ_i in (5-13d) is calculated from r_i and ω_i.

Theorem 5-2 **(Global asymptotic convergence):** Under Assumptions 5-1 and 5-2, the algorithm (5-13) with the network model (5-3) and (5-4) converge to the optimal point $(\omega^*, p^*, h^*, P^*, \varphi^*, \lambda^*, \mu^*, \varepsilon^*, \gamma^*, \zeta^*, \alpha^*)$ asymptotically where $(\omega^*, p^*, h^*, P^*, \varphi^*)$ is the optimal solution of problem (5-7).

5.4.3 Algorithm Implementation

As shown in Figure 5-4, the (5-13) can be implemented in a fully-distributed manner, i.e., only by local measurement and neighborhood communication can the algorithm converge to the global optimal.

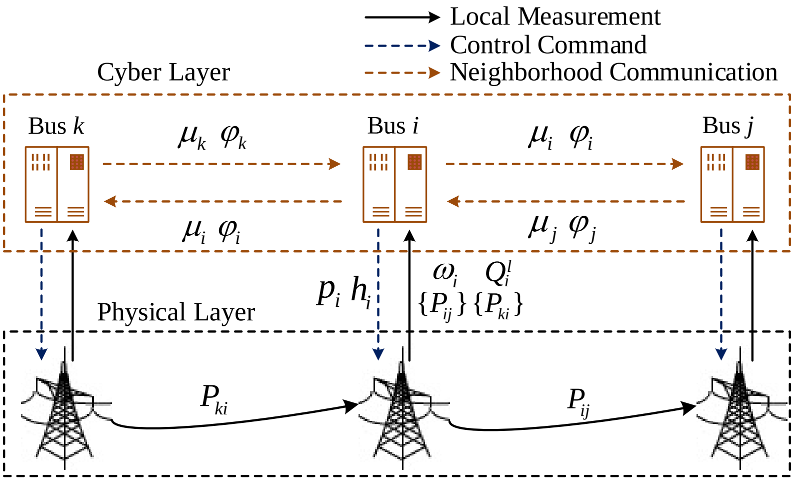

Figure 5-4. The implementation of the distributed control algorithm (5-13)

The implementation includes two steps: information gathering and control demand executing:

1) In the physical layer, each bus measures its local frequency deviation and line power flow deviation and updates the local heat load power deviation which is influenced

by heat demand, outer temperature, etc.

2) In the cyber layer, each bus exchanges Lagrange multiplier $\mu_i(t)$ and $\varphi_i(t)$ with adjacent buses. Then, each bus computes its control variables $p_i(t+1)$ and $h_i(t+1)$ and sends them to the physical layer to adjust power outputs.

By implementing the above two steps, the system frequency response and control command generation formulate a closed-loop to restore frequency with optimality guaranteed.

Theorem 5-3 **(Convergence with inaccurate coefficients):** If Assumption 5-2 works with following assumptions held:

1) $C_{i,e}(p_i)$ and $C_{i,h}(h_i)$ are α strongly convex and second-order continuously differentiable, and $C'_{i,e}(p_i)$ and $C'_{i,h}(h_i)$ are Lipschitz continuous for a Lipschitz constant $Lz > 0$.
2) The coefficient ε_{d_i} of (5-13a) and ε_{h_i} of (5-13b) satisfies:

$$C'_{i,e}(p_i) - \frac{\varepsilon_{\lambda_i}}{\varepsilon_{\lambda_i} + \varepsilon_{\mu_i}}\omega_i - \frac{\varepsilon_{\mu_i}}{K_i^C} r_i + \gamma_i^+ - \gamma_i^- - \sum_{m \in K^+} \zeta_i^m k_m + \sum_{n \in K^-} \zeta_i^n k_n = 0,$$

$$C'_{i,h}(h_i) - \delta_i^+ + \delta_i^- + \sum_{m \in K^+} \zeta_i^m - \sum_{n \in K^-} \zeta_i^n = 0.$$

3) Define the inaccurate damping coefficient $\tilde{D}_i = D_i + \tau a_i$, where the inaccurate coefficient τa_i satisfies:

$$\tau a_i \in 2(\underline{p}' - \sqrt{\underline{p}'^2 + \underline{p}' D_{\min}}, \underline{p}' + \sqrt{\underline{p}'^2 + \underline{p}' D_{\min}}),$$

where $\underline{p}' = 1/Lz$ and $D_{\min} = \min_{i \in E} D_i$.

The closed-loop system (5-3), (5-4), and (5-13) converges to a point $(\omega^*, p^*, h^*, P^*, \varphi^*, \lambda^*, \mu^*, \varepsilon^*, \gamma^*, \zeta^*, \alpha^*)$ where the $(\omega^*, p^*, h^*, P^*, \varphi^*)$ is the optimal solution of problem (5-7), even under inaccurate information of coefficients.

5.4 Proof of Optimality and Convergence

5.4.1 Proof of Theorem 5-1

Theorem 5-1**:** Let $(\omega^*, p^*, h^*, P^*, \varphi^*)$ become an optimum of the problem (5-7). When $\omega_i^* = 0$ is satisfied for $\forall i \in E$, the p^* and h^* are optimal for the problem (5-6).

Let $(\omega^*, p^*, h^*, P^*, \varphi^*)$ be an optimum of the problem (5-7). Assume $\forall i \in E$,

$\omega_i^* \neq 0$. Thus, the optimal cost function of problem (5-7) is:

$$f^* = \sum_{i\in E}[C_{i,e}(p_i^*) + C_{i,h}(h_i^*)] + \sum_{i\in E}\frac{1}{2}k_i^D D_i(\omega_i^*)^2 .$$

Then another solution $(\tilde{\omega}, p^*, h^*, P^*, \varphi^*)$ is constructed with $\tilde{\omega} = 0$ for $\forall i \in E$, $\tilde{P}_{ij} = \tilde{B}_{ij}(\varphi_i^* - \varphi_i^*)$ for $i, j \in E$, $ij \in L_{s,in}$, and $\tilde{P}_{ij} = 0$ for $i, j \in E$, $ij \in L_s \setminus L_{s,in}$. It is obvious that this solution is feasible for the problem (5-7), and the corresponding cost value is:

$$\tilde{f} = \sum_{i\in E}[C_{i,e}(p_i^*) + C_{i,h}(h_i^*)] < f^* ,$$

which contradicts the assumption that $(\omega^*, p^*, h^*, P^*, \varphi^*)$ is the optimum of the problem (5-7). Therefore, $\omega_i^* = 0$ for $\forall i \in E$.

Moreover, it is noticed that the (5-6b) and (5-7c) hold the same form. When $\omega_i = 0$ and given (p, h, φ), one can always find *P* which satisfies (5-7b) by using $\tilde{P}_{ij} = \tilde{B}_{ij}(\varphi_i^* - \varphi_i^*)$ for $i, j \in E$, $ij \in L_{s,in}$, and $\tilde{P}_{ij} = 0$ for $i, j \in E$, $ij \in L_s \setminus L_{s,in}$. As a result, the feasible set of (5-7) projected to (p, h, φ)-space under $\omega_i = 0$ is the same as the feasible set of (5-6) on the (p, h, θ)-space [56]. Thus, for any $(\tilde{\omega}, p^*, h^*, P^*, \varphi^*)$ which is an optimum of the problem (5-7), the (p^*, h^*) is the optimum of the problem (5-6).

5.4.2 Proof of Theorem 5-2

Define $x = (\varphi, P)$, $y = (\zeta, \gamma, \delta, \sigma)$, and $z = (p, h, x, \mu, \lambda_G, y)$ where $\mu = [\mu_G, \mu_{Ld}]$. The control mechanism can be written as:

$$\dot{p} = -\Gamma_p \frac{\partial \hat{L}}{\partial p},\ \ \dot{h} = -\Gamma_h \frac{\partial \hat{L}}{\partial h},\ \ \dot{x} = -\Gamma_x \frac{\partial \hat{L}}{\partial x},\ \ \dot{y} = -\Gamma_y \left[\frac{\partial \hat{L}}{\partial y}\right]_y^+ , \tag{5-14}$$

where $\Gamma_p = diag(\varepsilon_p)$ denotes the diagonal matrix of the positive coefficient of step sizes, etc. Define $o = (p, h, x)$ and $z^* = (o^*, y^*)$ to be any equilibrium of (5-13). Give:

$$U_{z^*}(z) = \frac{1}{2}(z - z^*)^T \Gamma_z^{-1}(z - z^*) , \tag{5-15}$$

where Γ_z is a block diagonal matrix consisting of corresponding entries (Γ_o, Γ_y).

According to Assumption 5-1, *L* is strictly convex in *p* and *h*. In addition, it can be proved that *L* is strictly concave in λ_G and linear in other variables. As a result, $L(o^*, y) - L(o^*, y^*) \leq 0$, and $L(o^*, y^*) - L(o, y^*) \leq 0$. Thus:

$$\dot{U}_{z*}(z) = -(o-o*)^T \frac{\partial L}{\partial o} + (y-y*)^T \left[\frac{\partial L}{\partial y}\right]_y^+ \leq -(o-o*)^T \frac{\partial L}{\partial o} + (y-y*)^T \frac{\partial L}{\partial y}$$

$$\leq [L(o*,y) - L(o*,y*)] + [L(o*,y*) - L(o,y*)] \leq 0,$$

which indicates that $U_{z*}(z)$ is bounded when $t \geq 0$ According to the Lasalle's invariance principle, the trajectory $z(t)$ asymptotically converges to the optimal point z_0, which is the optimal solution of (5-13) where variables are optimal for (5-3) and (5-4).

5.4.3 Proof of Theorem 5-3

To prove the distributed solution method is robust to inaccurate damping coefficient *D_i*, the following changes are made:

1) $p_i = \left(C'_{i,e}\right)^{-1}(\lambda_i + \mu_i)$, and $h_i = \left(C'_{i,h}\right)^{-1}(\delta^+ + \delta^-)$

2) $\gamma^+ \equiv \gamma^- \equiv \zeta \equiv 0.$

The equation (5-3), (5-4), and (5-13) still holds except (5-11):

$$\dot{\mu}_i = \varepsilon_{\mu_i}\left[P_i^{in} - p_i + \tau\alpha_i\omega_i - \sum_{j:ij\in L_{s,in}} \tilde{B}_{ij}(\varphi_i - \varphi_j) + \sum_{k:ki\in L_{s,in}} \tilde{B}_{ki}(\varphi_k - \varphi_i)\right].$$

It can be proved that the time derivative of (5-15) is bounded:

$$\dot{U}(w) \leq \int_0^1 (w-w^*)^T H(w(s))(w-w^*),$$

where $w(s) = w^* + s(w-w^*)$. The matrix *H* is the differential of $\hat{L}$ in which

$$H = \begin{array}{c|ccccc|c} & (\varphi,Q^v) & (P,\mu_{Ld}) & (\mu_G,\lambda_G) & \delta & (\varepsilon,\alpha) & \\ \hline & 0 & 0 & 0 & 0 & 0 & (\varphi,Q^v) \\ & 0 & H_{P,\mu_{LD}} & 0 & 0 & 0 & (P,\mu_{Ld}) \\ & 0 & 0 & H_{\mu_G,\lambda_G} & 0 & 0 & (\mu_G,\lambda_G) \\ & 0 & 0 & 0 & -h' & 0 & \delta \\ & 0 & 0 & 0 & 0 & 0 & (\varepsilon,\alpha) \end{array},$$

where $H_{P,\mu_{LD}}$ and H_{μ_G,λ_G} are both negative semi-definite sub-matrices.

Next, with the assumptions in Theorem 5-3, since $H \preceq 0$, it can be proved that according to the invariance principle the problem (5-13) is robust for the inaccurate coefficient $\tilde{D}_i$, when H is negative semi-definite [55].

5.5 Case Studies

Case studies are designed to demonstrate 1) the necessity of considering electric-heat coupling constraints in frequency control and 2) the robustness of the distributed algorithm under inaccurate coefficients.

The topology of the combined heat and power system is shown in Figure 5-5 [54].

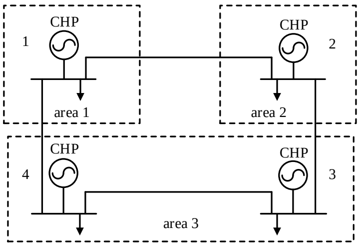

Figure 5-5. The topology of combined heat and power

5.5.1 Case 1: Necessity of Considering Electric-Heat Coupling Constraints

This case is designed to present the importance of considering electric-heat coupling in frequency control. The power step change happens at $t = 0$, where $P_3^{in} = 0.3$p.u., $Q_3^{in} = 0.3$p.u., and the heat inertia $Q_3^{v} = 0.1$p.u. The left boundary of the CHP unit at bus 3 is $h_3 \le 0.5 p_3$. The results are shown in Figures 5-6 and 5-7, where electric-heat coupling constraints are NOT considered in scenario *e1* , and in scenario *e2*, electric-heat coupling constraints are considered.

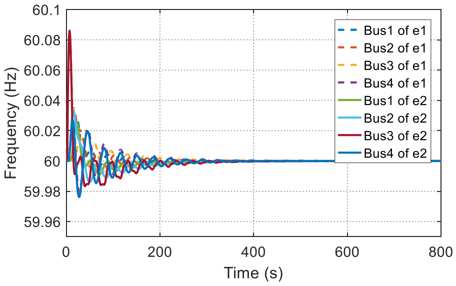

Figure 5-6. Frequency response to step electric and heat power changes

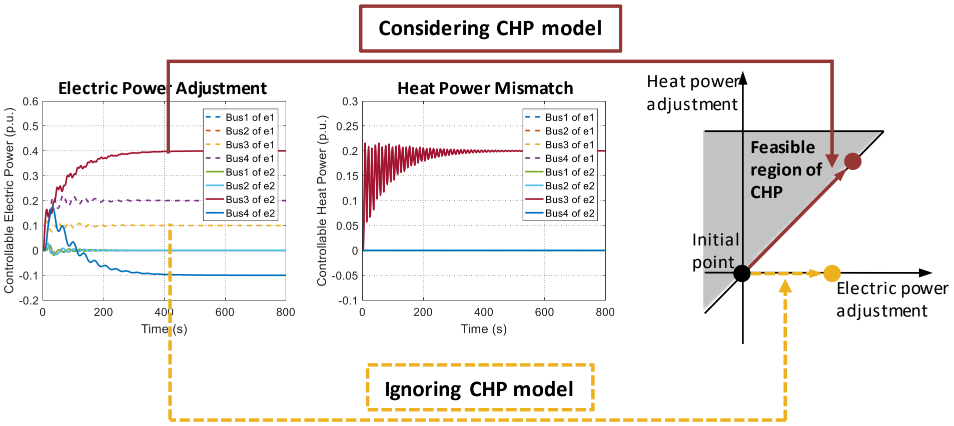

Figure 5-7. Power adjustment under step electric and heat power changes

According to results in Figure 5-6, the frequency is restored in both scenarios *e1* and *e2*, however, the electric and heat power outputs are different under two scenarios. Apparently, as shown in Figure 5-7, in scenario *e1* power outputs exceed the feasible region of CHP unit at bus 3, in which the electric-heat coupling constraints (5-6d) and (5-6e) have been broken. If this circumstance happens, the control commands cannot be executed, which dangers the frequency stability. But in scenario *e2*, the proposed method successfully satisfies the electric-heat coupling constraints (5-6d) and (5-6e) with the restoration of frequency.

5.5.2 Case 2: Robustness under Inaccurate Coefficient

In this case, the robustness of the proposed method is studied under the step change $P_3^{in} = 0.3$ p.u. at $t = 0$. To verify the robustness, the tested coefficient $\tilde{D}_i$ is set at *k* times of the real damping coefficient D_i, i.e., $\tilde{D}_i = kD_i$.

As shown in Figure 5-8, when *k* is approaching 0, the frequency damping is increasing and the convergence speed is decreasing. But if *k* is too large, the system becomes unstable and even fails to converge. Under given conditions, the proposed method is robust when $\tilde{D}_i$ varies from 0.1 to 10 times of real value D_i.

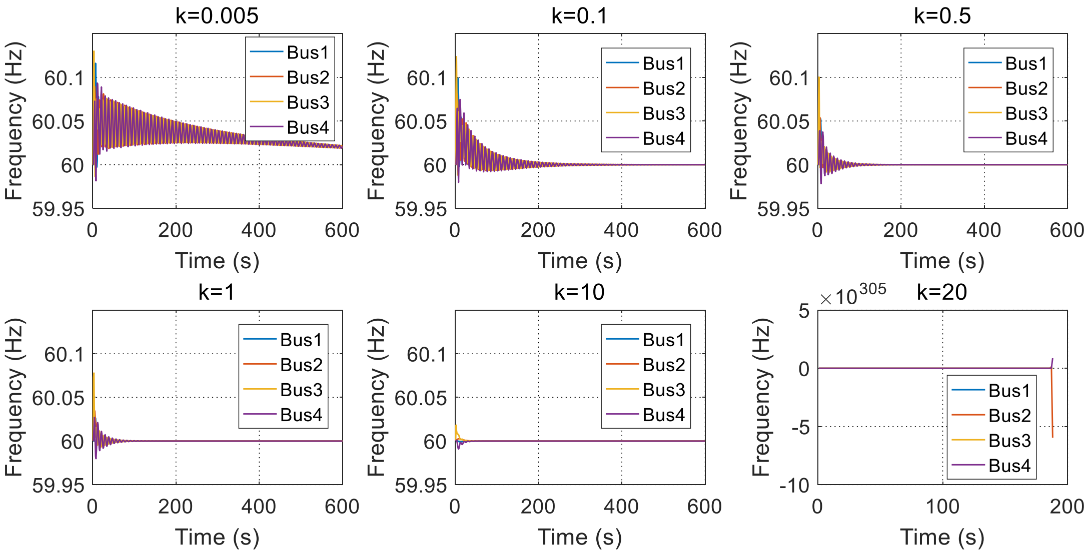

Figure 5-8. Frequency response under inaccurate coefficients.

5.6 Conclusion

In this chapter, a fully-distributed frequency control method is proposed with system-wide optimality for the combined heat and power systems considering electric-heat coupling constraints, electric line flow limits, and inaccurate damping coefficients. Based on reverse engineering, the proposed method only needs local measurement and neighborhood communication to reach system-wide optimality and is globally asymptotical stability. Case studies show that the proposed method can eliminate frequency deviations with economic optimality even when the damping coefficient is inaccurate. Also, it is of vital importance to consider the electric-heat coupling constraints to ensure the control commands are in the feasible region of generators.

The future work includes extending the proposed method to large scale cases and improving the dynamic performance of the algorithm by optimizing the step size.

Chapter 6: Conclusion

In this dissertation, combined heat and power systems’ challenges from multiple time scale characteristics and simplifications on system topology and control mechanisms are addressed in terms of power flow analysis and optimization. Also, solution methods with improvement in convergence and efficiency are proposed to deal with the nonlinearity for the power flow problem, the non-convexity for the optimization problem, and the distributed implementation for frequency control problem.

The main conclusions from case studies are summarized as follows.

1) In the combined electric and heat power flow analysis, the proposed method considers different dynamic time scales of electricity and heat, which improves the accuracy and convergence compared with the existing steady-state method. Compared with measurement data, the proposed method has high accuracy. When loops and variable mass flow are considered, the proposed method overcomes the commercial software’s failure of reflecting the heat dynamic process.
2) In the synchronous economic dispatch with variable mass flow, the proposed optimization model reduces the complexity from the integers in the existing model without compromise on accuracy. The proposed solution method with improved convergence and acceleration overcomes the divergence problem of the solver IPOPT. Compared with existing fixed mass flow methods, the proposed method has lower costs without any additional devices.
3) In the asynchronous economic dispatch, the proposed asynchronous dispatch model incorporates the different adjustment time scales of electricity and heat. Compared with traditional synchronous methods, the proposed method can maintain generation-demand balance and eliminate infeasible results, which contributes to the improvement in efficiency and security. With the heat dispatch interval increasing, the computational efficiency of the hybrid model is higher than the identical model.
4) In terms of the frequency control, the proposed fully-distributed control method restores the frequency with system-wide optimality. The consideration of electric-heat coupling in the proposed control method overcomes the risk of

violating generator’s feasible regions. Moreover, the proposed method is robust to the inaccurate damping coefficient.

As a continuation of this dissertation, several research topics could be extended. First, quantifying the dynamic time of a given combined heat and power system helps to decide the proper and efficient adjustment time scale. Second, how to improve the optimality of the proposed solution method for non-convex economic dispatch in Chapter 4 is an open question. Last but not least, we can improve the dynamic performance of frequency control by selecting proper step sizes.

References

[1] Wikipedia.2017 Taiwan blackout [EB/OL]. https://en.wikipedia.org/wiki/2017_Taiwan_blackout, 2020.02.

[2] 银川新闻网.宁夏电投西夏热电厂锅炉突发爆管故障 影响供热面积达 1300 万平方米 预计今日中午用户家中恢复正常温度 [EB/OL]. https://mp.weixin.qq.com/s/Pvfv23Am5hC1sCsgbjezFg,2018.12.

[3] Sun H, Guo Q, Pan Z. Energy Internet: concept, architecture and frontier outlook[J]. Automation of Electric Power Systems, 2015, 39(19): 1-8.

[4] Wu J Z, Yan J Y, Jia H J, et al. Integrated energy systems[J]. Applied Energy, 2016, 167: 155-157.

[5] Sun H, Guo Q, Zhang B, et al. Integrated energy management system: Concept, design, and demonstration in China[J]. IEEE Electrification Magazine, 2018, 6(2): 42-50.

[6] Beigvand S D, Abdi H, La Scala M. Combined heat and power economic dispatch problem using gravitational search algorithm[J]. Electric Power Systems Research, 2016, 133: 160-172.

[7] Riipinen M. District heating and cooling in Helsinki[C]. International Energy Agency CHP/DHC Collaborative and Clean Energy. Paper presented at the Ministerial CHP/DHC Working Group Joint Workshop. 2013.

[8] Kang C, Chen X, Xu Q, et al. Balance of power: toward a more environmentally friendly, efficient, and effective integration of energy systems in China[J]. IEEE Power and Energy Magazine, 2013, 11(5): 56-64.

[9] Sun H, Pan Z, Guo Q. Energy management for multi-energy flow: challenges and prospects[J]. Automation of Electric Power Systems, 2016, 40(15): 1-8.

[10] Qin X, Sun H, Shen X, et al. A generalized quasi-dynamic model for electric-heat coupling integrated energy system with distributed energy resources[J]. Applied energy, 2019, 251: 113270.

[11] Wang J, You S, Zong Y, et al. Investigation of real-time flexibility of combined heat and power plants in district heating applications[J]. Applied energy, 2019, 237: 196-209.

[12] Geidl M. Integrated modeling and optimization of multi-carrier energy systems[D]. ETH Zurich, 2007.

[13] Morvaj B, Evins R, Carmeliet J. Optimization framework for distributed energy systems with integrated electrical grid constraints[J]. Applied energy, 2016, 171: 296-313.

[14] Morvaj B, Evins R, Carmeliet J. Optimising urban energy systems: Simultaneous system sizing, operation and district heating network layout[J]. Energy, 2016, 116: 619-636.

[15] Liu X, Wu J, Jenkins N, et al. Combined analysis of electricity and heat networks[J]. Applied Energy, 2016, 162: 1238-1250.

[16] Abeysekera M. Combined analysis of coupled energy networks[D]. Cardiff University, 2016.

[17] Pan Z, Guo Q, Sun H. Interactions of district electricity and heating systems considering time-scale characteristics based on quasi-steady multi-energy flow[J]. Applied energy, 2016, 167: 230-243.

[18] Duquette J, Rowe A, Wild P. Thermal performance of a steady state physical pipe model for simulating district heating grids with variable flow[J]. Applied Energy, 2016, 178: 383-393.

[19] Sartor K, Dewalef P. Experimental validation of heat transport modelling in district heating networks[J]. Energy, 2017, 137: 961-968.

[20] Dahm J. District heating pipelines in the ground-simulation model[J]. 1999.

[21] Wang Y, You S, Zhang H, et al. Thermal transient prediction of district heating pipeline: Optimal selection of the time and spatial steps for fast and accurate calculation[J]. Applied Energy, 2017, 206: 900-910.

[22] Hassine I B, Eicker U. Impact of load structure variation and solar thermal energy integration on an existing district heating network[J]. Applied Thermal Engineering, 2013, 50(2): 1437-1446.

[23] Lin C, Wu W, Zhang B, et al. Decentralized solution for combined heat and power dispatch through benders decomposition[J]. IEEE Transactions on sustainable energy, 2017, 8(4): 1361-1372.

[24] Gu W, Wang J, Lu S, et al. Optimal operation for integrated energy system considering thermal inertia of district heating network and buildings[J]. Applied Energy, 2017, 199: 234-246.

[25] Wang D, Zhi Y, Jia H, et al. Optimal scheduling strategy of district integrated heat and power system with wind power and multiple energy stations considering thermal inertia of buildings under different heating regulation modes[J]. Applied energy, 2019, 240: 341-358.

[26] Pan Z, Wu J, Sun H, et al. Quasi-dynamic interactions and security control of integrated electricity and heating systems in normal operations[J]. CSEE Journal of Power and Energy Systems, 2019, 5(1): 120-129.

[27] Li Z, Wu W, Shahidehpour M, et al. Combined heat and power dispatch considering pipeline energy storage of district heating network[J]. IEEE Transactions on Sustainable Energy, 2015, 7(1): 12-22.

[28] Guelpa E, Verda V. Compact physical model for simulation of thermal networks[J]. Energy, 2019, 175: 998-1008.

[29] Wang L X, Zheng J H, Li M S, et al. Multi-time scale dynamic analysis of integrated energy systems: An individual-based model[J]. Applied energy, 2019, 237: 848-861.

[30] Wang H, Wang H, Zhou H, et al. Modeling and optimization for hydraulic performance design in multi-source district heating with fluctuating renewables[J]. Energy Conversion and Management, 2018, 156: 113-129.

[31] Lund H, Werner S, Wiltshire R, et al. 4th Generation District Heating (4GDH): Integrating smart thermal grids into future sustainable energy systems[J]. Energy, 2014, 68: 1-11.

[32] Huang J, Li Z, Wu Q H. Coordinated dispatch of electric power and district heating networks: A decentralized solution using optimality condition decomposition[J]. Applied energy, 2017, 206: 1508-1522.

[33] Geoffrion A M. Generalized Benders decomposition[J]. Journal of Optimization Theory and Applications, 1972, 10(4):237-260.

[34] Hao J, Chen Q, He K, et al. A heat current model for heat transfer/storage systems and its application in integrated analysis and optimization with power systems[J]. IEEE Transactions on Sustainable Energy, 2018, 11(1): 175-184.

[35] Pan Z, Guo Q, Sun H. Feasible region method based integrated heat and electricity dispatch considering building thermal inertia[J]. Applied energy, 2017, 192: 395-407.

[36] Li Z, Wu W, Wang J, et al. Transmission-constrained unit commitment considering combined electricity and district heating networks[J]. IEEE Transactions on Sustainable Energy, 2015, 7(2): 480-492.

[37] Vesterlund M, Toffolo A, Dahl J. Optimization of multi-source complex district heating network, a case study[J]. Energy, 2017, 126: 53-63.

[38] Huang S, Tang W, Wu Q, et al. Network constrained economic dispatch of integrated heat and electricity systems through mixed integer conic programming[J]. Energy, 2019, 179: 464-474.

[39] Chen Y, Guo Q, Sun H, et al. A water mass method and its application to integrated heat and electricity dispatch considering thermal inertias[J]. Energy, 2019, 181: 840-852.

[40] Bao Z, Zhou Q, Yang Z, et al. A multi time-scale and multi energy-type coordinated microgrid scheduling solution—Part I: Model and methodology[J]. IEEE Transactions on Power Systems, 2014, 30(5): 2257-2266.

[41] Yao S, Gu W, Zhou S, et al. Hybrid timescale dispatch hierarchy for combined heat and power system considering the thermal inertia of heat sector[J]. IEEE Access, 2018, 6: 63033-63044.

[42] Zhang B, Wu W, Zheng T, et al. Design of a multi-time scale coordinated active power dispatching system for accommodating large scale wind power penetration[J]. Dianli Xitong Zidonghua (Automation of Electric Power Systems), 2011, 35(1): 1-6.

[43] Liu N, Wang J, Wang L. Hybrid energy sharing for multiple microgrids in an integrated heat–electricity energy system[J]. IEEE Transactions on Sustainable Energy, 2018, 10(3): 1139-1151.

[44] Gu W, Lu S, Yao S, et al. Hybrid time-scale operation optimization of integrated energy system. Electric Power Automation Equipment[J], 2019, 39(8).

[45] Ilic M D. From hierarchical to open access electric power systems[J]. Proceedings of the IEEE, 2007, 95(5): 1060-1084.

[46] Bejestani A K, Annaswamy A, Samad T. A hierarchical transactive control architecture for renewables integration in smart grids: Analytical modeling and stability[J]. IEEE Transactions on Smart Grid, 2014, 5(4): 2054-2065.

[47] Goldman C, Heffner M G, Kirby B. Loads Providing Ancillary Services: Review of International Experience--Technical Appendix: Market Descriptions[J]. 2007.

[48] Fabozzi D, Thornhill N F, Pal B C. Frequency restoration reserve control scheme with participation of industrial loads[C]. 2013 IEEE Grenoble Conference. IEEE, 2013: 1-6.

[49] Liu H, Hu Z, Song Y, et al. Vehicle-to-grid control for supplementary frequency regulation considering charging demands[J]. IEEE Transactions on Power Systems, 2014, 30(6): 3110-3119.

[50] Lee S J, Kim J H, Kim C H, et al. Coordinated control algorithm for distributed battery energy storage systems for mitigating voltage and frequency deviations[J]. IEEE Transactions on Smart Grid, 2015, 7(3): 1713-1722.

[51] Andreasson M, Dimarogonas D V, Sandberg H, et al. Distributed control of networked dynamical systems: Static feedback, integral action and consensus[J]. IEEE Transactions on Automatic Control, 2014, 59(7): 1750-1764.

[52] Xu Y, Guo Q, Sun H, et al. Distributed discrete robust secondary cooperative control for islanded microgrids[J]. IEEE transactions on Smart Grid, 2018, 10(4): 3620-3629.

[53] Xu Y, Sun H, Gu W, et al. Optimal distributed control for secondary frequency and voltage regulation in an islanded microgrid[J]. IEEE Transactions on Industrial Informatics, 2018, 15(1): 225-235.

[54] Li N, Zhao C, Chen L. Connecting automatic generation control and economic dispatch from an optimization view[J]. IEEE Transactions on Control of Network Systems, 2015, 3(3): 254-264.

[55] Mallada E, Zhao C, Low S. Optimal load-side control for frequency regulation in smart grids[J]. IEEE Transactions on Automatic Control, 2017, 62(12): 6294-6309.

[56] Chen X, Zhao C, Li N. Distributed automatic load-frequency control with optimality in power systems[C]. 2018 IEEE Conference on Control Technology and Applications (CCTA). IEEE, 2018: 24-31.

[57] Kondoh J. Experiment of an electric water heater with autonomous frequency regulation[J]. IEEJ transactions on electrical and electronic engineering, 2013, 8(3): 223-228.

[58] Beil I, Hiskens I, Backhaus S. Frequency regulation from commercial building HVAC demand response[J]. Proceedings of the IEEE, 2016, 104(4): 745-757.

[59] Sun T, Lu J, Li Z, et al. Modeling combined heat and power systems for microgrid applications[J]. IEEE Transactions on Smart Grid, 2017, 9(5): 4172-4180.

[60] Sun H, Guo Q, Pan Z. Energy Internet: concept, architecture and frontier outlook[J]. Automation of Electric Power Systems, 2015, 39(19): 1-8.

[61] Laajalehto T, Kuosa M, Mäkilä T, et al. Energy efficiency improvements utilising mass flow control and a ring topology in a district heating network[J]. Applied thermal engineering, 2014, 69(1-2): 86-95.

[62] Larock B E, Jeppson R W, Watters G Z. Hydraulics of pipeline systems[M]. CRC press, 1999.

[63] Liu X. Combined analysis of electricity and heat networks[D]. Cardiff University, 2013.

[64] Incropera F P, Lavine A S, Bergman T L, et al. Fundamentals of heat and mass transfer[M]. Wiley, 2007.

[65] Bøhm B, Ha S, Kim W, et al. Simple models for operational optimisation[J]. Contract, 2002, 524110: 0010.

[66] Zhao H. Analysis, Modelling and operational optimazation of district heating systems[M]. Centre for District Heating Technology, 1995.

[67] Lahdelma R, Hakonen H. An efficient linear programming algorithm for combined heat and power production[J]. European Journal of Operational Research, 2003, 148(1): 141-151.

[68] Glover J D, Sarma M S, Overbye T. Power system analysis & design, SI version[M]. Cengage Learning, 2012.

[69] Hongbin S, Boming Z, Niande X. Study on convergence of back/forward sweep distribution power flow [J]. proceedings of the csee, 1999.

[70] Tan K K, Xu H K. Approximating fixed points of non-expansive mappings by the Ishikawa iteration process[J]. Journal of Mathematical Analysis and Applications, 1993, 178: 301-301.

[71] Vivian J, de Uribarri P M Á, Eicker U, et al. The effect of discretization on the accuracy of two district heating network models based on finite-difference methods[J]. Energy Procedia, 2018, 149: 625-634.

[72] Xing Y, Bagdanavicius A, Lannon S C, et al. Low temperature district heating network planning with the focus on distribution energy losses[J]. 2012.

[73] Duran M A, Grossmann I E. An outer-approximation algorithm for a class of mixed-integer nonlinear programs[J]. Mathematical programming, 1986, 36(3): 307-339.

[74] Grossmann I E, Kravanja Z. Mixed-integer nonlinear programming techniques for process systems engineering[J]. Computers & Chemical Engineering, 1995, 19: 189-204.

[75] Guo Y, Tong L, Wu W, et al. Coordinated multi-area economic dispatch via critical region projection[J]. IEEE Transactions on Power Systems, 2017, 32(5): 3736-3746.

[76] Quesada I, Grossmann I E. An LP/NLP based branch and bound algorithm for convex MINLP optimization problems[J]. Computers & chemical engineering, 1992, 16(10-11): 937-947.

[77] Haftka R T, Gürdal Z. Elements of structural optimization[M]. Springer Science & Business Media, 2012: 176-182.

[78] Yao S, Gu W, Lu S, et al. Dynamic Optimal Energy Flow in the Heat and Electricity Integrated Energy System[J]. IEEE Transactions on Sustainable Energy, 2020.

[79] Qin X, Zhang X, Shen X, et al. Distributed Optimal Frequency Control for Integrated Energy Systems with Electricity and Heat[C]. 2019 IEEE PES General Meeting, IEEE, 2019.

Acknowledgement

I have had the privilege of being advised by Professor Hongbin Sun. He not only helps me with the research topics and ideas but also teaches me principles of study and life. He encourages me to become an individual researcher and inspires me to do “valuable” research: Go depth in theory and link academic research with industrial application. With his support and influence, I have decided to pursue a Ph.D. degree.

I also feel honored to be instructed by Research Scientist Doctor Xinwei Shen and Professor Ye Guo. Doctor Xinwei Shen has instructed me for my 3-year master study with precious help, support, and encouragement. Every time he is very kind to discuss the research and career plan with me, which helps me overcome my difficulties. Professor Ye Guo is really nice and helpful to instruct me with patience, and when I came to him could I receive the specific direction and effective suggestions. His taste and attitude on research and life motivate me to become a rigorous researcher.

Moreover, I want to give my great thanks to Professor Shmuel S. Oren for his enlightening words in class, encouraging instructions at our discussion, and important recommendations during my application. I am really grateful to Professor Xuan Zhang and Doctor Zhaoguang Pan. I will never forget Professor Xuan Zhang’s instruction on my research and efforts in correcting my paper word for word, and Doctor Zhaoguang Pan’s valuable help for my research and life. Also, I feel so lucky to receive a rigorous academic attitude and career support from Professor Wenchuan Wu and Professor Qinglai Guo.

I am so fortunate to be a member of the EMS big family, Tsinghua-Berkeley Shenzhen Institute, and Tsinghua University.

Most of all, I want to say thank you to my parents for their unconditional support and love.

This work is supported by the National Key R&D Programs of China 2018YFB0905000.

声　明

本人郑重声明：所呈交的学位论文，是本人在导师指导下，独立进行研究工作所取得的成果。尽我所知，除文中已经注明引用的内容外，本学位论文的研究成果不包含任何他人享有著作权的内容。对本论文所涉及的研究工作做出贡献的其他个人和集体，均已在文中以明确方式标明。

Personal Statement

I solemnly declare that this dissertation was prepared solely by myself under instruction of my advisors. To my knowledge, except for documents cited in the dissertation, the research results do not contain any achievements of any others who have claimed copyrights. To contributions made by relevant individuals and organizations in the completion of the dissertation, I have clearly acknowledged all their efforts.

Signature by Author: ______________________

Date:________________________